GCPS

NUMERICAL MODELING OF HYDROGEN EMBRITTLEMENT ON SINGLE CRYSTALS

A THESIS SUBMITTED TO
THE GRADUATE SCHOOL OF NATURAL AND APPLIED SCIENCES
OF
ATILIM UNIVERSITY

BY

CANER ÇAMALAN

IN PARTIAL FULFILLMENT OF THE REQUIREMENTS
FOR
THE DEGREE OF DOCTOR OF PHILOSOPHY
IN
THE DEPARTMENT OF MECHANICAL ENGINEERING

JUNE 2025

Approval of the Graduate School of Natural and Applied Sciences, Atılım University.

_____

Assoc. Prof. Dr. Gökhan TUNÇ
Director

I certify that this thesis satisfies all the requirements as a thesis for the degree of **Doctor of Philosophy in Mechanical Engineering Department, Atılım University**.

_____

Prof. Dr. Hasan Umur AKAY
Acting Head of Department

This is to certify that we have read the thesis NUMERICAL MODELING OF HYDROGEN EMBRITTLEMENT ON SINGLE CRYSTALS submitted by CANER ÇAMALAN and that in our opinion it is fully adequate, in scope and quality, as a thesis for the degree of Doctor of Philosophy.

_____

Prof. Dr. Özgür ASLAN
Supervisor

Examining Committee Members:

Prof. Dr. Ahmet Hakan ARGEŞO
Aerospace Engineering, Atılım University _____

Prof. Dr. Özgür ASLAN
Mechanical Engineering, University of Bristol _____

Asst. Prof. Dr. Ferit SAİT
Mechanical Engineering, Çankaya University _____

Asst. Prof. Dr. Hakan KALKAN
Mechanical Engineering, Atılım University _____

Asst. Prof. Dr. Bahram LOTFI
Mechanical Engineering, TOBB ETU _____

Date: June 27, 2025

I declare and guarantee that all data, knowledge and information in this document has been obtained, processed and presented in accordance with academic rules and ethical conduct. Based on these rules and conduct, I have fully cited and referenced all material and results that are not original to this work.

Name, Last Name : CANER ÇAMALAN

Signature :

ABSTRACT

NUMERICAL MODELING OF HYDROGEN EMBRITTLEMENT ON SINGLE CRYSTALS

Çamalan, Caner

PhD, Department of Mechanical Engineering

Supervisor : Prof. Dr. Özgür ASLAN

June 2025, 138 pages

Hydrogen embrittlement (HE) is a critical degradation mechanism that compromises the structural integrity of metallic components exposed to hydrogen-rich environments. This phenomenon is particularly detrimental in high-performance engineering alloys, where microscopic interactions between hydrogen atoms and crystalline defects can trigger premature failure. In this thesis, we present a comprehensive computational framework for modeling hydrogen embrittlement in single-crystal metallic systems by integrating large-deformation crystal plasticity with variational phase-field fracture theory.

The initial chapters provide the theoretical background on finite-strain kinematics and the thermomechanical formulation of crystal plasticity, including the multiplicative decomposition of the deformation gradient and the evolution of slip on crystallographic systems. A phenomenological description of hydrogen transport, trapping, and its role in embrittlement is established.

Building upon this foundation, we develop a thermodynamically consistent coupled model that incorporates anisotropic plastic deformation and hydrogen-induced fracture within a phase-field variational framework. The governing equations are derived from a total free energy functional accounting for elastic, plastic, and fracture contri-

butions, with degradation functions applied selectively to the elastic and yield stresses to capture the ductile nature of hydrogen-assisted damage. The fracture evolution is driven by an accumulation variable that accounts for both mechanical work and plastic deformation, enabling the model to simulate anisotropic crack initiation, propagation, and bifurcation.

Extensive numerical simulations are performed on single-crystal geometries under tensile and shear loading, highlighting the effects of hydrogen concentration, crystallographic orientation, and length scale parameters on crack evolution. Mesh refinement and threshold sensitivity studies are conducted to verify the robustness of the model. The results reveal critical insights into crack deflection, anisotropic damage accumulation, and the interaction between slip activity and fracture in hydrogen-affected crystals.

Overall, the proposed framework offers a predictive tool for analyzing hydrogen embrittlement in anisotropic materials, bridging the gap between microstructural mechanisms and macroscopic fracture behavior. The methodology sets a foundation for future studies on polycrystalline aggregates, grain boundary effects, and multiscale coupling in hydrogen-sensitive alloys.

Keywords: Hydrogen Embrittlement, Phase Field Modeling, Ductile Fracture, Crystal Plasticity, Large Deformation

ÖZ

TEK KRİSTALLERDE HİDROJEN GEVREKLEŞMESİNİN SAYISAL MODELLENMESİ

Çamalan, Caner

Doktora, Makine Mühendisliği

Tez Yöneticisi : Prof. Dr. Özgür ASLAN

Haziran 2025, 138 sayfa

Hidrojen gevrekleşmesi (HG), hidrojen açısından zengin ortamlara maruz kalan metalik bileşenlerin yapısal bütünlüğünü tehlikeye atan kritik bir bozunma mekanizmasıdır. Bu olgu, özellikle yüksek performanslı mühendislik alaşımlarında, hidrojen atomları ile kristal kusurlar arasındaki mikroskobik etkileşimlerin erken kırılmaları tetikleyebilmesi nedeniyle son derece zararlıdır. Bu tezde, büyük deformasyonlu kristal plastisitesini varyasyonel faz-alan kırılma teorisi ile entegre ederek tek kristalli metalik sistemlerde hidrojen gevrekleşmesini modellemek için kapsamlı bir hesaplama çerçevesi sunuyoruz.

İlk bölümler, deformasyon gradyanının çarpımsal ayrışması ve kristalografik sistemlerde kaymanın evrimi dahil olmak üzere sonlu-gerinim kinematiği ve kristal plastisitesinin termomekanik formülasyonu hakkında teorik arka plan sağlar. Hidrojen taşınımı, tuzaklanması ve gevrekleşmedeki rolüne ilişkin fenomenolojik bir açıklama getirilmiştir.

Bu temele dayanarak, anizotropik plastik deformasyonu ve hidrojen kaynaklı kırılmayı bir faz alanı varyasyonel çerçevesi içinde birleştiren termodinamik olarak tutarlı bir birleşik model geliştiriyoruz. Yönetici denklemler, hidrojen destekli hasarın sünek

doğasını yakalamak için elastik ve akma gerilmelerine seçici olarak uygulanan bozunma fonksiyonları ile elastik, plastik ve kırılma katkılarını hesaba katan toplam serbest enerji fonksiyonelinden türetilmiştir. Kırılma evrimi, hem mekanik işi hem de plastik deformasyonu hesaba katan bir birikim değişkeni tarafından yönlendirilir ve modelin çatlak başlangıcını, yayılmasını ve çatallanmasını yönelime duyarlı bir şekilde simüle etmesini sağlar.

Çekme ve kesme yüklemesi altında tek kristal geometriler üzerinde kapsamlı sayısal simülasyonlar gerçekleştirilerek hidrojen konsantrasyonu, kristalografik yönelim ve uzunluk ölçeği parametrelerinin çatlak gelişimi üzerindeki etkileri vurgulanmıştır. Modelin sağlamlığını doğrulamak için ağ inceltme ve eşik hassasiyeti çalışmaları yapılmıştır. Sonuçlar, çatlak sapması, anizotropik hasar birikimi ve hidrojenden etkilenen kristallerde kayma aktivitesi ile kırılma arasındaki etkileşim hakkında kritik bilgiler ortaya koymaktadır.

Genel olarak, önerilen çerçeve, anizotropik malzemelerde hidrojen gevrekleşmesini analiz etmek için mikroyapısal mekanizmalar ve makroskopik kırılma davranışı arasındaki boşluğu dolduran öngörücü bir araç sunmaktadır. Bu metodoloji, gelecekteki çalışmalar için bir temel oluşturmaktadır.

Anahtar Kelimeler: Hidrojen Gevrekleşmesi, Faz Alanı Modellemesi, Sünek Kırılma, Kristal Plastisite, Sonlu Deformasyon

ACKNOWLEDGMENTS

I would first and foremost like to express my deepest gratitude to Prof. Dr. Özgür Aslan, for his unwavering support, insightful guidance, and invaluable mentorship throughout the course of this research. His profound expertise combined with his thoughtful encouragement and patience, has been a constant source of inspiration for me. His dedication to scientific rigor and clarity has shaped my understanding of research, and I am truly grateful for the academic freedom and trust he granted me which allowed me to grow as an independent researcher.

I am truly honored by the presence and contributions of my thesis committee members. I extend my sincere thanks to Prof. Dr. Ahmet Hakan Argeşo, who graciously took on the role of head of the committee, for his thoughtful engagement and support during the evaluation process. I am also especially grateful to Asst. Prof. Dr. Ferit Sait for his continuous willingness to assist and his generous support throughout the course of this work and his presence of being a committee member. I am equally thankful to Asst. Prof. Dr. Hakan Kalkan and Asst. Prof. Dr. Bahram Lotfi for their time, careful review, and valuable feedback, all of which have contributed meaningfully to the quality and depth of this thesis.

I gratefully acknowledge the financial support provided by TÜBİTAK(The Scientific and Technological Research Council of Türkiye) under project number 119C037. I also thank TUSAŞ Engine Industries(TEI) for their partnership and valuable contributions within the scope of the same project. Their support played a crucial role in enabling the successful completion of this work.

I would like to express my sincere gratitude to Prof. Dr. Emin Bayraktar for the opportunity to collaborate with him on a joint publication and for his valuable contributions throughout the process. I am especially thankful to Dr. Gamze Çakır Kabakcı for her dedicated leadership in the Computational Science and Engineering Laboratory (CSE-Lab) and for the close collaboration we had during the same work. Her

guidance and consistent support have meant a great deal to me. I would also like to thank my colleagues Utku Kaftancıoğlu and Çağatay Kaşar, with whom I shared not only the office but also the challenges, ideas, and achievements of our project group. Their collaboration and friendship made the research journey all the more rewarding.

I am profoundly grateful to my family for their unconditional love and support throughout this journey. I owe my deepest thanks to my mother, Tamam Çelebi, whose selfless sacrifices and unwavering dedication made everything possible. This thesis stands as much as her achievement as it is mine. I am also thankful to my sister, Çiğdem Çamalan, for her constant encouragement, and to my beloved nephew, Taylan Beder, whose presence always brings light and joy into my life.

I would also like to express my sincere gratitude to my dearest friends Ali Can Doğan, Ahmet Calayir, Semih Olgun, Umurcan Tantoğlu and Melih Dağıstan. Our friendship has been a constant source of strength and balance in my life. Their unwavering presence, loyalty and brotherhood mean the world to me, and I am truly fortunate to walk through life with them by my side.

A special thanks goes to my long-time gaming friend Joseph Warburton. Sharing years of fun, challenges and laughter, his friendship has added a lot of joy and entertainment to my life. Gaming with him has always been the perfect way to unwind after long, tiring days.

TABLE OF CONTENTS

ABSTRACT iii

ÖZ v

ACKNOWLEDGMENTS vii

TABLE OF CONTENTS ix

LIST OF TABLES xv

LIST OF FIGURES xvi

LIST OF SYMBOLS xviii

CHAPTER

1 INTRODUCTION 1

1.1 Background 1

1.2 Failure Mechanisms of Turbine Blade 4

1.2.1 Fatigue 4

1.2.2 Oxidation and Corrosion 4

1.2.3 Phase Instability 4

1.3 Scope and Outline 5

2 KINEMATICS OF LARGE DEFORMATION THEORY 7

2.1 Motion of a Body 7

2.1.1 Material(Lagrangian) Description 8

2.1.2 Spatial(Eulerian) Description 9

2.2 Displacement Field 9

2.3 Deformation Gradient 10

2.3.1 Volume Change 11

2.4 Stretch and Rotation 11

2.5 Strain Measures 13
2.5.1 Green-Lagrangian Strain Tensor 13
2.6 Velocity Gradient 14
2.6.1 Symmetric and Skew-Symmetric Part of Velocity Gradient 14
2.6.2 Relationship Between D and $\dot{E}$ 15
2.7 Balance Laws 16
2.7.1 Conservation of Mass 18
2.7.2 Conservation of Linear Momentum 18
2.7.3 Conservation of Angular Momentum 19
2.7.4 Conservation of Energy 20
2.7.5 Conservation of Entropy 22
2.8 Thermodynamic Dissipation, Clausius-Duhem Inequality, and Helmholtz Free Energy 23
2.8.1 Concept of Dissipation 23
2.8.2 Claussius-Duhem Inequality 23
2.8.3 Helmholtz Free Energy 24
3 CRYSTAL PLASTICITY 25
3.1 Historical Evolution of Crystal Plasticity in Metallic Materials 25
3.1.1 Early Empirical Observations of Slip 25
3.1.2 Multi Slip Systems 26
3.1.3 Schmid Law and the Concept of Resolved Shear Stress 27
3.1.4 Development of Crystal Plasticity as a Continuum Framework 29
3.1.5 Relevance to Single Crystal Superalloys 30
3.2 Crystallographic Deformation and Slip System Activation . . 31
3.2.1 Description of Active Slip Systems in FCC Crystals 31
3.2.2 Role of γ and γ' Phases in Accommodating Deformation 32
3.2.3 Partial Dislocation Motion, Stacking Faults, and Glide Barriers 32

3.2.4 Orientation-Dependent Plasticity and Anisotropy . 33
3.3 Thermomechanics of Elastoviscoplastic Single Crystals . . . 33
3.3.1 Balance Laws 33
3.3.2 Specialization of Free Energy Function with Coleman's Exploitation 36
3.3.2.1 Coleman's Exploitation 36
3.3.2.2 Free Energy Function and State Laws . 38
3.3.3 Kinematics of Crystal Plasticity 39
3.3.4 Dissipation and Flow Relations 41
4 HYDROGEN EMBRITTLEMENT IN METALS 42
4.1 Historical Background and Engineering Relevance 42
4.1.1 Engineering Relevance 44
4.1.2 Mechanisms of Hydrogen Embrittlement 45
4.1.2.1 Hydrogen-Enhanced Decohesion (HEDE) 45
4.1.2.2 Hydrogen-Enhanced Localized Plasticity (HELP) 46
4.1.2.3 Adsorption-Induced Dislocation Emission (AIDE) 48
4.1.2.4 Hydride Formation and Precipitation . 48
4.1.2.5 Synergistic Interactions and Plasticity-Mediated Decohesion 49
4.1.3 Hydrogen Transport and Trapping 49
4.1.3.1 Lattice Diffusion and Solubility 50
4.1.3.2 Trapping at Dislocations, Interfaces, and Precipitates 50
4.1.3.3 Thermodynamics of Trapping (Oriani's Model) 51
4.1.3.4 Experimental Methods and Limitations 51
4.1.4 Modeling Approaches for Hydrogen Embrittlement 52
4.1.4.1 Phenomenological and Empirical Models 53
4.1.4.2 Diffusion–Mechanics Coupling Models 54

4.1.4.3 Continuum Damage Mechanics and Failure Criteria 55
4.1.4.4 Crystal Plasticity-Based Formulations 56
4.1.4.5 Fracture Models: Cohesive Zone and Phase-Field Approaches 56
4.1.4.6 Comparative Assessment and Modeling Limitations 57
4.2 Thermodynamical Framework for Coupled Diffusion–Deformation Theory 58
4.2.1 Kinematics 60
4.2.2 Method of Virtual Power and Balance of Forces . . 62
4.2.3 Balance Law for Hydrogen Diffusion 64
4.2.4 Balance Equations 65
4.2.5 Constitutive Equations 66
4.2.6 Oriani's Local Equilibrium Theory 68
4.2.7 Specialization of the Constitutive Equations 70
4.2.7.1 Free Energy 70
4.2.7.2 Hydrogen Trapping 72
4.2.7.3 Lattice Hydrogen Flux 73
4.2.7.4 Balance of Lattice Chemical Potential and Concentration 74
4.2.8 Governing Partial Differential Equations 75
4.3 Numerical Simulations and Discussion 76
4.3.1 J2 Plasticity-Based Modeling and Simulations . . . 76
4.3.1.1 Validation Against Analytical Solution 76
4.3.1.2 Single Edge Notch Simulation 80
4.3.2 Crystal Plasticity-Based Modeling and Simulations 88
4.3.2.1 Single Edge Notch with Crystallographic Anisotropy 88
4.3.2.2 Polycrystalline Tensile Test 93
4.3.3 Polycrystalline Tensile Test 93
4.3.4 Concluding Remarks 98

5 PHASE FIELD MODELING OF FRACTURE 100
5.1 Introduction 100
5.2 Theoretical Background 103
5.2.1 Variational Formulation of Regularized Fracture . . 104
Remark: 105
5.2.1.1 Elastic Energy Contribution at Finite Strain 105
5.2.1.2 Plastic Dissipation at Finite Strain: J2 Plasticity with Linear Isotropic Hardening 106
5.2.1.3 Work Density of Fracture and Total Energy Functional 108
5.2.1.4 Variational Derivation of the Phase-Field Evolution Equation 109
Irreversibility Constraint: 110
Remark on Material Anisotropy: . . . 110
5.3 Numerical Results 111
5.3.1 Single Edge Notched Geometry 111
5.3.2 Effect of Length Scale Parameter l in Brittle Fracture 112
5.3.3 Tension-Compression Split Validation via Shear Loading 113
5.3.4 Stress–Strain Behavior and Fracture Threshold Sensitivity 113
5.3.5 Coupled Damage and Plasticity Evolution 114
5.3.6 Summary 116
REFERENCES 126
APPENDICES
A FINITE ELEMENT IMPLEMENTATION 127
A.1 Time Integration for Hydrogen Diffusion Model 130
A.2 Hydrogen Diffusion Flowchart for UMAT & UMATHT Subroutines 132

A.3 Phase Field Fracture Flowchart for UMAT & UMATHT Subroutines . . . 133
B PARTIAL DIFFERENTIAL EQUATIONS . . . 134
B.1 PDE for Hydrogen . . . 134
B.1.1 Residual Vector . . . 134
B.1.2 Tangent Matrix . . . 135
B.2 PDE for Phase-Field Fracture . . . 135
B.2.1 Residual Vector . . . 136
B.2.2 Tangent Matrix . . . 136
CURRICULUM VITAE . . . 138

LIST OF TABLES

TABLES

Table 4.1 Material properties for the SEN specimen 80

LIST OF FIGURES

FIGURES

Figure 1.1 Schematics of a turbojet engine. 2

Figure 2.1 Reference and deformed configurations of a body. 8

Figure 3.1 Slip lanes on surface of single crystal superalloy under fatigue loading[8]. 26

Figure 3.2 Octahedral slip systems and slip normals $\mathbf{n}^{\alpha}$ and slip directions $\mathbf{m}^{\alpha}$ [26]. 41

Figure 4.1 A, finely crystalline iron under normal conditions. B, same specimen during pickling [29]. 42

Figure 4.2 (a) Schematic of the bar geometry and boundary conditions, (b) Hydrogen diffusion ahead of the boundary. 78

Figure 4.3 Concentration distribution along a bar with different approaches. . . 79

Figure 4.4 (a) Schematic of the blunt-crack geometry and boundary conditions, (b) Mesh around crack tip. 81

Figure 4.5 (a) Equivalent plastic strain. (b) Trapped hydrogen concentration. . 83

Figure 4.6 a) Volumetric strain. (b) Lattice hydrogen concentration. 84

Figure 4.7 (a) Normalized hydrostatic stress ahead of crack tip, (b) Equivalent tensile plastic strain ahead of crack tip. 85

Figure 4.8 (a) Normalized trapped concentration, (b) Normalized lattice concentration ahead of crack tip. 86

Figure 4.9 Equivalent plastic strain 89

Figure 4.10 (a) Equivalent plastic strain. (b) Trapped hydrogen concentration. . 90

Figure 4.11 (a) Equivalent plastic strain. (b) Trapped hydrogen concentration. . 91

Figure 4.12 (a) Equivalent plastic strain. (b) Trapped hydrogen concentration. . 92
Figure 4.13 Polycrystal contains cells with different orientations. 94
Figure 4.14 Boundary conditions and applied load on the geometry. 95
Figure 4.15 (a) Stress distribution. (b) Lattice hydrogen distribution. 96
Figure 4.16 (a) Equivalent plastic strain. (b) Trapped hydrogen concentration. . 97

Figure 5.1 Phase field variable with different length parameter. 104
Figure 5.2 Geometry and boundary conditions for the single edge notched specimen under tensile loading. 111
Figure 5.3 Mesh refinement used to enhance resolution of crack propagation zone. 112
Figure 5.4 Crack profiles in brittle fracture under tension for (left) $l = 0.01$, (middle) $l = 0.02$, and (right) $l = 0.03$. 112
Figure 5.5 Crack propagation under shear loading with $l = 0.02$. Inclined crack confirms that tension-compression split is active. 113
Figure 5.6 Stress–strain response for threshold value 1 MPa. Lower threshold triggers brittle failure. 114
Figure 5.7 Stress–strain response for threshold value 30 MPa. Higher threshold delays damage onset. 114
Figure 5.8 Evolution of damage and plastic strain for threshold = 1 MPa. Damage dominates early, consistent with brittle behavior. 115
Figure 5.9 Evolution of damage and plastic strain for threshold = 30 MPa. Plastic strain accumulates prior to crack initiation. 115

LIST OF SYMBOLS

$\mathcal{B}$	:	Material body
$\mathcal{B}_0$	:	Reference configuration
$\mathcal{B}_t$	:	Current (deformed) configuration
$\mathbf{X}$	:	Material point in reference configuration
$\mathbf{x}$	:	Spatial position in deformed configuration
χ	:	Deformation mapping function
$\dot{\chi}, \ddot{\chi}$	:	Material velocity and acceleration
$\mathbf{u}$	:	Displacement vector
$\mathbf{F}$	:	Deformation gradient tensor
J	:	Jacobian of deformation gradient, $J = \det \mathbf{F}$
$\mathbf{I}$	:	Second-order identity tensor
δ_{ij}	:	Kronecker delta
$\mathbf{U}$	:	Right Cauchy stretch tensor
$\mathbf{V}$	:	Left Cauchy stretch tensor
$\mathbf{R}$	:	Rotation tensor
$\mathbf{C}$	:	Right Cauchy-Green deformation tensor, $\mathbf{C} = \mathbf{F}^{\mathrm{T}}\mathbf{F}$
$\mathbf{B}$	:	Left Cauchy-Green deformation tensor, $\mathbf{B} = \mathbf{F}\mathbf{F}^{\mathrm{T}}$
$\mathbf{E}$	:	Green-Lagrange strain tensor, $\mathbf{E} = \frac{1}{2}(\mathbf{C} - \mathbf{I})$
$\mathbf{L}$	:	Velocity gradient tensor, $\mathbf{L} = \nabla \mathbf{v}$
$\mathbf{D}$	:	Rate-of-deformation tensor, $\mathbf{D} = \frac{1}{2}(\mathbf{L} + \mathbf{L}^{\mathrm{T}})$
$\mathbf{W}$	:	Spin tensor, $\mathbf{W} = \frac{1}{2}(\mathbf{L} - \mathbf{L}^{\mathrm{T}})$

ρ : Mass density

$\mathbf{v}$: Velocity vector

$\mathbf{a}$: Acceleration, $\mathbf{a} = \dot{\mathbf{v}}$

$\mathbf{b}$: Body force per unit mass

$\mathbf{t}$: Traction vector

$\boldsymbol{\sigma}$: Cauchy stress tensor

e : Specific internal energy

η : Specific entropy

r : Heat supply per unit mass

h : Heat flux per unit area

$\mathbf{q}$: Heat flux vector

θ : Absolute temperature

γ : Entropy production per unit mass

ψ : Helmholtz free energy, $\psi = e - \theta\eta$

$\boldsymbol{\varepsilon}$: Infinitesimal strain tensor, $\boldsymbol{\varepsilon} = \frac{1}{2}(\nabla\mathbf{u} + \nabla^{\mathrm{T}}\mathbf{u})$

$\dot{\mathbf{E}}$: Time derivative of Green-Lagrange strain

Γ : Total entropy production

H : Total entropy

K : Kinetic energy

E : Internal energy

P : Mechanical power

Q : Thermal power

S : Entropy power

m	:	Total mass
$\mathbf{I}$	:	Total linear momentum
$\mathbf{D}_0$	:	Total angular momentum
$\nabla(\cdot)$	:	Gradient operator
$\mathrm{div}(\cdot)$	:	Divergence operator
τ	:	Resolved shear stress
ϕ	:	Angle between slip plane normal and applied stress
λ	:	Angle between slip direction and applied stress
m	:	Schmid factor
τ_{crit}	:	Critical resolved shear stress (CRSS)
ρ_0	:	Reference mass density
$\mathbf{D}_{\mathrm{loc}}$	:	Local mechanical dissipation
$\mathbf{D}_{\mathrm{cond}}$	:	Conductive dissipation
$\boldsymbol{\beta}$	:	Thermodynamic force conjugate to $\boldsymbol{\varepsilon}^p$
$\boldsymbol{g}$	:	Temperature gradient
$\boldsymbol{\varepsilon}^p$	:	Plastic strain tensor
ϱ^α	:	Isotropic hardening variable for slip system α
$\mathbb{C}$	:	Fourth-order elasticity tensor (cubic symmetry)
r_0	:	Initial slip resistance
q	:	Hardening coefficient
$h^{r\alpha}$	:	Latent hardening matrix
r^α	:	Slip resistance on slip system α
$\mathbf{F}^e$	:	Elastic part of deformation gradient
$\mathbf{F}^p$	:	Plastic part of deformation gradient

$\mathbf{R}^e$	:	Elastic rotation tensor
$\mathbf{U}^e$	:	Elastic right stretch tensor
$\mathbf{C}^e$	:	Elastic right Cauchy-Green tensor
$\mathbf{E}^e$	:	Elastic Hencky strain tensor
C_{11}, C_{12}, C_{44}	:	Elastic constants in Voigt notation
μ'	:	Effective shear modulus
$\mathbf{D}^p$	:	Plastic stretching tensor
$\dot{\gamma}^\alpha$	:	Slip rate on slip system α
$\mathbf{m}^\alpha$	:	Slip direction for system α
$\mathbf{n}^\alpha$	:	Slip plane normal for system α
n	:	Rate sensitivity exponent
ρ^α	:	Nonlinear isotropic hardening variable
b	:	Saturation rate parameter
$\mathcal{D}$	:	Mechanical dissipation
f^α	:	Yield function for slip system α
$\dot{\gamma}_0$	:	Reference slip rate
W_B	:	Trap binding energy
K_T	:	Equilibrium constant for trapping
θ_L	:	Lattice site occupancy
θ_T	:	Trap site occupancy
N_L	:	Number of solvent atoms per unit volume
N_T	:	Number of traps per unit volume
$\mathbf{N}^p$	:	Direction of plastic flow
$\widetilde{N_T}$	:	Trap density as function of plastic strain

CHAPTER 1

INTRODUCTION

1.1 Background

The development of the gas turbine and turbojet engine in the early 20th century quickly revealed that materials for the ”hot section” the combustion chamber and turbine, were a critical limiting factor [1]. Early jet engines suffered blade failures and performance limitations due to the inability of conventional steel alloys to withstand the high temperatures and stresses inside the turbine. This challenge spurred intensive research into new high-temperature materials during and after World War II [1]. A major breakthrough was the introduction of nickel-based superalloys in the 1940s. For example, Nimonic 75, an 80%Ni–20%Cr alloy with minor titanium and carbon, was first used for the turbine blades in Sir Frank Whittle's prototype jet engine [1]. This alloy and its successors offered significantly better strength and corrosion resistance at temperature than earlier blade materials, enabling higher turbine inlet temperatures and improved engine performance. Indeed, the thermal efficiency of a gas turbine improves as the turbine entry temperature (TET) rises [2], so any increase in allowable blade temperature translates to a more powerful and efficient engine. Thanks to advances in alloy chemistry and processing (e.g. vacuum melting to remove impurities in the 1950s), the temperature capability of turbine blades steadily increased [3]. Early turbojets could only handle turbine temperatures on the order of 820 °C, whereas modern engines run gas temperatures exceeding 1370 °C in the first-stage turbine [2]. Modern high-pressure turbine blades made of nickel superalloys can sustain *metal* temperatures on the order of 1050 °C with local hot spots approaching 1200 °C, roughly 85–90% of the alloy's melting point [2].

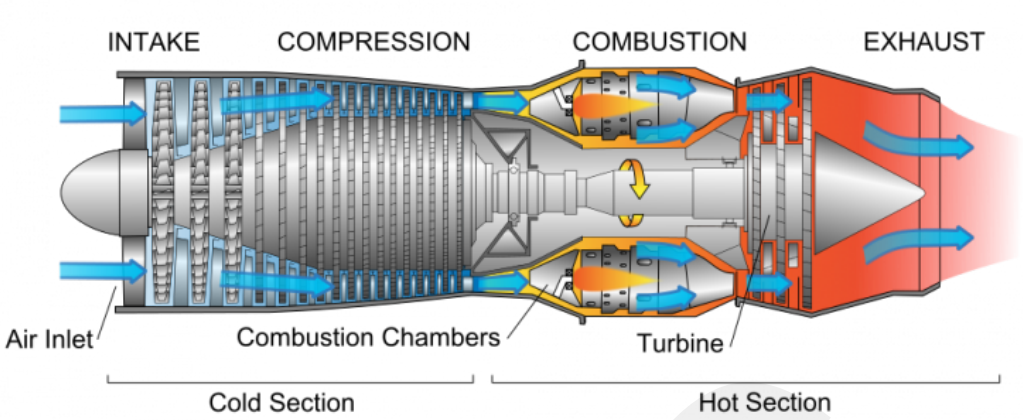


Figure 1.1: Schematics of a turbojet engine.

Nickel-based superalloys have become the material of choice for turbine blades because of their unique ability to retain strength at elevated temperatures. Nickel retains an austenitic face-centered cubic (FCC) crystal structure up to its melting point, providing a stable matrix (the "γ" phase) to which many other elements can be alloyed [3]. The defining feature of Ni-based superalloys is the precipitation of an ordered intermetallic phase known as gamma-prime (γ'). When a sufficient amount of aluminum (and/or titanium) is added to nickel, a second phase with the nominal composition Ni_3Al forms as finely dispersed nanometer-scale precipitates throughout the nickel matrix [2]. This γ' phase has an L1_2 crystal structure and is coherent with the matrix, meaning it interfaces with little lattice strain. The coherent γ/γ' microstructure is the cornerstone of superalloy strength: the hard γ' precipitates impede the motion of dislocations especially at high temperatures where normal alloys would soften [3].

Over the decades, major metallurgical advancements have incrementally pushed the performance of turbine blades. One such advance was in casting and solidification control. Early superalloy blades were cast polycrystals with many random grain boundaries, which at high temperatures became weak links, grain boundaries are prone to sliding, cavitation, and diffusion, leading to creep and fatigue damage accumulation [3]. Engineers discovered that aligning or eliminating grain boundaries would improve high-temperature capability. In the 1960s, directional solidification (DS) techniques were developed, casting blades with columnar grains all oriented along the major stress axis. This removed transverse grain boundaries and markedly increased creep rupture lives.

By the 1980s, further refinement led to single-crystal (SC) blades grown as one continuous crystal with no grain boundaries at all [2]. The elimination of grain boundaries was revolutionary: the single-crystal blades displayed vastly improved creep resistance and much greater resilience against thermal fatigue and oxidation since there were no boundary regions to act as fast-diffusion paths or crack initiation sites [3].

The chemical composition of superalloys has also been refined over successive generations. First-generation single-crystal superalloys had no rhenium (Re), while second- and third-generation variants introduced 2–6% Re to improve creep resistance. However, high levels of refractory elements, especially Re and W, promote the formation of topologically close-packed (TCP) phases, brittle intermetallics that deplete strengthening elements from the matrix and significantly reduce ductility and fatigue resistance [4, 5]. To mitigate this, fourth-generation superalloys incorporated small amounts of ruthenium (Ru), which suppresses TCP phase formation and improves phase stability over long-term operation [4].

In parallel, thermal and environmental protection technologies were developed. Internal cooling passages and film cooling techniques allow air from the compressor to flow through the blade, reducing metal temperatures. The application of thermal barrier coatings (TBCs), typically composed of a ceramic topcoat (e.g., yttria-stabilized zirconia) and a metallic bond coat (such as MCrAlY), further protects the blade from thermal and oxidative damage. These TBC systems have been shown to reduce surface metal temperatures by over 100 °C and significantly extend component life [6].

Despite these advancements, turbine blades still face a variety of failure mechanisms. Among them, creep, the time-dependent plastic deformation under sustained load at high temperature, remains a primary concern. Even small deformations can affect the aerodynamic profile of blades, causing efficiency losses or catastrophic failure. The γ' precipitates and single-crystal structures are crucial in suppressing creep, but long-term exposure still results in microstructural evolution such as rafting, coarsening, and ultimately material degradation [3].

1.2 Failure Mechanisms of Turbine Blade

1.2.1 Fatigue

Fatigue, both low-cycle (LCF) and high-cycle (HCF), is another critical issue. LCF arises due to cyclic thermal strains during engine start-up and shutdown, while HCF is caused by vibrational stresses during steady-state operation. Fatigue cracks often initiate at surface imperfections, cooling holes, or microstructural features such as pores or inclusions. In service, these cracks may propagate rapidly under the influence of thermal gradients, centrifugal loading, and environmental conditions.

1.2.2 Oxidation and Corrosion

Oxidation and corrosion are also significant degradation mechanisms. While superalloys form protective oxide layers (typically alumina or chromia), exposure to contaminants like sulfur, sodium, and vanadium can lead to hot corrosion, which disrupts the protective scale and accelerates material loss. Type I hot corrosion occurs at high temperatures (>800 °C), while Type II occurs at lower temperatures (600–800 °C). The selection of alloying elements and the application of coatings are key strategies for mitigating these effects [3, 6].

1.2.3 Phase Instability

Phase instability over time is another concern, particularly the formation of TCP phases. These brittle intermetallics, which form after long-term exposure to high temperatures, reduce mechanical properties and act as crack initiation sites. Their suppression through careful alloy design, including the addition of Ru, is an ongoing area of research and development [4, 5].

In conclusion, the historical development of turbojet engines has been inextricably linked to the evolution of turbine blade materials. From early failures of steel alloys to the sophisticated single-crystal, Re- and Ru-containing superalloys of today, progress in material science has enabled the dramatic performance improvements seen in modern gas turbines. The careful balance between strength, toughness, oxidation resistance, and microstructural stability defines the success of these components. Understanding the interplay between materials development and failure mechanisms is critical for further advances in jet engine performance and durability.

1.3 Scope and Outline

This thesis is devoted to the modeling and simulation of hydrogen embrittlement in metallic materials at the single crystal level, with a particular focus on large deformation kinematics, crystal plasticity, and phase-field modeling of fracture. The central aim is to develop a thermodynamically consistent, finite strain framework capable of capturing the coupled effects of mechanical deformation and hydrogen diffusion on fracture behavior. The scope spans theoretical derivations, constitutive modeling, and numerical implementations grounded in continuum mechanics and thermodynamics.

The thesis is organized as follows:

- **Chapter 2** introduces the kinematics of large deformation theory, including the formulation of deformation gradients, strain measures, and the velocity gradient tensor. The chapter also presents the fundamental balance laws and thermodynamic restrictions, culminating in the Clausius-Duhem inequality and the Helmholtz free energy function.
- **Chapter 3** outlines the historical development of crystal plasticity theory for metallic materials. It discusses the crystallographic basis of plastic deformation, including slip system activation, and develops a thermomechanically consistent formulation of elastoviscoplastic behavior in single crystals.

- **Chapter 4** focuses on hydrogen embrittlement in metals. It begins with a historical overview and engineering context, followed by the derivation of a coupled diffusion–deformation theory within a thermodynamic framework. This chapter concludes with representative numerical simulations and discussions.

- **Chapter 5** presents the phase-field modeling approach for fracture. Theoretical foundations and governing equations are introduced, followed by numerical results that demonstrate the ability of the model to simulate complex fracture patterns, including those induced by hydrogen-assisted degradation.

Through this structured development, the thesis aims to establish a computationally robust modeling framework validated thorugh analytical solutions and experiments for understanding and predicting failure mechanisms in hydrogen-charged single crystal metals.

CHAPTER 2

KINEMATICS OF LARGE DEFORMATION THEORY

2.1 Motion of a Body

Consider a homogeneous body $\mathcal{B}$ in a three dimensional Euclidean space $\mathbf{R^3}$ is a collection of infinitely many points. At a fixed time t_0, any arbitrary point $\mathbf{X}$ on that body is called material point and occupied region by the body is reference configuration. A motion of any point on $\mathcal{B}$ at a given time t can be mapped with a smooth function

$$\mathbf{x} = \chi(\mathbf{X}, \mathbf{t}) \tag{2.1}$$

to spatial configuration (deformed configuration). The mapping function χ, takes any point from the reference configuration $\mathcal{B}$, to a deformed configuration $\mathcal{B}_{\sqcup}$, may also be called deformation mapping.The material point $\mathbf{X}$ will occupy different points in the deformed configuration throughout the motion. Since the deformation map is one-to-one and bijective, it has a unique inverse

$$\mathbf{X} = \chi^{-1}(\mathbf{x}, \mathbf{t}) \tag{2.2}$$

Any material point which passes through a point in deformed configuration has the velocity and acceleration

$$\dot{\chi} = \frac{\partial \chi(\mathbf{X}, t)}{\partial t} \quad \text{and} \quad \ddot{\chi} = \frac{\partial^2 \chi(\mathbf{X}, t)}{\partial t^2} \tag{2.3}$$

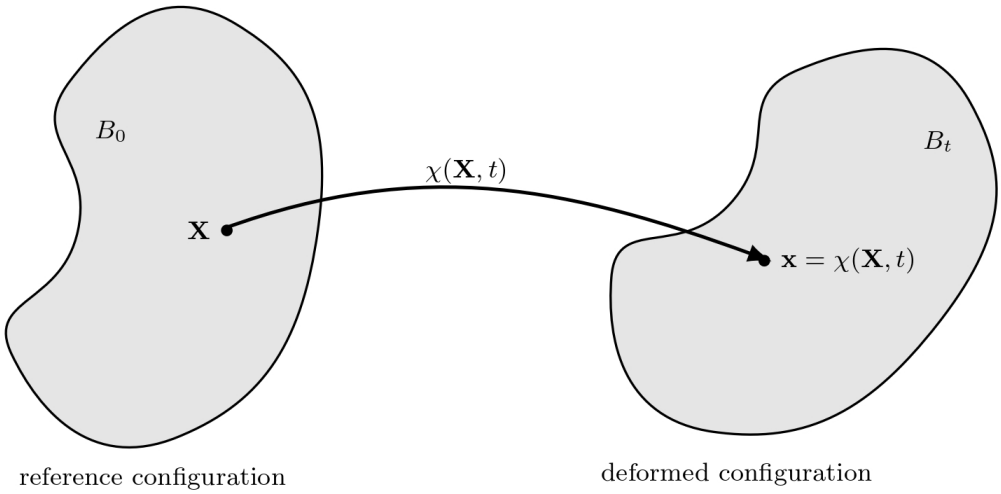


Figure 2.1: Reference and deformed configurations of a body.

2.1.1 Material(Lagrangian) Description

Let a function defined in deformed configuration depends on reference coordinates **X** and t so that

$$f(\mathbf{X}, t) \tag{2.4}$$

called a lagrangian form of a function. Taking the time derivative of this function will yield

$$\frac{df(\mathbf{X}, t)}{dt} = \frac{\partial f(\mathbf{X}, t)}{\partial t} \tag{2.5}$$

only when the material point **X** held fixed. By the same logic, the lagrangian form of the velocity and acceleration of a motion are

$$\dot{\chi} = \frac{\partial \chi(\mathbf{X}, t)}{\partial t} \quad \text{and} \quad \ddot{\chi} = \frac{\partial^2 \chi(\mathbf{X}, t)}{\partial t^2} \tag{2.6}$$

2.1.2 Spatial(Eulerian) Description

A function defined in material coordinates can be reparameterized in terms of spatial coordinates **x** as

$$f(\mathbf{X}, t)) = f(\chi^{-1}(\mathbf{x}, t), t) \tag{2.7}$$

and called a Eulerian form of a function. Taking the time derivative of this function will yield

$$\frac{df(\mathbf{x}, t)}{dt} = \frac{\partial f(\chi^{-1}(\mathbf{x}, t), t)}{\partial t} \tag{2.8}$$

Then the Eulerian form of the velocity and acceleration of a motion are

$$\dot{\chi} = \frac{\partial \chi(\chi^{-1}(\mathbf{x}, t), t)}{\partial t} \quad \text{and} \quad \ddot{\chi} = \frac{\partial^2 \chi(\chi^{-1}(\mathbf{x}, t), t)}{\partial t^2} \tag{2.9}$$

2.2 Displacement Field

In continuum mechanics, the deformation of the body is refer to the displacement of the material points from reference configuration to deformed configuration. The displacement of any point is

$$\mathbf{u}(\mathbf{X}, t) = \mathbf{x} - \mathbf{X} = \chi(\mathbf{X}, t) - \mathbf{X} \tag{2.10}$$

defined in the lagrangian space or in Eulerian space as

$$\mathbf{u}(\mathbf{x}, t) = \mathbf{x} - \mathbf{X} = \mathbf{x} - \chi^{-1}(\mathbf{x}, t) \tag{2.11}$$

2.3 Deformation Gradient

Consider a material line has the length d$\mathbf{X}$ lies on the reference configuration. At time t material line happen to be occupy a space in deformed configuration as d$\mathbf{x}$ so that any infinitesimal change on d$\mathbf{X}$ at a fixed time and by the definition of deformation mapping, is give

$$\mathrm{d}\mathbf{x} = \frac{\partial \mathbf{x}(\mathbf{X})}{\partial \mathbf{X}} \mathrm{d}\mathbf{X} \tag{2.12}$$

From here the deformation gradient can be defined as

$$\mathbf{F} = \frac{\partial \mathbf{x}}{\partial \mathbf{X}} = \nabla \mathbf{x} \quad \text{or} \quad \mathrm{d}\mathbf{x} = \mathbf{F}\mathrm{d}\mathbf{X} \tag{2.13}$$

The deformation gradient defines the relation between the reference configuration and the deformed configuration with equation 2.13.

At this point let us define the determinant of $\mathbf{F}$ which is nothing but a Jacobian of the motion denoted by

$$J = |\mathbf{F}| = \det\mathbf{F} \tag{2.14}$$

to express the volume change of the body. If the determinant of deformation gradient is 1 that means $\mathbf{F} = \mathbf{I}$, where $\mathbf{I}$ is second order identity tensor and has the property

$$\delta_{ij} = \begin{cases} 1 & \text{for} \quad i = j \\ 0 & \text{for} \quad i \neq j \end{cases} \tag{2.15}$$

then the volume is preserved and the deformation is said to be isochoric.

2.3.1 Volume Change

Let us define a volume element in reference configuration with three line elements having position vector $\mathbf{X}$ by using triple scalar product. Then the volume is

$$\begin{aligned} \mathrm{d}V &= \mathrm{d}\mathbf{X}^1 \cdot \mathrm{d}\mathbf{X}^2 \times \mathrm{d}\mathbf{X}^3 \\ &= (\mathrm{d}X^1\mathbf{e}_1) \cdot (\mathrm{d}X^2\mathbf{e}_2) \times (\mathrm{d}X^3\mathbf{e}_3) \\ &= \mathrm{d}X^1\mathrm{d}X^2\mathrm{d}X^3(\mathbf{e}_1 \cdot (\mathbf{e}_2 \times \mathbf{e}_3)) \end{aligned} \tag{2.16}$$

where $\mathbf{e}_i$ refers to the unit vector along the $\mathrm{d}\mathbf{X}^i$. Then the deformed volume is given as

$$\begin{aligned} \mathrm{d}v &= \mathrm{d}\mathbf{x}^1 \cdot \mathrm{d}\mathbf{x}^2 \times \mathrm{d}\mathbf{x}^3 \\ &= (\mathrm{d}X^1(\mathbf{F} \cdot \mathbf{e}_1)) \cdot (\mathrm{d}X^2(\mathbf{F} \cdot \mathbf{e}_2)) \times (\mathrm{d}X^3(\mathbf{F} \cdot \mathbf{e}_3)) \\ &= |F|\mathrm{d}X^1\mathrm{d}X^2\mathrm{d}X^3 = J\mathrm{d}V \end{aligned} \tag{2.17}$$

2.4 Stretch and Rotation

The deformation gradient contains the stretch and rotation. Assume a line element $\mathrm{d}\mathbf{X}$, undergoes a deformation which involves both stretch and rotation such that

$$\mathrm{d}\mathbf{X}' = \mathbf{U}\mathrm{d}\mathbf{X} \quad \text{and} \quad \mathrm{d}\mathbf{x} = \mathbf{R}\mathrm{d}\mathbf{X}' \tag{2.18}$$

There exist a theorem called polar decomposition relates the deformation gradient and these two tensors in a multiplicative way as follows

$$\mathbf{F} = \mathbf{RU} = \mathbf{VR} \tag{2.19}$$

where **U** is right Cauchy stretch tensor, **V** is left Cauchy stretch tensor and **R** is rotation tensor. Note that, **U** and **V** are symmetric and positive definite and **R** is an orthogonal tensor and have the following properties

$$\mathbf{R}\mathbf{R}^{\mathrm{T}} = \mathbf{I}, \quad \mathbf{U} = \mathbf{U}^{\mathrm{T}}, \quad \mathbf{V} = \mathbf{V}^{\mathrm{T}} \tag{2.20}$$

In equation 2.18, a pure stretch is applied with **U**d**X** which means the angle between the line elements is not changing. The line elements either elongates or shorten but does not rotate. The operation **U** is followed by **R** to apply rotation to the stretched element, **RU**d**X**.

Before moving further it is better to describe Cauchy-Green tensors. By help of the equations 2.19 and 2.20

$$\mathbf{U} = \mathbf{R}^{-1} \cdot \mathbf{F} = \mathbf{R}^{\mathrm{T}} \cdot \mathbf{F}, \quad \mathbf{V} = \mathbf{F} \cdot \mathbf{R}^{-1} = \mathbf{F} \cdot \mathbf{R}^{\mathrm{T}} \tag{2.21}$$

and

$$\begin{aligned} \mathbf{U}^2 &= \mathbf{U} \cdot \mathbf{U} \\ &= \mathbf{U}^{\mathrm{T}} \cdot \mathbf{U} \\ &= \mathbf{F}^{\mathrm{T}} \cdot (\mathbf{R} \cdot \mathbf{R}^{-1}) \cdot \mathbf{F} \\ &= \mathbf{F}^{\mathrm{T}} \cdot \mathbf{F} = \mathbf{C} \end{aligned} \tag{2.22}$$

By following the same steps one can come up with

$$\mathbf{B} = \mathbf{F} \cdot \mathbf{F}^{\mathrm{T}} \tag{2.23}$$

here **C** is *Right Cauchy-Green Deformation Tensor* and **B** is *Left Cauchy-Green Deformation Tensor*.

2.5 Strain Measures

Consider a line element d$\mathbf{X}$ and two material point on this element A and B in the reference configuration. These points are gonna occupy positions $\overline{\mathrm{A}}$ and $\overline{\mathrm{B}}$ in the deformed configuration. To show the change in the length of line element as material deforms, the distance between the points for each configuration is given

$$(\mathrm{d}S)^2 = \mathrm{d}\mathbf{X}^{\mathrm{T}} \cdot \mathrm{d}\mathbf{X} \tag{2.24}$$

$$\begin{aligned}(\mathrm{d}s)^2 &= \mathrm{d}\mathbf{x}^{\mathrm{T}} \cdot \mathrm{d}\mathbf{x} \\ &= \mathrm{d}\mathbf{X}^{\mathrm{T}} \cdot (\mathbf{F}^{\mathrm{T}}\mathbf{F}) \cdot \mathrm{d}\mathbf{X}\end{aligned} \tag{2.25}$$

It is known that from equation 2.22, $\mathbf{C} = \mathbf{F}^{\mathrm{T}} \cdot \mathbf{F}$. So that equation 2.25

$$\mathrm{d}\mathbf{X}^{\mathrm{T}} \cdot (\mathbf{F}^{\mathrm{T}}\mathbf{F}) \cdot \mathrm{d}\mathbf{X} = \mathrm{d}\mathbf{X}^{\mathrm{T}} \cdot \mathbf{C} \cdot \mathrm{d}\mathbf{X} \tag{2.26}$$

2.5.1 Green-Lagrangian Strain Tensor

The change in square length in a line element $(\mathrm{d}s)^2 - (\mathrm{d}S)^2$ can be expressed as in terms of either materials points from reference configuration or deformed configuration. Considering the change in terms of reference configuration

$$(\mathrm{d}s)^2 - (\mathrm{d}S)^2 = \mathrm{d}\mathbf{X}^{\mathrm{T}} \cdot (\mathbf{C} - \mathrm{I}) \cdot \mathrm{d}\mathbf{X} \tag{2.27}$$

By definition,

$$\mathbf{E} = \frac{1}{2}(\mathbf{C} - \mathrm{I}) \tag{2.28}$$

is called the *Green-Lagrangian Strain Tensor*. Note that Green-Lagrangian Strain Tensor is also symmetric, $\mathbf{E} = \mathbf{E}^{\mathrm{T}}$.

2.6 Velocity Gradient

Let us recall the line element from deformed configuration d$\mathbf{x}$ two material points $\overline{\mathrm{A}}$ and $\overline{\mathrm{B}}$ in the neighbourhood of that line element. Writing the velocity around the point $\overline{\mathrm{A}}$ is

$$\mathrm{d}\mathbf{v} = \frac{\partial \mathbf{v}(\mathbf{x}, t)}{\partial \mathbf{x}} \mathrm{d}\mathbf{x} \tag{2.29}$$

From here the velocity gradient tensor can be written as

$$\mathbf{L} = \nabla \mathbf{v} = \frac{\partial \mathbf{v}(\mathbf{x}, t)}{\partial \mathbf{x}} \tag{2.30}$$

Rewriting the equation 2.29 as

$$\mathrm{d}\mathbf{v} = \mathbf{L}\mathrm{d}\mathbf{x} \tag{2.31}$$

will give the relative velocity between points $\overline{\mathrm{A}}$ and $\overline{\mathrm{B}}$.

2.6.1 Symmetric and Skew-Symmetric Part of Velocity Gradient

Let us decompose the velocity gradient tensor into its symmetric and skew-symmetric parts as

$$\mathbf{L} = \mathbf{D} + \mathbf{W} \tag{2.32}$$

Where $\mathbf{D}$ is called rate of deformation (stretching) tensor which describes rate of deformation in the vicinity of material point in deformed configuration and $\mathbf{W}$ is called spin tensor which describes local rigid body rotation in the neighbourhood of material point in deformed configuration. It follows that

$$\mathbf{D} = \frac{1}{2}(\mathbf{L} + \mathbf{L}^{\mathrm{T}}), \qquad \mathbf{W} = \frac{1}{2}(\mathbf{L} - \mathbf{L}^{\mathrm{T}}) \tag{2.33}$$

2.6.2 Relationship Between D and $\dot{\mathbf{E}}$

The well-known relation between the material time derivative of the Green-Lagrange strain tensor and the rate-of-deformation tensor is given by

$$\dot{\mathbf{E}} = \mathbf{F}^{\mathrm{T}} \cdot \mathbf{D} \cdot \mathbf{F} \tag{2.34}$$

This expression provides a direct link between the strain rate in the reference configuration and the symmetric part of the spatial velocity gradient.

Next, reconsidering the definition of deformation gradient and taking the time derivative

$$\begin{aligned} \frac{\mathrm{d}}{\mathrm{d}t}\mathrm{d}\mathbf{x} &= \frac{\mathrm{d}}{\mathrm{d}t}(\mathbf{F}\mathrm{d}\mathbf{X}) \\ &= \frac{\mathrm{d}\mathbf{F}}{\mathrm{d}t}\mathrm{d}\mathbf{X} + 0 \end{aligned} \tag{2.35}$$

and from equation 2.31 and equation 2.35

$$\dot{\mathbf{F}}\mathrm{d}\mathbf{X} = \mathbf{L}\mathrm{d}\mathbf{x} \tag{2.36}$$

finally leads

$$\mathbf{L} = \dot{\mathbf{F}}\mathbf{F}^{-1} \tag{2.37}$$

2.7 Balance Laws

Starting with some physical definitions

$$
\begin{aligned}
&\text{(i) Mass} && m := \int_{\mathcal{B}} \mathrm{d}m = \int_{\mathcal{B}} \rho \, \mathrm{d}V \\
&\text{(ii) Linear Momentum} && \mathbf{I} := \int_{\mathcal{B}} \rho \mathbf{v} \, \mathrm{d}V \\
&\text{(iii) Angular Momentum} && \mathbf{D}_0 := \int_{\mathcal{B}} \mathbf{x} \times \rho \mathbf{v} \, \mathrm{d}V \\
&\text{(iv) Kinetic Energy} && K := \int_{\mathcal{B}} \frac{1}{2} \rho |\mathbf{v}|^2 \, \mathrm{d}V \\
&\text{(v) Internal Energy} && E := \int_{\mathcal{B}} \rho e \, \mathrm{d}V \\
&\text{(vi) Entropy} && H := \int_{\mathcal{B}} \rho \eta \, \mathrm{d}V \\
&\text{(vii) Entropy Production} && \Gamma := \int_{\mathcal{B}} \rho \gamma \, \mathrm{d}V
\end{aligned}
\tag{2.38}
$$

The integral expressions above provide the total physical quantities over the body $\mathcal{B}$, such as mass, momentum, energy, and entropy, in terms of their respective field variables. While these quantities characterize the overall state of the system, it is equally important to account for the external actions and interactions that drive the evolution of the system over time. These include the mechanical forces and couples acting on the body, as well as the rates of energy and entropy transfer due to mechanical and thermal processes.

Accordingly, the following set of integral relations define the corresponding external power and flux terms, mechanical force, mechanical couple, mechanical power, thermal power, and entropy power which govern the exchange of energy and entropy between the body and its surroundings:

(i) Mechanical Force $\mathbf{F} := \int_{\mathcal{B}} \rho \mathbf{b} \, \mathrm{d}V + \int_{\partial \mathcal{P}} \mathbf{t} \, \mathrm{d}A$

(ii) Mechanical Couple $\mathbf{M}_0 := \int_{\mathcal{B}} \mathbf{x} \times \rho \mathbf{b} \, \mathrm{d}V + \int_{\partial \mathcal{B}} \mathbf{x} \times \mathbf{t} \, \mathrm{d}A$

(iii) Mechanical Power $P := \int_{\mathcal{B}} \rho \mathbf{b} \cdot \mathbf{v} \, \mathrm{d}V + \int_{\partial \mathcal{B}} \mathbf{t} \cdot \mathbf{v} \, \mathrm{d}A$ (2.39)

(iv) Thermal Power $Q := \int_{\mathcal{B}} \rho r \, \mathrm{d}V - \int_{\partial \mathcal{B}} h \, \mathrm{d}A$

(v) Entropy Power $S := \int_{\mathcal{B}} \rho \frac{r}{\theta} \, \mathrm{d}V - \int_{\partial \mathcal{B}} \frac{h}{\theta} \, \mathrm{d}A$

The relationship between the field equations and the external loads is then given as

(i) Conservation of Mass (closed system) $\frac{dm}{dt} = 0$

(ii) Conservation of Linear Momentum $\frac{d\mathbf{I}}{dt} = \mathbf{F}$

(iii) Conservation of Angular Momentum $\frac{d\mathbf{D}_0}{dt} = \mathbf{M}_0$ (2.40)

(iv) Conservation of Energy (1^{st} Law) $\frac{d}{dt}(K + E) = P + Q$

(v) Conservation of Entropy (2^{nd} Law) $\Gamma = \frac{dH}{dt} - S \geq 0$

2.7.1 Conservation of Mass

The conservation of mass states that the total mass of a closed system remains constant over time. For a material body $\mathcal{B}$, this requirement is expressed by setting the time derivative of the total mass to zero

$$\frac{d}{dt}(m) = \frac{d}{dt}\int_{\mathcal{B}} \rho \, dV = \int_{\mathcal{B}} \dot{\rho} \, dV = 0 \tag{2.41}$$

In local form, this implies that the material time derivative of the density must vanish, i.e.,

$$\dot{\rho} = 0 \tag{2.42}$$

meaning the mass density of each material point does not change as the body evolves.

2.7.2 Conservation of Linear Momentum

The conservation of linear momentum states that the change in total momentum equals the sum of external forces acting on the body. This leads to the local balance equation, which relates the acceleration of a material point to the internal stresses and body forces.

$$\frac{d}{dt}\int_{\mathcal{B}} \rho \mathbf{v} \, dV = \int_{\mathcal{B}} (\dot{\rho}\mathbf{v} + \rho\dot{\mathbf{v}}) \, dV = \int_{\mathcal{B}} \rho \mathbf{b} \, dV + \int_{\partial\mathcal{B}} \mathbf{t} \, dA \tag{2.43}$$

where the surface integral can be written as

$$\int_{\partial\mathcal{B}} \mathbf{t} \, dA = \int_{\partial\mathcal{B}} \boldsymbol{\sigma}\mathbf{n} \, dA = \int_{\mathcal{B}} \operatorname{div} \boldsymbol{\sigma} \, dV \tag{2.44}$$

Insertion yields

$$\int_{\mathcal{B}} (\dot{\rho}\mathbf{v} + \rho\dot{\mathbf{v}}) \, dV = \int_{\mathcal{B}} (\rho\mathbf{b} + \operatorname{div} \boldsymbol{\sigma}) \, dV \tag{2.45}$$

where it can be substituted the conservation of mass. The localization of the latter integral

$$\lim_{\mathcal{B}\to dV} \int_{\mathcal{B}} (\rho\dot{\mathbf{v}} - \operatorname{div}\boldsymbol{\sigma} - \rho\mathbf{b})\, dV = 0 \tag{2.46}$$

then yields the well-known local form of the conservation of linear momentum

$$\rho\dot{\mathbf{v}} = \rho\mathbf{a} = \operatorname{div}\boldsymbol{\sigma} + \rho\mathbf{b} \tag{2.47}$$

governing the local stress equilibrium at a material point.

2.7.3 Conservation of Angular Momentum

The conservation of angular momentum requires that the rate of change of total angular momentum of the body equals the sum of the moments of external forces. For a material body $\mathcal{B}$, this is expressed as

$$\frac{d}{dt}\int_{\mathcal{B}} \rho\,\mathbf{x}\times\mathbf{v}\, dV = \int_{\mathcal{B}} \rho\,\mathbf{x}\times\mathbf{b}\, dV + \int_{\partial\mathcal{B}} \mathbf{x}\times\mathbf{t}\, dA \tag{2.48}$$

where $\mathbf{x}$ is the position vector, and $\times$ denotes the cross product.

Using the traction vector $\mathbf{t} = \boldsymbol{\sigma}\mathbf{n}$ and applying the divergence theorem,

$$\int_{\partial\mathcal{B}} \mathbf{x}\times(\boldsymbol{\sigma}\mathbf{n})\, dA = \int_{\mathcal{B}} \operatorname{div}(\mathbf{x}\times\boldsymbol{\sigma})\, dV \tag{2.49}$$

By expanding and applying product rules, this becomes

$$\operatorname{div}(\mathbf{x}\times\boldsymbol{\sigma}) = \mathbf{x}\times(\operatorname{div}\boldsymbol{\sigma}) + \boldsymbol{\sigma}^T - \boldsymbol{\sigma} \tag{2.50}$$

Using the local balance of linear momentum (previous section), and substituting, the integral form reduces to

$$\int_{\mathcal{B}} \left[(\boldsymbol{\sigma}^T - \boldsymbol{\sigma}) \right] dV = 0 \tag{2.51}$$

Since this must hold for any part $\mathcal{B}$, the localization yields

$$\boldsymbol{\sigma} = \boldsymbol{\sigma}^T \tag{2.52}$$

which states that the Cauchy stress tensor is symmetric.

2.7.4 Conservation of Energy

$$\frac{d}{dt}[K + E] = P + Q \tag{2.53}$$

$$\frac{d}{dt}\left[\int_{\mathcal{B}} \frac{1}{2}\rho |\mathbf{v}|^2 \, dV + \int_{\mathcal{B}} \rho e \, dV \right] = \int_{\mathcal{B}} \rho \mathbf{b} \cdot \mathbf{v} \, dV + \int_{\partial\mathcal{B}} \mathbf{t} \cdot \mathbf{v} \, dA + \int_{\mathcal{B}} \rho r \, dV - \int_{\partial\mathcal{B}} h \, dA \tag{2.54}$$

The surface integrals transformed into volume integrals:

$$\begin{aligned} \int_{\partial\mathcal{B}} \mathbf{v} \cdot \mathbf{t} \, dA &= \int_{\partial\mathcal{B}} \mathbf{v} \cdot (\boldsymbol{\sigma}\mathbf{n}) \, dA = \int_{\partial\mathcal{B}} v_i \sigma_{ij} n_j \, dA \\ &= \int_{\mathcal{B}} \nabla\mathbf{v} : \boldsymbol{\sigma} \, dV + \int_{\mathcal{B}} \mathbf{v} \cdot \operatorname{div} \boldsymbol{\sigma} \, dV \end{aligned} \tag{2.55}$$

and

$$\int_{\partial\mathcal{B}} h \, dA = \int_{\partial\mathcal{B}} \mathbf{q} \cdot \mathbf{n} \, dA = \int_{\mathcal{B}} \operatorname{div} \mathbf{q} \, dV \tag{2.56}$$

Note that in the former, since $\boldsymbol{\sigma} = \boldsymbol{\sigma}^T$,

$$\nabla \mathbf{v} : \boldsymbol{\sigma} = \dot{\boldsymbol{\varepsilon}} : \boldsymbol{\sigma} = \boldsymbol{\sigma} : \dot{\boldsymbol{\varepsilon}} \tag{2.57}$$

and the definition of the strain tensor $\boldsymbol{\varepsilon} := \text{sym}(\nabla \mathbf{u}) = \frac{1}{2}(\nabla \mathbf{u} + \nabla^T \mathbf{u})$ implies $\text{sym}(\nabla \mathbf{v}) = \dot{\boldsymbol{\varepsilon}}$. Thus,

$$\nabla \mathbf{v} : \boldsymbol{\sigma} = \dot{\boldsymbol{\varepsilon}} : \boldsymbol{\sigma} = \boldsymbol{\sigma} : \dot{\boldsymbol{\varepsilon}} \tag{2.58}$$

Taking the time derivative and substituting the above transformations, it can be obtained

$$\begin{aligned} &\int_{\mathcal{B}} \frac{1}{2}\dot{\rho}|\mathbf{v}|^2 \, dV + \int_{\mathcal{B}} \rho \mathbf{v} \cdot \mathbf{a} \, dV + \int_{\mathcal{B}} \dot{\rho} e \, dV + \int_{\mathcal{B}} \rho \dot{e} \, dV \\ &= \int_{\mathcal{B}} (\rho \mathbf{b} \cdot \mathbf{v} + \boldsymbol{\sigma} : \dot{\boldsymbol{\varepsilon}} + \mathbf{v} \cdot \text{div}\, \boldsymbol{\sigma}) \, dV + \int_{\mathcal{B}} (\rho r - \text{div}\, \mathbf{q}) \, dV \end{aligned} \tag{2.59}$$

Putting the terms together on one side,

$$\int_{\mathcal{B}} \mathbf{v} \cdot (\rho \mathbf{a} - \text{div}\, \boldsymbol{\sigma} - \rho \mathbf{b}) \, dV + \int_{\mathcal{B}} (\rho \dot{e} - \boldsymbol{\sigma} : \dot{\boldsymbol{\varepsilon}} - \rho r + \text{div}\, \mathbf{q}) \, dV = 0 \tag{2.60}$$

where it is substituted the Balance of Linear Momentum (III.19) in the first term. Finally, applying the localization theorem

$$\lim_{\mathcal{B} \to dV} \int_{\mathcal{B}} (\rho \dot{e} - \boldsymbol{\sigma} : \dot{\boldsymbol{\varepsilon}} - \rho r + \text{div}\, \mathbf{q}) \, dV = 0 \tag{2.61}$$

It is obtained the local form of the energy balance, also known as the first law of thermodynamics:

$$\rho \dot{e} = \boldsymbol{\sigma} : \dot{\boldsymbol{\varepsilon}} + \rho r - \text{div}\, \mathbf{q} \tag{2.62}$$

which simply states that the rate of specific internal energy is equal to the sum of the internal stress power ($\boldsymbol{\sigma} : \dot{\boldsymbol{\varepsilon}}$) and the thermal power ($\rho r - \text{div}\, \mathbf{q}$).

2.7.5 Conservation of Entropy

$$\begin{aligned}\Gamma &:= \int_{\mathcal{B}} \rho\gamma \, dV = \frac{d}{dt} H - S \geq 0 \\ &= \frac{d}{dt} \int_{\mathcal{B}} \rho\eta \, dV - \int_{\mathcal{B}} \frac{\rho r}{\theta} \, dV + \int_{\partial\mathcal{B}} \frac{h}{\theta} \, dA \geq 0\end{aligned} \tag{2.63}$$

Transforming the surface integral into the volume integral:

$$\begin{aligned}\int_{\partial\mathcal{B}} \frac{h}{\theta} \, dA &= \int_{\partial\mathcal{B}} \frac{\mathbf{q} \cdot \mathbf{n}}{\theta} \, dA = \int_{\partial\mathcal{B}} \frac{q_i n_i}{\theta} \, dA \\ &= \int_{\mathcal{B}} \frac{1}{\theta} \operatorname{div} \mathbf{q} \, dV - \int_{\mathcal{B}} \frac{1}{\theta^2} \mathbf{q} \cdot \nabla\theta \, dV\end{aligned} \tag{2.64}$$

it is concluded at

$$\int_{\mathcal{B}} \rho\gamma \, dV = \int_{\mathcal{B}} \rho\dot{\eta} \, dV - \int_{\mathcal{B}} \frac{\rho r}{\theta} \, dV + \int_{\mathcal{B}} \frac{1}{\theta} \operatorname{div} \mathbf{q} \, dV - \int_{\mathcal{B}} \frac{1}{\theta^2} \mathbf{q} \cdot \nabla\theta \, dV \tag{2.65}$$

The localization

$$\lim_{\mathcal{B} \to dV} \int_{\mathcal{B}} \left(\rho\gamma - \rho\dot{\eta} + \frac{\rho r}{\theta} - \frac{1}{\theta} \operatorname{div} \mathbf{q} + \frac{1}{\theta^2} \mathbf{q} \cdot \nabla\theta \right) dV = 0 \tag{2.66}$$

leads to

$$\rho\gamma = \rho\dot{\eta} - \frac{1}{\theta}(\rho r - \operatorname{div} \mathbf{q}) - \frac{1}{\theta^2} \mathbf{q} \cdot \nabla\theta \geq 0 \tag{2.67}$$

From the first law, $\rho r - \operatorname{div} \mathbf{q} = \rho\dot{e} - \boldsymbol{\sigma} : \dot{\boldsymbol{\varepsilon}}$, so:

$$\rho\gamma = \rho\dot{\eta} - \frac{1}{\theta}(\rho\dot{e} - \boldsymbol{\sigma} : \dot{\boldsymbol{\varepsilon}}) - \frac{1}{\theta^2} \mathbf{q} \cdot \nabla\theta \geq 0 \tag{2.68}$$

2.8 Thermodynamic Dissipation, Clausius-Duhem Inequality, and Helmholtz Free Energy

2.8.1 Concept of Dissipation

The second law of thermodynamics, applied in the context of continuum mechanics, requires that the entropy production in a material body must always be non-negative. Starting from the local form of the entropy balance derived above,

$$\rho\gamma = \rho\dot{\eta} - \frac{1}{\theta}(\rho\dot{e} - \boldsymbol{\sigma} : \dot{\boldsymbol{\varepsilon}}) - \frac{1}{\theta^2}\mathbf{q} \cdot \nabla\theta \geq 0 \tag{2.69}$$

where γ is the rate of entropy production per unit mass, η is the entropy per unit mass, e is the internal energy per unit mass, θ is the absolute temperature, $\mathbf{q}$ is the heat flux vector, and r is the heat supply per unit mass.

This inequality enforces that all processes occurring within the material are thermodynamically admissible, i.e., **dissipation** (irreversible entropy production) is always non-negative. The term $-\frac{1}{\theta^2}\mathbf{q} \cdot \nabla\theta$ accounts for entropy production due to heat conduction, which, according to Fourier's law, is always positive for physically realistic processes.

2.8.2 Claussius-Duhem Inequality

The above relation is commonly known as the **Clausius-Duhem inequality**, and it provides a foundational constraint for all constitutive equations describing material behavior. By substituting the first law of thermodynamics,

$$\rho\dot{e} = \boldsymbol{\sigma} : \dot{\boldsymbol{\varepsilon}} + \rho r - \operatorname{div}\mathbf{q} \tag{2.70}$$

into the entropy inequality, and focusing on the isothermal case ($\nabla\theta = 0$, θ = constant), the inequality reduces to

$$\rho\gamma = \rho\dot{\eta} - \frac{1}{\theta}(\rho\dot{e} - \boldsymbol{\sigma} : \dot{\boldsymbol{\varepsilon}}) \geq 0 \tag{2.71}$$

2.8.3 Helmholtz Free Energy

A central concept in thermodynamics is the **Helmholtz free energy** per unit mass, defined by

$$\psi := e - \theta\eta \tag{2.72}$$

where ψ is the Helmholtz free energy. Taking the material time derivative (in the isothermal case) gives

$$\dot{\psi} = \dot{e} - \theta\dot{\eta} \tag{2.73}$$

Rearranging for the entropy rate, it is obtained

$$\theta\dot{\eta} = \dot{e} - \dot{\psi} \tag{2.74}$$

Substituting this result into the reduced Clausius-Duhem inequality leads to the following form:

$$\rho\gamma = \rho\dot{\eta} - \frac{1}{\theta}(\rho\dot{e} - \boldsymbol{\sigma} : \dot{\boldsymbol{\varepsilon}}) \tag{2.75}$$

$$= \frac{1}{\theta}\left(\boldsymbol{\sigma} : \dot{\boldsymbol{\varepsilon}} - \rho\dot{\psi}\right) \geq 0 \tag{2.76}$$

or, equivalently,

$$\boldsymbol{\sigma} : \dot{\boldsymbol{\varepsilon}} - \rho\dot{\psi} \geq 0 \tag{2.77}$$

This final expression represents the mechanical dissipation in isothermal processes. It establishes that the rate of mechanical work input, minus the rate of free energy storage, must be non-negative. This is a fundamental requirement for the formulation of thermodynamically consistent constitutive models.

CHAPTER 3

CRYSTAL PLASTICITY

3.1 Historical Evolution of Crystal Plasticity in Metallic Materials

3.1.1 Early Empirical Observations of Slip

The foundational understanding of plastic deformation in crystalline metals was established through meticulous empirical observations in the early 20th century. Researchers noted that when metallic single crystals were subjected to mechanical stress, distinct linear markings, known as slip traces, appeared on their polished surfaces. These traces were indicative of localized shear deformation occurring along specific crystallographic planes. Notably, the crystal lattice remained intact, suggesting that the deformation was due to the movement of dislocations rather than a breakdown of the crystal structure [7].

These early observations were pivotal in recognizing that plastic deformation in metals is governed by the motion of dislocations along particular slip systems. This insight laid the groundwork for the development of theoretical models that describe the anisotropic nature of plasticity in crystalline materials.

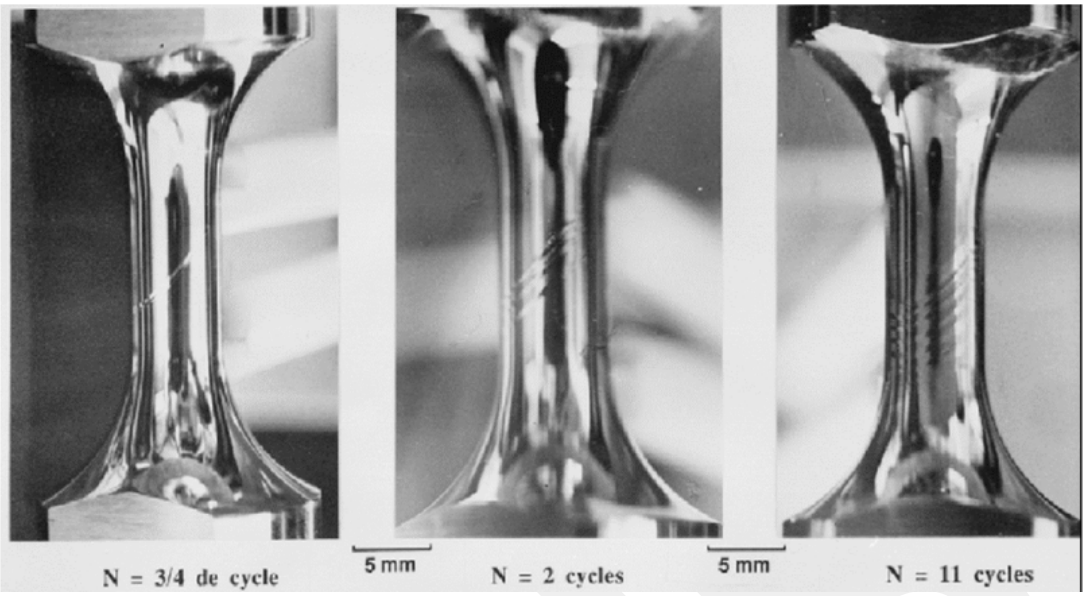


Figure 3.1: Slip lanes on surface of single crystal superalloy under fatigue loading[8].

Subsequent studies built upon these findings, leading to the formulation of models that quantitatively describe the behavior of crystals under stress. For instance, Taylor introduced a model in 1938 that conceptualized multiple slip systems contributing to the overall deformation of a crystal, providing a more comprehensive understanding of plasticity in single crystals [9]. Modern interpretations of this framework, particularly with respect to multislip interactions and rate-dependent effects, are presented in more recent works [10].

These empirical insights and theoretical advancements collectively contributed to the evolution of crystal plasticity theory, which has become instrumental in predicting and analyzing the mechanical behavior of crystalline materials, particularly in applications involving single crystal superalloys.

3.1.2 Multi Slip Systems

The foundational understanding of plastic deformation in crystalline metals was significantly advanced by G. I. Taylor's seminal work in 1938. Taylor proposed that the plastic deformation of polycrystalline metals could be understood by considering the behavior of individual grains, each undergoing deformation through multiple slip systems to accommodate the imposed macroscopic strain [9].

In his model, Taylor assumed that each grain in a polycrystalline aggregate deforms uniformly, experiencing the same strain as the overall material. This assumption led to the concept of multiple slip systems being activated within each grain to achieve compatibility with the surrounding matrix. The model provided a framework for predicting the onset of yielding and the subsequent plastic flow in metals, particularly those with face-centered cubic (FCC) crystal structures.

Taylor's model introduced the idea that five independent slip systems are necessary to accommodate arbitrary plastic deformation in three dimensions. This concept was crucial in explaining the ductility of metals and the ability of polycrystalline aggregates to undergo large plastic strains without failure. The model also laid the groundwork for the development of more sophisticated theories of crystal plasticity that account for anisotropic behavior and the influence of grain interactions.

Subsequent refinements to Taylor's model have addressed its limitations, such as the assumption of uniform strain across all grains. For instance, the inclusion of grain interaction effects and the consideration of stress heterogeneity have led to more accurate predictions of material behavior. These advancements have been instrumental in the development of crystal plasticity finite element methods (CPFEM), which allow for the simulation of complex deformation processes in polycrystalline materials [10].

3.1.3 Schmid Law and the Concept of Resolved Shear Stress

The onset of plastic deformation in crystalline materials is governed by the activation of specific slip systems, which are combinations of crystallographic planes and directions along which dislocation motion occurs. A fundamental criterion for predicting the initiation of slip is provided by Schmid's Law, formulated by Erich Schmid and Walter Boas in 1935 [11]. This law quantifies the resolved shear stress (τ) acting on a slip system as a function of the applied normal stress (σ) and the orientation of the slip system relative to the loading direction:

$$\tau = \sigma \cos\phi \cos\lambda \tag{3.1}$$

Here, ϕ is the angle between the slip plane normal and the applied stress direction, and λ is the angle between the slip direction and the applied stress direction. The product $\cos\phi\cos\lambda$ is known as the Schmid factor (m), which represents the geometric component influencing the effectiveness of the applied stress in producing shear on the slip system.

According to Schmid's Law, slip initiates when the resolved shear stress reaches a critical value, known as the critical resolved shear stress (CRSS, τ_{crit}):

$$\tau \geq \tau_{\text{crit}} \tag{3.2}$$

This criterion implies that for a given material and temperature, the CRSS is a material constant, and the activation of slip depends on the orientation of the crystal relative to the applied stress. The maximum Schmid factor occurs when both ϕ and λ are 45°, resulting in $m = 0.5$. This orientation yields the highest resolved shear stress for a given applied stress, making it the most favorable condition for slip initiation.

Schmid's Law is particularly applicable to face-centered cubic (FCC) metals, where the slip systems are well-defined and the CRSS is relatively low and isotropic. However, in body-centered cubic (BCC) metals, deviations from Schmid's Law have been observed due to the influence of non-glide stress components and the complex core structures of screw dislocations. These factors can lead to phenomena such as tension-compression asymmetry and orientation-dependent CRSS, necessitating more advanced models to accurately predict plastic behavior in such materials [12, 13, 14].

Furthermore, the CRSS plays a significant role in the fatigue performance of materials. Studies have shown that materials with higher CRSS values tend to exhibit better fatigue resistance, as the higher stress required to initiate slip delays the onset of plastic deformation under cyclic loading [15].

Understanding the principles of Schmid's Law is essential for analyzing the mechanical behavior of single crystals and for developing crystal plasticity models that can predict the anisotropic response of materials under various loading conditions.

3.1.4 Development of Crystal Plasticity as a Continuum Framework

The evolution of crystal plasticity into a continuum framework has been pivotal in advancing our understanding of the mechanical behavior of crystalline materials. Early models, such as those proposed by Taylor and Elam in 1923[16], laid the groundwork by considering the collective behavior of slip systems within polycrystalline aggregates. However, these models were limited in capturing the anisotropic and heterogeneous nature of crystal deformation.

The advent of continuum mechanics provided a robust platform to model the complex interactions within crystalline materials. By integrating the principles of continuum mechanics with crystallographic slip, researchers developed constitutive models that could account for the anisotropic plastic behavior observed in single crystals. These models introduced internal variables representing the state of the crystal, such as dislocation densities and slip system activities, enabling a more accurate depiction of the material's response under various loading conditions.

A significant advancement in this field was the development of the Crystal Plasticity Finite Element Method (CPFEM). CPFEM allows for the simulation of polycrystalline materials by discretizing the material into finite elements, each representing a single crystal orientation. This method captures the heterogeneity of deformation and the interactions between grains, providing insights into phenomena such as texture evolution, strain localization, and anisotropic hardening [17].

Moreover, the integration of multiscale modeling approaches has further enhanced the predictive capabilities of crystal plasticity frameworks. By bridging atomistic simulations with continuum models, researchers can capture the influence of microscale mechanisms, such as dislocation nucleation and motion, on the macroscopic behavior of materials. This holistic approach enables the design of materials with tailored properties by understanding and manipulating their underlying microstructural features [18].

The continuous refinement of crystal plasticity models, coupled with advancements in computational power, has solidified their role as indispensable tools in materials science and engineering. These models not only facilitate the prediction of material behavior under various loading conditions but also aid in the development of new materials with enhanced performance characteristics.

3.1.5 Relevance to Single Crystal Superalloys

The development of crystal plasticity frameworks has been instrumental in advancing our understanding of the mechanical behavior of single crystal superalloys, particularly nickel-based variants, which are extensively utilized in high-temperature applications such as turbine blades in aerospace engines. These materials exhibit exceptional creep resistance and mechanical strength at elevated temperatures, attributes that are intrinsically linked to their unique microstructural features and deformation mechanisms.

Single crystal superalloys are characterized by a two-phase microstructure comprising a γ matrix and coherent γ' precipitates. The γ' phase, typically ordered $L1_2$ Ni_3Al, imparts significant strength by impeding dislocation motion through coherency strains and order hardening mechanisms. The absence of grain boundaries in single crystals eliminates grain boundary sliding and associated creep mechanisms, thereby enhancing high-temperature performance.

Crystal plasticity models have been pivotal in capturing the anisotropic and orientation-dependent deformation behavior of these materials. For instance, CPFEM has been employed to simulate the creep behavior of single crystal superalloys, accounting for the evolution of dislocation structures and the influence of crystallographic orientation on mechanical response [19]. These models incorporate the effects of slip system activity, lattice rotations, and the interaction between dislocations and γ' precipitates, providing insights into the mechanisms governing creep deformation.

Moreover, advanced modeling approaches have integrated phase-field methods with crystal plasticity to simulate the co-evolution of microstructure and mechanical behavior. Such coupled models enable the prediction of phenomena like rafting, where the γ' precipitates align perpendicularly to the applied stress direction during high-temperature creep, affecting the material's strength and deformation characteristics [20].

The relevance of crystal plasticity frameworks extends to the design and optimization of single crystal superalloys. By simulating various loading conditions and microstructural configurations, these models assist in tailoring alloy compositions and heat treatment processes to achieve desired mechanical properties. Furthermore, they facilitate the assessment of service life and performance of components under operational conditions, contributing to the reliability and efficiency of high-temperature systems.

3.2 Crystallographic Deformation and Slip System Activation

3.2.1 Description of Active Slip Systems in FCC Crystals

Face-centered cubic (FCC) crystals, such as those found in nickel-based superalloys, exhibit high ductility due to the presence of multiple slip systems. The primary slip systems in FCC structures are the {111} planes and <110> directions, resulting in 12 distinct slip systems. This abundance of slip systems facilitates plastic deformation under various loading conditions, contributing to the material's formability and toughness.

The activation of these slip systems is governed by the resolved shear stress acting on the slip plane in the slip direction, as described by Schmid's law. When the resolved shear stress reaches a critical value, known as the critical resolved shear stress (CRSS), dislocation motion initiates along the most favorably oriented slip system. The CRSS is influenced by factors such as temperature, strain rate, and the presence of obstacles like precipitates or solute atoms [21].

3.2.2 Role of γ and γ' Phases in Accommodating Deformation

Nickel-based superalloys are characterized by a two-phase microstructure comprising a disordered γ matrix and ordered γ' precipitates (Ni_3Al). The γ' phase is coherent with the γ matrix and serves as the primary strengthening mechanism by impeding dislocation motion. During deformation, dislocations can shear through the γ' precipitates or bypass them via Orowan looping, depending on factors such as precipitate size, spacing, and temperature.

At lower temperatures, dislocation shearing of γ' precipitates is more prevalent, while at higher temperatures, Orowan bypass becomes dominant due to increased dislocation mobility. The interaction between dislocations and γ' precipitates significantly influences the creep resistance and overall mechanical properties of the superalloy [22].

3.2.3 Partial Dislocation Motion, Stacking Faults, and Glide Barriers

In FCC crystals with low stacking fault energy (SFE), perfect dislocations tend to dissociate into partial dislocations separated by stacking faults. This dissociation reduces the energy of the dislocation but introduces a barrier to cross-slip, thereby affecting the material's work hardening behavior. The width of the stacking fault is inversely related to the SFE; lower SFE leads to wider stacking faults and greater separation between partials.

The presence of stacking faults and partial dislocations can impede dislocation motion, acting as barriers to glide and influencing the activation of additional slip systems. These mechanisms play a crucial role in the deformation behavior of nickel-based superalloys, particularly under conditions where cross-slip is limited [23].

3.2.4 Orientation-Dependent Plasticity and Anisotropy

The mechanical response of single crystal superalloys is highly anisotropic due to the crystallographic orientation of the specimen relative to the loading direction. For instance, specimens oriented along the [001] direction typically exhibit superior creep resistance and tensile strength compared to other orientations. This anisotropy arises from the directional dependence of slip system activation and the interaction between dislocations and the γ/γ' microstructure.

Understanding the orientation-dependent plasticity is essential for optimizing the performance of components made from single crystal superalloys. By aligning the crystallographic orientation to exploit favorable slip system activation, engineers can enhance the mechanical properties and service life of critical components, such as turbine blades in jet engines [24].

3.3 Thermomechanics of Elastoviscoplastic Single Crystals

The constitutive modeling of single crystal behavior under high-temperature loading conditions requires a thermodynamically consistent framework capable of accounting for elastic, plastic, and viscoplastic deformation mechanisms. To this end, the thermomechanical formulation is constructed based on the principles of continuum mechanics and the second law of thermodynamics, following the Coleman–Noll procedure [25].

3.3.1 Balance Laws

To construct a thermodynamically consistent constitutive model, it is essential to begin with the fundamental balance laws of continuum mechanics. These laws govern the conservation of mass, linear and angular momentum, energy, and entropy, and provide the framework for deriving the restrictions that any admissible constitutive equation must satisfy. The formulations below are presented in their local differential forms under the continuum assumption.

1. **Mass Conservation**

   The conservation of mass in the reference configuration is expressed as:

   $$\dot{\rho}_0 = 0, \tag{3.3}$$

   where ρ_0 denotes the reference mass density. In the absence of phase transformations or mass sources/sinks, the material is assumed incompressible in the reference frame.

2. **Balance of Linear and Angular Momentum**

   The balance of linear momentum ensures that the rate of change of linear momentum equals the sum of internal and external forces. Neglecting inertial terms and assuming quasi-static conditions, the equation in the current configuration is:

   $$\nabla \cdot \boldsymbol{\sigma} - \rho \boldsymbol{b} = \mathbf{0}, \tag{3.4}$$

   where $\boldsymbol{\sigma}$ is the Cauchy stress tensor and $\boldsymbol{b}$ is the body force per unit mass.

   The balance of angular momentum imposes symmetry on the stress tensor:

   $$\boldsymbol{\sigma} = \boldsymbol{\sigma}^T \tag{3.5}$$

   This condition ensures that no internal moment couples exist, which is valid for classical continua with no couple stresses or intrinsic rotations. In the absence of material anisotropy at the continuum scale, this symmetry naturally follows from torque balance on infinitesimal elements.

3. **Energy Balance (1$^{\text{st}}$ Law of Thermodynamics)**

   The first law of thermodynamics enforces conservation of energy. It states that the rate of change of internal energy within a body is equal to the sum of mechanical work done and the thermal energy added. In the absence of chemical reactions and radiation, the local differential form is:

   $$\rho \dot{e} = \boldsymbol{\sigma} : \dot{\boldsymbol{\varepsilon}} + \rho r - \nabla \cdot \mathbf{q}, \tag{3.6}$$

where e is the specific internal energy, r is the heat source per unit mass, and $\mathbf{q}$ is the heat flux vector. The first term on the right-hand side, $\boldsymbol{\sigma} : \dot{\boldsymbol{\varepsilon}}$, represents the power expended by internal stresses through deformation. The final term captures spatial heat flux divergence, describing energy transport by conduction.

This equation ensures that all internal energy changes are accounted for by external inputs either mechanical or thermal and serves as a foundation for connecting mechanical dissipation and heat generation in later thermomechanical formulations.

4. **Entropy Balance (2nd Law of Thermodynamics)**

   The second law of thermodynamics introduces irreversibility into the system. It demands that entropy must not decrease and strictly increases in the presence of dissipative processes such as plastic deformation or heat conduction.

   The local form of the entropy inequality can be written as:

$$\rho\gamma = \rho\dot{\eta} - \frac{1}{\theta}(\rho\dot{e} - \boldsymbol{\sigma} : \dot{\boldsymbol{\varepsilon}}) - \frac{1}{\theta^2}\mathbf{q} \cdot \nabla\theta \geq 0, \tag{3.7}$$

   where η is the specific entropy and θ is the absolute temperature. The first term on the right corresponds to the entropy rate, while the remaining terms account for entropy changes induced by internal energy variations and heat conduction. The scalar γ quantifies the net entropy production rate and must remain non-negative.

   This inequality plays a central role in deriving admissible constitutive equations. It not only constrains how materials respond to mechanical and thermal loads, but also provides a pathway to extract dissipation mechanisms and internal variable evolution laws in a thermodynamically consistent manner.

5. **Claussius-Duhem Inequality, Dissipation and Helmholtz Free Energy**

   The second law of thermodynamics requires that the total entropy of a system does not decrease. By combining the internal energy balance with the entropy inequality, the Clausius–Duhem inequality in local form is obtained as:

$$-\rho(\dot{e} - \theta\dot{\eta}) + \boldsymbol{\sigma} : \dot{\boldsymbol{\varepsilon}} - \frac{\mathbf{q}}{\theta} \cdot \nabla\theta \geq 0 \tag{3.8}$$

   Introducing the Helmholtz free energy as $\psi = e - \theta\eta$, the inequality becomes:

$$-\rho(\dot{\psi} + \eta\dot{\theta}) + \boldsymbol{\sigma} : \dot{\boldsymbol{\varepsilon}} - \frac{\mathbf{q}}{\theta} \cdot \nabla\theta \geq 0 \tag{3.9}$$

This can be split into two contributions: local mechanical dissipation and conductive dissipation:

$$\rho D_{\text{loc}} = -\rho(\dot{\psi} + \eta\dot{\theta}) + \boldsymbol{\sigma} : \dot{\boldsymbol{\varepsilon}} \geq 0 \tag{3.10}$$

$$\rho D_{\text{cond}} = -\frac{\mathbf{q}}{\theta} \cdot \nabla\theta \geq 0 \tag{3.11}$$

Under isothermal conditions, i.e., $\dot{\theta} = 0$, the inequality reduces to:

$$\rho D = \boldsymbol{\sigma} : \dot{\boldsymbol{\varepsilon}} - \rho\dot{\psi} \geq 0 \tag{3.12}$$

which serves as the thermodynamic constraint that any admissible constitutive model must fulfill to ensure positive dissipation.

These balance laws establish the governing framework for subsequent thermomechanical modeling. In the following sections, they are used to derive state equations, internal variable evolution, and flow rules consistent with crystal plasticity theory.

3.3.2 Specialization of Free Energy Function with Coleman's Exploitation

3.3.2.1 Coleman's Exploitation

The thermodynamic restrictions derived in the local dissipation inequality can be systematically utilized to derive thermodynamically admissible constitutive equations. This is accomplished using Coleman's exploitation method, in which the free energy function is assumed to depend on observable and internal state variables relevant to the material's response.

A general form of the Helmholtz free energy per unit reference mass is assumed as:

$$\psi = \hat{\psi}(x, \theta, \boldsymbol{\varepsilon}, \boldsymbol{\varepsilon}^p, \boldsymbol{\alpha}, \boldsymbol{g}), \tag{3.13}$$

where x is the spatial position, θ is the temperature, $\boldsymbol{\varepsilon}$ is the total strain tensor, $\boldsymbol{\varepsilon}^p$ is the plastic strain tensor, $\boldsymbol{\alpha}$ is a set of internal variables (e.g., hardening variables), and $\boldsymbol{g} = \nabla\theta$ is the temperature gradient.

Accordingly, the thermodynamic quantities are defined as constitutive functions of the same state variables:

$$\boldsymbol{\sigma} = \hat{\boldsymbol{\sigma}}(x, \theta, \boldsymbol{\varepsilon}, \boldsymbol{\varepsilon}^p, \boldsymbol{\alpha}, \boldsymbol{g}), \tag{3.14}$$

$$\boldsymbol{\beta} = \hat{\boldsymbol{\beta}}(x, \theta, \boldsymbol{\varepsilon}, \boldsymbol{\varepsilon}^p, \boldsymbol{\alpha}, \boldsymbol{g}), \tag{3.15}$$

$$\eta = \hat{\eta}(x, \theta, \boldsymbol{\varepsilon}, \boldsymbol{\varepsilon}^p, \boldsymbol{\alpha}, \boldsymbol{g}), \tag{3.16}$$

$$\mathbf{q} = \hat{\mathbf{q}}(x, \theta, \boldsymbol{\varepsilon}, \boldsymbol{\varepsilon}^p, \boldsymbol{\alpha}, \boldsymbol{g}). \tag{3.17}$$

Here, $\boldsymbol{\beta}$ and X denote thermodynamic forces conjugate to $\boldsymbol{\varepsilon}^p$ and $\boldsymbol{\alpha}$, respectively.

The material time derivative of the free energy function is expressed via the chain rule as:

$$\dot{\psi} = \frac{\partial \hat{\psi}}{\partial \boldsymbol{\varepsilon}} : \dot{\boldsymbol{\varepsilon}} + \frac{\partial \hat{\psi}}{\partial \boldsymbol{\varepsilon}^p} : \dot{\boldsymbol{\varepsilon}}^p + \frac{\partial \hat{\psi}}{\partial \theta}\dot{\theta} + \frac{\partial \hat{\psi}}{\partial \boldsymbol{g}} \cdot \dot{\boldsymbol{g}}. \tag{3.18}$$

Substituting this expression into the local dissipation inequality yields:

$$\begin{aligned} \rho D_{\text{loc}} = \left[\boldsymbol{\sigma} - \rho\frac{\partial \hat{\psi}}{\partial \boldsymbol{\varepsilon}}\right] : \dot{\boldsymbol{\varepsilon}} - \rho\frac{\partial \hat{\psi}}{\partial \boldsymbol{\varepsilon}^p} : \dot{\boldsymbol{\varepsilon}}^p - \rho\left(\eta + \frac{\partial \hat{\psi}}{\partial \theta}\right)\dot{\theta} \\ - \rho\frac{\partial \hat{\psi}}{\partial \boldsymbol{g}} \cdot \dot{\boldsymbol{g}} \geq 0 \end{aligned} \tag{3.19}$$

Since this inequality must hold for all admissible processes, including arbitrary rates $\dot{\boldsymbol{\varepsilon}}, \dot{\theta}, \dot{\boldsymbol{g}}$, the following constitutive constraints must be satisfied:

$$\boldsymbol{\sigma} = \rho\frac{\partial \hat{\psi}}{\partial \boldsymbol{\varepsilon}}, \qquad \eta = -\frac{\partial \hat{\psi}}{\partial \theta}, \qquad \frac{\partial \hat{\psi}}{\partial \boldsymbol{g}} = 0 \tag{3.20}$$

These are the standard thermodynamic consistency conditions for thermoelasticity, which ensure that purely elastic responses are non-dissipative and reversible.

Consequently, the dissipation inequality reduces to:

$$\boldsymbol{\beta} : \dot{\boldsymbol{\varepsilon}}^p \geq 0 \tag{3.21}$$

This reduced form identifies the contributions to mechanical dissipation due to inelastic strain evolution and internal variable dynamics. It forms the foundation upon which rate-independent or rate-dependent plastic flow and hardening laws can be developed in the next stages of constitutive modeling.

3.3.2.2 Free Energy Function and State Laws

To characterize the thermodynamic behavior of single crystal plasticity, a specific form of the Helmholtz free energy density is introduced, incorporating elastic deformation and isotropic hardening effects through internal variables. The proposed free energy function takes the following form [26]:

$$\psi(\boldsymbol{\varepsilon}^e, \varrho^\alpha) = \frac{1}{2}\boldsymbol{\varepsilon}^e : \mathbb{C} : \boldsymbol{\varepsilon}^e + r_0 \sum_{\alpha=1}^{N} \varrho^\alpha + \frac{q}{2} \sum_{r,\alpha=1}^{N} h^{r\alpha} \varrho^r \varrho^\alpha \tag{3.22}$$

Here, $\boldsymbol{\varepsilon}^e$ is the elastic strain tensor, $\mathbb{C}$ is the fourth-order elasticity tensor for cubic symmetry, r_0 denotes the initial slip resistance, and q is a hardening coefficient. The scalar variable ϱ^α quantifies the isotropic hardening contribution from each slip system α, and $h^{r\alpha}$ is an interaction matrix that accounts for self and latent hardening between slip systems r and α.

From this energy potential, the thermodynamic state equations are derived by differentiation with respect to the appropriate variables:

$$\boldsymbol{\sigma} = \rho \frac{\partial \psi}{\partial \boldsymbol{\varepsilon}^e} = \mathbb{C} : \boldsymbol{\varepsilon}^e, \tag{3.23}$$

$$r^\alpha = \rho \frac{\partial \psi}{\partial \varrho^\alpha} = r_0 + q \sum_{r=1}^{N} h^{\alpha r} \varrho^r, \tag{3.24}$$

where $\boldsymbol{\sigma}$ is the Cauchy stress tensor and r^α is the current slip resistance on slip system α, which evolves through the accumulation of plastic activity represented by ϱ^α.

Note that the elastic strain is defined using the symmetric part of the displacement gradient as $\boldsymbol{\varepsilon} = \mathrm{sym}[\nabla \boldsymbol{u}]$.

3.3.3 Kinematics of Crystal Plasticity

Consider a single crystal body $\mathcal{B}$ undergoing large deformations. The motion is described by the deformation map $\boldsymbol{x} : \mathcal{B}_0 \rightarrow \mathbb{R}^3$, where $\mathcal{B}_0$ is the reference configuration. The deformation gradient, velocity and velocity gradient defined as

$$\mathbf{F} = \nabla\chi, \qquad \mathbf{v} = \dot{\chi}, \qquad \mathbf{L} = grad(\mathbf{v}) = \dot{\mathbf{F}}\mathbf{F}^{-1}. \tag{3.25}$$

The velocity gradient $\mathbf{L} = \dot{\mathbf{F}}\mathbf{F}^{-1}$ is additively decomposed into elastic and plastic parts using the multiplicative decomposition of the deformation gradient:

$$\mathbf{F} = \mathbf{F}^e\mathbf{F}^p, \tag{3.26}$$

where $\mathbf{F}^p$ represents the plastic deformation due to crystallographic slip and $\mathbf{F}^e$ corresponds to the elastic distortion. The right polar decomposition of $\mathbf{F}^e$ is

$$\mathbf{F}^e = \mathbf{R}^e\mathbf{U}^e \tag{3.27}$$

where $\mathbf{R}^e$ is a rotation tensor and $\mathbf{U}^e$ is the right stretch tensor. The right Cauchy-Green tensor and the Hencky's strain is then

$$\mathbf{C}^e = (\mathbf{U}^e)^2 = \mathbf{F}^{eT}\mathbf{F}^e, \qquad \mathbf{E}^e = ln(\mathbf{U}^e) \tag{3.28}$$

This strain measure is symmetric and work-conjugate to the Second Piola–Kirchhoff stress tensor defined as follows:

$$\mathbf{S} = \mathbb{C} : \boldsymbol{E}^e \tag{3.29}$$

where $\mathbb{C}$ is the fourth order elasticity moduli and characterizes the cubic elastic behavior of the material. For cubic crystals, $\mathbb{C}$ has three independent components: C_{11}, C_{12}, and C_{44}. Hence, the stiffness matrix in Voigt notation is given by:

$$\mathbb{C} = \begin{bmatrix} C_{11} & C_{12} & C_{12} & 0 & 0 & 0 \\ C_{12} & C_{11} & C_{12} & 0 & 0 & 0 \\ C_{12} & C_{12} & C_{11} & 0 & 0 & 0 \\ 0 & 0 & 0 & C_{44} & 0 & 0 \\ 0 & 0 & 0 & 0 & C_{44} & 0 \\ 0 & 0 & 0 & 0 & 0 & C_{44} \end{bmatrix}$$

where

$$C_{11} = \frac{1}{3}(3K + 4\mu), \quad C_{12} = \frac{1}{3}(3K - 2\mu), \quad C_{44} = \mu + \mu' \tag{3.30}$$

where K is bulk modulus, μ is shear modulus and μ' is the effective shear modulus described in specific crystallographic directions [27].

Since the plastic deformation can be considered as a result of activation of slip systems with α being the number of slip system and N is the total number of slip systems, the plastic stretching tensor is written in the following:

$$\mathbf{D}^p = \sum_{\alpha=1}^{N} \dot{\gamma}^\alpha \mathbf{m}^\alpha \otimes \mathbf{n}^\alpha \tag{3.31}$$

where $\mathbf{m}^\alpha$ is the flow direction and $\mathbf{n}^\alpha$ is the normal to the slip plane and γ is the plastic slip where it is defined as:

$$\dot{\gamma}^\alpha = \langle \frac{|\tau^\alpha| - r^\alpha}{K} \rangle^n sign(\tau^\alpha) \tag{3.32}$$

where r^α is the plastic slip threshold, K and n are the viscosity parameters. The plastic threshold with isotropic hardening for each slip system is given as:

$$r^\alpha = r_0 + q \sum_{\alpha=1}^{N} h^{\alpha r} \rho^\alpha \tag{3.33}$$

where r_0 stands for yield threshold for each slip system, q is a material constant represents the maximum value of hardening, $h^{\alpha r}$ is the interaction matrix that governs the self and latent hardening of the material caused by the interactions between the N number of slip systems and usually is taken as identity matrix for single crystal Ni-based superalloys since they do not show pro-dominant latent hardening [27]. The least term ρ^α is defined as non-linear isotropic hardening:

$$\rho^\alpha = (1 - exp(-b|\gamma^\alpha|) \tag{3.34}$$

where b is a parameter which controls the rate of saturation. The resolved shear stress in eqn[] is then:

$$\tau^\alpha = \mathbf{S} : (\mathbf{m}^\alpha \otimes \mathbf{n}^\alpha) \tag{3.35}$$

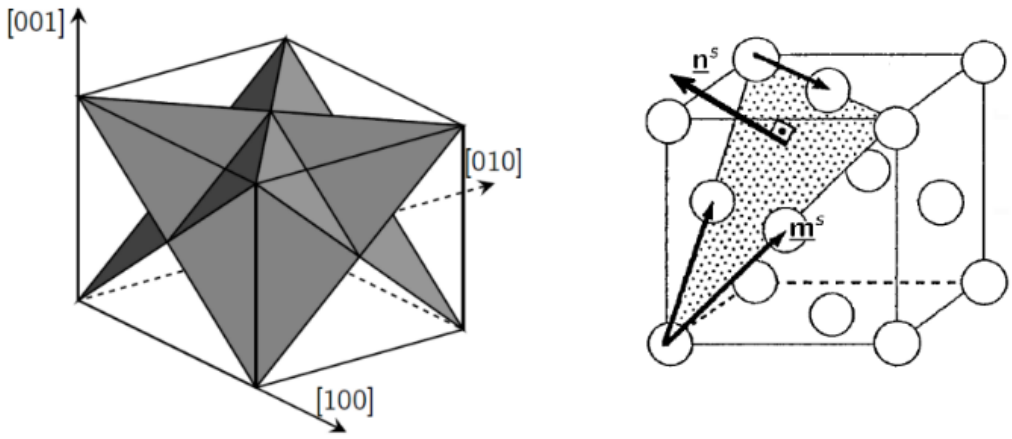


Figure 3.2: Octahedral slip systems and slip normals $\mathbf{n}^\alpha$ and slip directions $\mathbf{m}^\alpha$ [26].

3.3.4 Dissipation and Flow Relations

The remaining terms in the dissipation inequality define the inelastic contribution, which stems solely from crystallographic slip:

$$\mathcal{D} = \sum_{\alpha=1}^{N} \tau^\alpha \dot{\gamma}^\alpha - r^\alpha \dot{r}^\alpha \geq 0, \tag{3.36}$$

where τ^α is the resolved shear stress and $\dot{\gamma}^\alpha$ is the slip rate on slip system α, while r^α denotes the slip resistance (or yield threshold), which evolves due to isotropic hardening. This structure identifies the energetic conjugacy between slip and resistance and forms the basis of constitutive modeling in the absence of kinematic hardening.

To maintain thermodynamic admissibility, the plastic flow rule must be derived from a viscoplastic potential or yield function. For rate-independent behavior, the following Kuhn–Tucker conditions are imposed:

$$f^\alpha(\tau^\alpha, r^\alpha) \leq 0, \quad \dot{\gamma}^\alpha \geq 0, \quad \dot{\gamma}^\alpha f^\alpha = 0. \tag{3.37}$$

For rate-dependent flow, a viscoplastic overstress-type law is adopted:

$$\dot{\gamma}^\alpha = \dot{\gamma}_0 \left\langle \frac{|\tau^\alpha| - r^\alpha}{K} \right\rangle^n \operatorname{sign}(\tau^\alpha), \tag{3.38}$$

where $\dot{\gamma}_0$ is the reference slip rate, K is a drag stress, n is the rate sensitivity exponent, and $\langle \cdot \rangle$ denotes the Macaulay bracket. This formulation guarantees that dissipation remains non-negative for all admissible thermomechanical paths.

CHAPTER 4

HYDROGEN EMBRITTLEMENT IN METALS

4.1 Historical Background and Engineering Relevance

Hydrogen embrittlement (HE) has been recognized as a critical metallurgical problem for nearly 150 years. Its origin can be traced back to the late 19th century, during the Second Industrial Revolution, when the widespread use of acid treatments in the wire-drawing industry led to unexpected material failures. In 1875, W.H. Johnson conducted experiments on iron wires cleaned in sulfuric acid and observed that the wires became brittle and, upon fracture, released gas bubbles—later inferred to be hydrogen [28]. Johnson proposed that hydrogen produced at the iron surface during acid exposure was absorbed into the metal and later released at the fracture site, initiating what is known as hydrogen embrittlement.

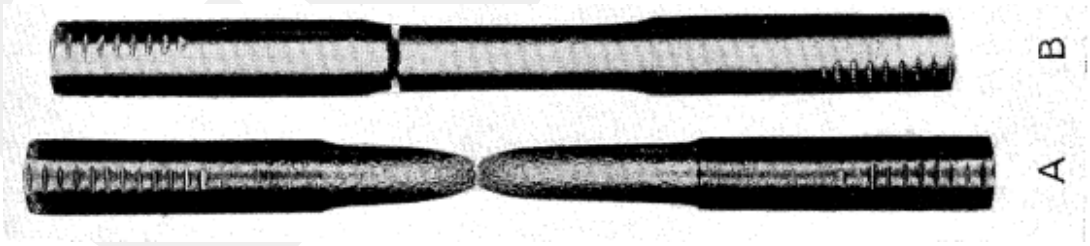


Figure 4.1: A, finely crystalline iron under normal conditions. B, same specimen during pickling [29].

Johnson's work was subsequently validated and expanded upon by other researchers, including Hughes in 1880, who confirmed that hydrogen exposure rendered iron and steel brittle. In 1926, L.B. Pfeil published a seminal study showing how the presence of occluded hydrogen reduced the tensile strength of iron [29]. Pfeil hypothesized that atomic hydrogen weakened metallic cohesion, offering an early mechanistic interpretation of the embrittlement process.

The mid-20th century brought theoretical advancements. In 1949, Darken and Smith developed a framework to describe hydrogen diffusion in steel, distinguishing between stationary and non-stationary regimes and highlighting the importance of microstructural features such as dislocations and grain boundaries [30]. In 1970, R.A. Oriani formalized the theory of hydrogen trapping, introducing a thermodynamic model that accounts for the equilibrium between mobile and trapped hydrogen sites[31]. Oriani's approach remains a cornerstone of modern HE modeling and widely used in HE simulation frameworks today.

By the 1980s, researchers like Hirth and Kumnick focused on the mechanical implications of hydrogen trapping in deformed iron. Kumnick and Johnson's time-lag permeation experiments established a high binding energy for deep traps (60 kJ/mol), showing that plastic deformation and dislocation structures act as major hydrogen sinks [32]. Hirth (1980) further emphasized that no single mechanism could fully describe HE, calling for multifactorial models involving trapping, decohesion, and dislocation interactions [33].

Contemporary reviews [34, 35], categorize HE mechanisms into several overlapping modes: hydrogen-enhanced decohesion (HEDE), hydrogen-enhanced localized plasticity (HELP), adsorption-induced dislocation emission (AIDE), and hydride fracture. Lynch also highlighted that many HE manifestations involve hydrogen-assisted cracking (HAC) without visible warning, especially in high-strength steels and superalloys.

In recent decades, experimental capabilities have significantly improved. High resolution transmission electron microscopy (TEM), atom probe tomography (APT), and thermal desorption spectroscopy (TDS) have enabled nanoscale observation of hydrogen interactions with lattice defects. Yet, as highlighted by Tunes et al. in their recent review [36], even the most advanced techniques still face challenges in detecting hydrogen directly at the nanoatomic scale or under in situ loading conditions. This experimental limitation hampers full validation of competing HE mechanisms such as hydrogen-enhanced localized plasticity (HELP), hydrogen-enhanced decohesion (HEDE), and adsorption-induced dislocation emission (AIDE) [34].

4.1.1 Engineering Relevance

Hydrogen embrittlement continues to pose a serious threat to the safety and longevity of structural components in energy, aerospace, nuclear, and automotive sectors. Components subjected to hydrogen-rich environments such as turbine blades, reactor containment vessels, and hydrogen transport pipelines, can experience catastrophic failure under otherwise safe loading conditions.

The susceptibility of materials varies widely. High-strength martensitic steels (>1400 MPa) can suffer HE from hydrogen concentrations as low as 1 ppm [35], while austenitic steels and aluminum alloys generally exhibit greater resistance unless subjected to extreme conditions. Nickel-based superalloys, often used in turbine engines, may suffer from hydrogen-assisted decohesion if exposed to gaseous hydrogen at high pressures and temperatures.

Detection and prevention of HE remain challenging. Hydrogen's small size and high mobility allow it to diffuse rapidly through metals and accumulate at critical microstructural features such as grain boundaries, dislocations, and phase interfaces. This makes early-stage embrittlement nearly impossible to detect through conventional non-destructive testing (NDT) techniques.

With the global emphasis on transitioning to hydrogen energy systems, understanding HE is more relevant than ever. The projected increase in hydrogen storage, transportation, and usage infrastructure calls for predictive modeling and robust materials screening to mitigate HE risks.

In summary, hydrogen embrittlement is both a historical and contemporary challenge. Understanding its origins and evolution is essential for the development of reliable models and experimental methods, and for ensuring the safety and longevity of critical engineering systems.

4.1.2 Mechanisms of Hydrogen Embrittlement

Hydrogen embrittlement (HE) arises from several synergistic mechanisms that alter the mechanical integrity of metals exposed to hydrogen-rich environments. Over the past decades, significant progress has been made in distinguishing and characterizing these mechanisms. However, due to their overlapping consequences and context-dependent activation, they are still actively debated and researched [34, 37, 38]. The primary mechanisms include Hydrogen-Enhanced Decohesion (HEDE), Hydrogen-Enhanced Localized Plasticity (HELP), Adsorption-Induced Dislocation Emission (AIDE), and hydride formation. Each is introduced below with a focus on physical interpretation rather than modeling implications.

4.1.2.1 Hydrogen-Enhanced Decohesion (HEDE)

The HEDE mechanism is based on the reduction of atomic cohesive strength in the presence of hydrogen, especially at internal interfaces such as grain boundaries, phase boundaries, and cleavage planes. Originally articulated in the early 20th century, and formalized in theoretical models by Oriani, Troiano, and others, HEDE posits that hydrogen segregates to regions of high triaxial stress, where it reduces the energy required for atomic separation.

Atomistic simulations have provided compelling support for this model, showing that hydrogen can reduce the cohesive energy of iron grain boundaries by as much as 40% [39, 40]. The embrittlement is particularly pronounced at high-angle grain boundaries, where hydrogen-induced decohesion facilitates brittle intergranular fracture.

Experimental observations corroborate these theoretical findings. Fracture surfaces of high-strength steels often display intergranular morphology under hydrogen exposure, consistent with cohesive weakening rather than ductile rupture. However, despite extensive indirect evidence, direct in situ observation of HEDE remains limited by the challenges of detecting hydrogen at the atomic scale under mechanical loading [36].

4.1.2.2 Hydrogen-Enhanced Localized Plasticity (HELP)

Contrary to HEDE, which promotes brittle behavior by reducing bond strength, the HELP mechanism enhances dislocation activity, resulting in localized plastic deformation. First proposed by Beachem in 1972, HELP suggests that hydrogen reduces the interaction forces between dislocations and also modifies local elastic moduli, effectively softening the matrix. These effects promote dislocation glide and reduce the critical resolved shear stress necessary for slip.

HELP describes how hydrogen increases dislocation mobility by shielding elastic interactions between dislocations and obstacles. This enhancement leads to slip planarity, localization of plastic strain, and eventual ductile-to-brittle transitions under certain loading conditions. Direct TEM observations in high-purity metals have shown increased dislocation velocities and reduced spacing in pileups under hydrogen charging [41, 42]. This localization contributes to shear banding and early void nucleation precursors to ductile fracture in hydrogen-charged specimens.

In situ transmission electron microscopy (TEM) studies have revealed that dislocations move more freely and form dense pile-ups in hydrogen-charged specimens compared to hydrogen-free controls [34, 43]. Macroscopic manifestations include the formation of slip bands, microvoids, and shear localization zones, particularly ahead of crack tips. While this mechanism alone may not directly cause fracture, it serves to concentrate deformation in narrow bands, preconditioning the material for subsequent decohesion or crack propagation.

A seminal contribution to the development of the HELP mechanism was provided by Birnbaum and Sofronis [44], who demonstrated that hydrogen significantly enhances dislocation mobility by lowering the barriers for dislocation glide and shielding elastic stress fields. Their work combined in situ transmission electron microscopy with micromechanical analysis to show that hydrogen promotes intense slip localization near crack tips without requiring void nucleation or cleavage. These insights established a theoretical and experimental foundation for interpreting hydrogen-assisted fracture as a manifestation of localized plastic softening rather than classical embrittlement.

The continuum-level consequences of the HELP mechanism were further developed by Sofronis et al. [45], who investigated hydrogen-induced shear localization using a bifurcation framework. By modeling hydrogen-enhanced softening as a concentration-dependent reduction in local yield stress and incorporating hydrogen effects into a pressure-sensitive constitutive law, they demonstrated that the presence of hydrogen significantly reduces the critical strain for localization. Their findings support the view that macroscale ductile failure under hydrogen exposure may result from the intensification of local plastic instabilities rather than brittle decohesion, aligning with experimental observations of slip banding and localized deformation in high hydrogen environments.

4.1.2.3 Adsorption-Induced Dislocation Emission (AIDE)

The AIDE mechanism, while related to HELP, emphasizes hydrogen's role in lowering the energy barrier for dislocation emission from freshly formed crack surfaces or pre-existing flaws. Hydrogen atoms adsorbed at these surfaces reduce the surface energy and facilitate atomic shearing across lattice planes, thereby triggering dislocation emission under lower applied stress.

This mechanism is particularly important in materials where hydrogen diffusion is limited or when loading rates are high enough that bulk diffusion cannot occur quickly. Under such conditions, the dominant hydrogen interaction is with the crack surface itself, promoting quasi-cleavage fracture modes [35, 46]. Molecular dynamics simulations have further shown that hydrogen coverage enhances crack-tip mobility, allowing alternating cycles of emission and cleavage depending on the local hydrogen concentration and stress state.

4.1.2.4 Hydride Formation and Precipitation

In specific alloy systems, particularly those involving titanium, zirconium, vanadium, or niobium, hydrogen can precipitate as brittle hydride phases. These hydrides form under suitable temperature and hydrogen concentration conditions and typically exhibit lower toughness and higher crack susceptibility than the surrounding matrix. The resulting embrittlement is often intergranular and brittle in nature.

Experimental studies on Zr-based alloys used in nuclear fuel cladding and Ti alloys used in aerospace have documented the nucleation and growth of δ-$ZrH_{1.6}$ and TiH_2 at grain boundaries and crack tips, where they serve as crack initiation sites [47, 48]. Although not generally observed in steels or Ni-based superalloys, hydride-induced fracture remains a critical concern in hydride-forming materials, especially under sustained hydrogen charging.

4.1.2.5 Synergistic Interactions and Plasticity-Mediated Decohesion

Recent experimental and theoretical studies increasingly suggest that these mechanisms do not act in isolation. Instead, hydrogen-assisted failure often involves overlapping phenomena that evolve during the deformation process. A prime example is "plasticity-mediated decohesion," a concept supported by Nagao et al., in which HELP-driven dislocation pile-ups concentrate stress at hydrogen-weakened grain boundaries, ultimately triggering intergranular fracture [43]. Similarly, in steels subjected to cyclic or sustained hydrogen exposure, early plastic strain localization (HELP) transitions into brittle decohesion (HEDE) once a critical hydrogen concentration or stress state is reached [34, 36].

This synergy underscores the need to consider not only material composition and microstructure, but also service conditions, strain rate, and hydrogen flux when evaluating hydrogen embrittlement susceptibility. The interplay between mechanisms is particularly critical in high-strength structural alloys and single crystals under complex loading, where hydrogen's role evolves dynamically during crack initiation and growth.

4.1.3 Hydrogen Transport and Trapping

Understanding the transport and trapping behavior of hydrogen in metals is essential for interpreting and modeling hydrogen embrittlement. Hydrogen ingress, mobility, and accumulation are governed by a combination of interstitial diffusion and site-specific trapping, both of which are strongly influenced by temperature, microstructure, and applied stress.

4.1.3.1 Lattice Diffusion and Solubility

In most metals, hydrogen diffuses by hopping between interstitial lattice sites. In body-centered cubic (BCC) lattices, hydrogen prefers tetrahedral sites, while in face-centered cubic (FCC) metals, it typically occupies octahedral sites. Due to the openness of the BCC lattice, hydrogen diffusion is considerably faster in BCC metals (e.g., ferritic steels) than in FCC counterparts (e.g., austenitic stainless steels) [31, 37].

The diffusion coefficient D obeys an Arrhenius relation:

$$D = D_0 \exp\left(-\frac{Q}{RT}\right), \tag{4.1}$$

where D_0 is the pre-exponential factor, Q is the activation energy for diffusion, R is the universal gas constant, and T is the absolute temperature. In addition to temperature, hydrostatic tensile stress can enhance hydrogen solubility and diffusion by lowering the chemical potential of hydrogen in regions of triaxial tension [38].

4.1.3.2 Trapping at Dislocations, Interfaces, and Precipitates

Microstructural heterogeneities serve as hydrogen traps, which can significantly reduce effective diffusivity and increase local hydrogen concentrations. These traps are classified into two broad types:

- **Reversible (weak) traps** — associated with dislocations, low-angle grain boundaries, and interstitial sites with low binding energy ($\lesssim 30$ kJ/mol).
- **Irreversible (strong) traps** — associated with vacancies, carbides, or other second-phase particles, often exhibiting binding energies > 50 kJ/mol.

Kumnick and Johnson's classical permeation study showed that cold-worked iron introduces deep traps with binding energies around 60 kJ/mol, likely due to dislocation structures and strain-induced vacancies [32]. Such traps retard hydrogen diffusion but enhance local hydrogen accumulation, which is critical for embrittlement phenomena.

4.1.3.3 Thermodynamics of Trapping (Oriani's Model)

To describe the interaction between diffusing hydrogen and microstructural traps, Oriani proposed a local equilibrium model. It assumes that lattice and trap sites maintain thermodynamic equilibrium, leading to a relationship for the fraction of occupied traps θ_T as:

$$\frac{\theta_T}{1-\theta_T} = \frac{\theta_L}{1-\theta_L} \exp\left(\frac{W_b}{RT}\right) \tag{4.2}$$

where θ_L is the occupancy of lattice sites and W_b is the trap binding energy [31]. Although powerful, Oriani's model is most accurate under conditions of low hydrogen concentration and static microstructure. Extensions are often necessary to account for trap saturation and mobile trap evolution during deformation.

4.1.3.4 Experimental Methods and Limitations

A variety of experimental techniques are employed to investigate hydrogen transport and trapping:

- **Permeation experiments**: Used to extract apparent diffusion coefficients and trap densities by measuring breakthrough curves in membrane-type setups [36].
- **Thermal Desorption Spectroscopy (TDS)**: Determines trap energy distributions by monitoring hydrogen release with increasing temperature.
- **Atom Probe Tomography (APT)**: Enables 3D mapping of hydrogen with subnanometer resolution but faces challenges in quantifying hydrogen under stress.
- **Secondary Ion Mass Spectrometry (SIMS)**: Offers depth profiling capabilities but suffers from poor spatial precision at trap scales.

Despite their usefulness, these methods face critical limitations. Hydrogen is difficult to detect at low concentrations, and most techniques lack the ability to resolve its behavior in situ under mechanical load. As highlighted by Tunes et al., even with modern instrumentation, direct nanoscale quantification of hydrogen under realistic service conditions remains elusive [36].

To address these experimental limitations, numerical studies have begun to explore the effect of microstructural features—particularly grain boundaries—on hydrogen transport. Díaz et al. [49] compared two modeling approaches for simulating hydrogen permeation tests in iron: a one-dimensional continuum model based on Oriani-type trapping and a polycrystalline finite element model using Voronoi tessellation. Their results revealed that while the continuum model captured transient trapping effects, only the polycrystalline model accurately reproduced the steady-state hydrogen flux, due to its ability to account for grain boundary diffusivity and segregation. These findings highlight the importance of incorporating realistic microstructural geometry in predictive modeling of hydrogen transport and trapping.

4.1.4 Modeling Approaches for Hydrogen Embrittlement

The modeling of hydrogen embrittlement (HE) spans a wide spectrum of approaches, from empirical degradation laws to fully coupled, thermodynamically consistent formulations. While no single model can universally capture all observed manifestations of HE, each modeling class offers insights at different scales and for specific material systems. This section categorizes existing approaches into six major families, beginning with phenomenological models and ending with fracture-based frameworks, to form a bridge between fundamental mechanisms and the advanced results presented later in this thesis.

4.1.4.1 Phenomenological and Empirical Models

Phenomenological models form the earliest and most application-oriented class of hydrogen embrittlement simulations. These models do not explicitly consider microstructural features or underlying mechanisms such as HELP or HEDE; instead, they focus on reproducing observed macroscopic behavior through modified constitutive laws, critical stress thresholds, or empirical degradation functions.

One classical example is the use of a critical hydrogen concentration or threshold stress below which hydrogen-induced cracking does not occur. McMahon and Troiano proposed fracture criteria based on critical hydrogen-modified cohesive strength, where embrittlement was assumed to occur once local stress exceeded this reduced limit [50]. Such concepts remain in use for assessing structural steels under cathodic charging.

In finite element applications, such as those implemented in commercial packages like ABAQUS, engineers often adopt scalar degradation functions that reduce yield strength, fracture toughness, or ductility as a function of local hydrogen concentration:

$$\sigma_y(c) = \sigma_{y,0}\left(1 - \chi \frac{c}{c_{\text{sat}}}\right) \tag{4.3}$$

where $\sigma_{y,0}$ is the intrinsic yield stress, c is the local hydrogen concentration, c_{sat} is the saturation concentration, and $\chi \in [0, 1]$ is a phenomenological sensitivity parameter [40, 51].

Empirical fracture criteria are also used, particularly in the context of hydrogen-assisted cracking (HAC). These include modified Gurson models where porosity evolution is accelerated in the presence of hydrogen, or fracture toughness reduction factors in the critical J-integral or CTOD values.

While these models are computationally efficient and easy to calibrate against engineering data, they lack predictive power outside of the conditions under which they were fitted. Moreover, they fail to capture the strong coupling between diffusion, stress, plasticity, and trap occupancy observed in modern experiments. As such, they are best suited for engineering design and conservative screening, rather than mechanistic investigation.

4.1.4.2 Diffusion–Mechanics Coupling Models

To more accurately capture hydrogen's behavior in metals, especially its stress-driven migration and interactions with microstructural features, several models have emerged that couple mechanical deformation with hydrogen diffusion. These approaches build on Fick's law but include modifications to account for stress-affected chemical potentials and trap-lattice interactions.

A widely used extension of Fickian transport is:

$$\mathbf{J} = -D\nabla c + \frac{DcV_H}{RT}\nabla\sigma_H \tag{4.4}$$

where $\mathbf{J}$ is the hydrogen flux, D is the diffusivity, c the concentration, V_H the partial molar volume, σ_H the hydrostatic stress, and T temperature. This formulation highlights how hydrostatic tensile stress attracts hydrogen, thereby increasing local concentrations at crack tips or dislocation pile-ups [52, 53].

Advanced models like those of Sofronis and McMeeking incorporate finite strain elasticity, transient trap kinetics, and time-dependent loading. These models are often used in finite element analyses to simulate long-term hydrogen exposure or cyclic stress-driven accumulation. They also serve as a basis for hydrogen-assisted cracking simulations in structural steels and high-performance alloys.

Martínez-Pañeda et al. [54] advanced this class of models by incorporating strain gradient plasticity (SGP), allowing them to capture dislocation hardening effects near crack tips. Their results showed that classical J2 plasticity underestimates both hydrostatic stress and hydrogen concentration in the process zone. By using SGP, they achieved stress and hydrogen field predictions that better align with experimental SIMS data, underlining the importance of microstructure-sensitive plasticity theories in embrittlement modeling.

4.1.4.3 Continuum Damage Mechanics and Failure Criteria

Continuum Damage Mechanics (CDM) provides a scalar or tensorial framework to represent material degradation due to microvoids, decohesion, or microcrack nucleation—phenomena strongly influenced by hydrogen. In HE modeling, CDM is often enhanced with hydrogen concentration-dependent degradation laws.

One common approach is to define a scalar damage variable D, whose evolution depends on local stress, plastic strain, and hydrogen concentration:

$$\dot{D} = f(\sigma, \varepsilon^p, c) \tag{4.5}$$

with damage affecting material stiffness or yield surface degradation. Variants of the Gurson-Tvergaard-Needleman (GTN) model have also been modified to incorporate accelerated void growth or coalescence in the presence of hydrogen [51, 55].

These models are especially useful for predicting ductile-to-brittle transitions and loss of load-bearing capacity, particularly under monotonic or low-cycle loading. However, they often require extensive parameter fitting and lack direct links to dislocation-scale mechanisms.

4.1.4.4 Crystal Plasticity-Based Formulations

Crystal plasticity (CP) models offer a physics-based approach to simulating hydrogen embrittlement by resolving slip on individual crystallographic systems. Hydrogen can affect plastic flow at this level by modifying the critical resolved shear stress, enhancing slip planarity, or promoting localization (HELP mechanism).

In CP frameworks, slip system shear rates are modified as:

$$\dot{\gamma}^{\alpha} = \dot{\gamma}_0 \left(\frac{|\tau^{\alpha}|}{\tau_c^{\alpha}(c)} \right)^n \text{sign}(\tau^{\alpha}) \tag{4.6}$$

where $\tau_c^{\alpha}(c)$ is the hydrogen-dependent slip resistance, often reduced with increasing c, the local hydrogen concentration.

More recent formulations incorporate hydrogen transport equations directly into the CP framework, enabling the simulation of anisotropic trap saturation, orientation-sensitive slip, and hydrogen-enhanced dislocation motion [56, 57].

4.1.4.5 Fracture Models: Cohesive Zone and Phase-Field Approaches

To model crack initiation and propagation explicitly, two advanced methods are widely employed: Cohesive Zone Models (CZMs) and Phase-Field Models (PFMs). Both have been extended to incorporate hydrogen effects, particularly HEDE-type decohesion and HELP-induced softening.

In hydrogen-sensitive CZMs, the cohesive traction–separation law is modified by local hydrogen concentration:

$$T_n = g(c) T_{n0} \left(1 - \frac{\delta_n}{\delta_c} \right) \tag{4.7}$$

where $g(c)$ is a degradation function that reduces peak traction as hydrogen concentration increases. This allows the simulation of accelerated crack advance in high hydrogen zones [40, 58].

Phase-field models offer a variational framework to simulate complex crack paths without tracking interfaces. Hydrogen enters these models by modifying the fracture energy functional:

$$\mathcal{G}_c(c) = \mathcal{G}_0 \left(1 - \eta \frac{c}{c_{\text{sat}}}\right) \tag{4.8}$$

where $\mathcal{G}_c$ is the hydrogen-degraded critical energy release rate, and η is a phenomenological factor. Such models enable the simulation of both cohesive failure and diffusively driven degradation, particularly in multiphysics scenarios.

An advanced phase-field framework for hydrogen embrittlement has been developed by Martínez-Pañeda et al. [59], where the fracture energy degradation is directly linked to hydrogen coverage via quantum mechanics-informed relations. Their model has been applied to a wide range of boundary value problems including notched bars and internal hydrogen cracking, confirming its robustness and predictive capability.

4.1.4.6 Comparative Assessment and Modeling Limitations

Each modeling approach has distinct strengths and limitations. Phenomenological models are simple and fast but limited to calibrated conditions. Diffusion–mechanics models capture transport effects but often miss fracture initiation. Crystal plasticity offers mechanistic fidelity but at high computational cost. Cohesive and phase-field models excel at crack path prediction but require dense meshes and accurate energy parameters.

A key limitation across all models remains the lack of definitive in-situ experimental validation for hydrogen concentration and stress localization at the microscale. As such, the selection of an appropriate model must be guided by the material system, available data, and the intended application whether predictive design or mechanistic understanding.

The next section introduces a thermodynamically consistent framework for modeling hydrogen embrittlement in single crystals and polycrystals, building upon the physical principles and modeling paradigms discussed above.

4.2 Thermodynamical Framework for Coupled Diffusion–Deformation Theory

Modeling hydrogen embrittlement (HE) has evolved significantly, progressing from phenomenological laws to continuum models that couple mechanical deformation, hydrogen diffusion, and microstructural trapping. One of the earliest rigorous attempts to couple hydrogen diffusion and mechanical behavior was made by Sofronis and McMeeking [52], who formulated a small-strain finite element model incorporating Oriani's local equilibrium trapping theory. Their analysis demonstrated how plasticity-induced hydrostatic stress gradients, combined with trapping kinetics, strongly influence hydrogen accumulation near blunting crack tips.

Krom and Bakker [60] extended this framework by introducing transient formulations and incorporating large deformation effects. Their work illustrated that plastic deformation not only concentrates hydrogen but also generates new trapping sites, which must be accounted for to predict realistic hydrogen profiles.

A major advancement in understanding hydrogen transport in metals came from Oriani [31], who introduced a thermodynamic theory of reversible hydrogen trapping. Assuming local equilibrium between mobile and trapped populations, Oriani derived a closed-form relationship between lattice and trap concentrations. His model shows that the effective diffusivity is reduced as trap density or binding energy increases, and he identified regimes in which the classical notion of phenomenological diffusivity becomes invalid.

Experimental support for these theoretical developments was later provided by Kumnick and Johnson [32], who measured hydrogen permeation in deformed iron. Their time-lag experiments identified deep traps with binding energies around 60 kJ/mol and trap densities increasing by three orders of magnitude with plastic deformation. These results confirmed the dominant role of dislocations and associated debris in generating irreversible hydrogen traps.

A key step toward thermodynamically consistent continuum modeling was made by Anand [61], who developed a coupled theory for species diffusion and large elastic–plastic deformations. This framework used the Coleman–Noll procedure to derive constitutive relations from a Helmholtz free energy potential and accounted for dissipation due to plastic flow and chemical potential gradients.

Di Leo and Anand [62] extended this formulation by introducing separate chemical potentials for lattice and trapped hydrogen. Oriani's local equilibrium condition emerged naturally within their thermodynamic structure, enabling consistent treatment of equilibrium and non-equilibrium hydrogen transport and trapping. A similar modeling framework was developed by Barrera et al. [63], who implemented a coupled mechanical–diffusion finite element model incorporating Oriani-type trapping. Their study highlighted that hydrogen-enhanced plasticity alone is insufficient to induce failure unless it is combined with stress localization or decohesion, emphasizing the need to consider multiple interacting mechanisms in hydrogen embrittlement modeling.

Aslan [64] numerically implemented this framework for metals undergoing large plastic deformations, incorporating experimental calibration of trapping effects. His simulations demonstrated how trap-enhanced hydrogen accumulation aligns with regions of high stress and strain localization, enabling the modeling of HELP-type behavior.

Recent developments also emphasize the role of microstructure. Li et al. [65] implemented a grain boundary-sensitive crystal plasticity framework, showing that hydrogen segregation concentrates at high-angle grain boundaries and triple junctions. Lu et al. [66] examined hydrogen-induced fracture in Ni-based single crystals, finding that dislocation–interface interactions and γ/γ' boundaries play a critical role in crack initiation.

These contributions provide the necessary theoretical and numerical foundation for the current study, which aims to extend such frameworks to single-crystal finite strain settings by integrating Oriani-type trapping, dislocation-driven transport, and stress-assisted diffusion in a thermodynamically consistent manner.

4.2.1 Kinematics

Consider a homogeneous body B happen to be in a reference configuration and a motion of any point on body B can be mapped by a smooth function $\boldsymbol{x} = \chi(\boldsymbol{X}, t)$ with given deformation gradient, velocity and velocity gradient as

$$\mathbf{F} = \nabla\chi, \qquad \mathbf{v} = \dot{\chi}, \qquad \mathbf{L} = grad(\mathbf{v}) = \dot{\mathbf{F}}\mathbf{F}^{-1} \tag{4.9}$$

Deformation gradient can be decomposed into elastic and plastic parts by the Kröner Decomposition in the form

$$\mathbf{F} = \mathbf{F}^e\mathbf{F}^p \tag{4.10}$$

where $\mathbf{F}^e$ is the elastic distortion represents stretching and rotation and $\mathbf{F}^p$ represents the local deformation caused by plastic distortion. Then the velocity gradient decomposed into

$$\mathbf{L} = \mathbf{L}^e + \mathbf{F}^e\mathbf{L}^p\mathbf{F}^{e-1} \tag{4.11}$$

where

$$\mathbf{L}^e = \dot{\mathbf{F}}^e\mathbf{F}^{e-1}, \qquad \text{and} \qquad \mathbf{L}^p = \dot{\mathbf{F}}^p\mathbf{F}^{p-1} \tag{4.12}$$

The stretching and spin tensors defined as

$$\begin{aligned} \mathbf{D}^e &= \text{sym}\mathbf{L}^e, \qquad \mathbf{W}^e = \text{skw}\mathbf{L}^e \\ \mathbf{D}^p &= \text{sym}\mathbf{L}^p, \qquad \mathbf{W}^p = \text{skw}\mathbf{L}^p \end{aligned} \tag{4.13}$$

Assume the volume ratio

$$J \overset{\text{def}}{=} \det\mathbf{F} \tag{4.14}$$

and by 4.10

$$J = J^e J^p, \qquad J^e \overset{\text{def}}{=} \det\mathbf{F}^e > 0 \qquad \text{and} \qquad J^p \overset{\text{def}}{=} \det\mathbf{F}^p > 0, \tag{4.15}$$

can be concluded with $\mathbf{F}^e$ and $\mathbf{F}^p$ are invertible.

Assuming plastic flow is incompressible and irrotational will give

$$J^p = \det\mathbf{F}^p = 1 \qquad \text{and} \qquad tr\mathbf{L}^p = tr\mathbf{D}^p = \mathbf{W}^p = 0 \tag{4.16}$$

The right polar decomposition of $\mathbf{F}^e$ is

$$\mathbf{F}^e = \mathbf{R}^e\mathbf{U}^e \tag{4.17}$$

where $\mathbf{R}^e$ is a rotation tensor and $\mathbf{U}^e$ is the right stretch tensor. The right Cauchy-Green tensor and the Hencky's strain is then

$$\mathbf{C}^e = (\mathbf{U}^e)^2 = \mathbf{F}^{eT}\mathbf{F}^e, \qquad \mathbf{E}^e = ln(\mathbf{U}^e) \tag{4.18}$$

and by 4.16 and 4.12

$$\mathbf{L}^p = \mathbf{D}^p, \qquad \dot{\mathbf{F}}^p = \mathbf{D}^p\mathbf{F}^{p-1} \tag{4.19}$$

Defining an equivalent tensile plastic strain rate and equivalent tensile stress as

$$\dot{\overline{\epsilon}}^p \overset{\text{def}}{=} \sqrt{\frac{2}{3}}|\mathbf{D}^p|, \qquad \overline{\sigma} = \sqrt{\frac{3}{2}}|\mathbf{M}_0^e| \tag{4.20}$$

where $\mathbf{M}_0^e$ is being deviatoric Mandel stress and by knowing codirectionality of plastic flow of which direction of plastic flow $\mathbf{N}^p$ and direction of deviatoric stress is parallel so that

$$\mathbf{N}^p = \frac{\mathbf{D}^p}{|\mathbf{D}^p|} = \frac{\mathbf{M}_0^e}{|\mathbf{M}_0^e|} \tag{4.21}$$

One can write plastic stretching tensor as then

$$\mathbf{D}^p = \sqrt{\frac{3}{2}}\dot{\bar{\epsilon}}^p \mathbf{N}^p \tag{4.22}$$

4.2.2 Method of Virtual Power and Balance of Forces

The principle of virtual power serves as a foundational tool for deriving balance laws in continuum mechanics, particularly under large deformation. It replaces the classical approach based on direct appeal to Newton's laws with a variational framework that provides a natural entry point for complex material theories such as those involving internal variables, defects, and dissipation mechanisms.

Let $\mathcal{B}$ denote the reference configuration of the body and let $\boldsymbol{x} : \mathcal{B} \to \mathbb{R}^3$ denote its motion. At each material point $\mathbf{X} \in \mathcal{B}$, the deformation gradient is $\mathbf{F} = \nabla \boldsymbol{x}$ and the velocity is $\mathbf{v} = \dot{\boldsymbol{x}}$. Let $\delta\mathbf{v}$ be an admissible virtual velocity field.

The internal virtual power $\mathcal{P}_{\text{int}}$ and external virtual power $\mathcal{P}_{\text{ext}}$ defined as

$$\mathcal{P}_{\text{int}}(\delta\mathbf{v}) = \int_{\mathcal{B}} \mathbf{T}_\mathbf{R} : \nabla\delta\mathbf{v}\, \mathrm{d}V, \qquad \mathcal{P}_{\text{ext}}(\delta\mathbf{v}) = \int_{\mathcal{B}} \rho\mathbf{b} \cdot \delta\mathbf{v}\, \mathrm{d}V + \int_{\partial\mathcal{B}} \bar{\mathbf{t}} \cdot \delta\mathbf{v}\, \mathrm{d}A \tag{4.23}$$

where $\mathbf{T}_\mathbf{R}$ is the first Piola–Kirchhoff stress tensor, ρ is the reference mass density, $\mathbf{b}$ is the body force per unit mass, and $\bar{\mathbf{t}}$ is the prescribed traction on the boundary.

The principle of virtual power asserts that, for all admissible virtual velocities $\delta\mathbf{v}$ vanishing on the Dirichlet part of the boundary, the total virtual power of internal forces equals that of external forces:

$$\mathcal{P}_{\text{int}}(\delta\mathbf{v}) = \mathcal{P}_{\text{ext}}(\delta\mathbf{v}) \tag{4.24}$$

Applying this principle to arbitrary $\delta\mathbf{v}$ yields the local form of the balance of linear momentum in the reference configuration:

$$\text{Div}\,\mathbf{T}_{\mathbf{R}} + \rho\mathbf{b} = \rho\ddot{\boldsymbol{x}} \quad \text{in } \mathcal{B} \tag{4.25}$$

with boundary condition

$$\mathbf{T}_{\mathbf{R}}\mathbf{n} = \bar{\mathbf{t}} \quad \text{on } \partial\mathcal{B}_N \tag{4.26}$$

where $\mathbf{n}$ is the outward unit normal vector in the reference configuration and $\partial\mathcal{B}_N$ is the Neumann part of the boundary.

In the context of finite-strain plasticity with internal variables (such as $\mathbf{F}^p$), the principle of virtual power can be extended by including additional power-conjugate pairs. For example, if plastic flow is driven by a dissipation mechanism, introducing a microforce balance acting on $\mathbf{F}^p$:

$$\int_{\mathcal{B}} \boldsymbol{\Xi} : \delta\dot{\mathbf{F}}^p \, \mathrm{d}V \tag{4.27}$$

where $\boldsymbol{\Xi}$ is a generalized stress (microforce) conjugate to $\dot{\mathbf{F}}^p$. This term contributes to the dissipation inequality and plays a central role in defining the constitutive structure under the thermodynamical framework.

This variational structure not only delivers the classical momentum balance but also sets the stage for coupling with species transport, internal evolution equations, and dissipation—all of which will follow in subsequent sections.

4.2.3 Balance Law for Hydrogen Diffusion

For a given material point X within a body of volume V and surface S, the total moles of hydrogen atoms per unit volume in a fixed reference configuration are denoted as $C_{total}(X,t)$. The variation in hydrogen concentration within an arbitrary spatial region U is described by a flux $\boldsymbol{j}(X,t)$, which represents the moles of diffusing species per unit area per unit time. Consequently, the principle of mass conservation requires that

$$\frac{\partial}{\partial t}\int_B C_{total}\, dV + \int_{dB} \boldsymbol{j}.\boldsymbol{n}\, dS = 0 \tag{4.28}$$

and applying Gauss divergence on the integral over ∂V gives

$$\dot{C}_{total} = -Div\boldsymbol{j} \tag{4.29}$$

where total concentration of hydrogen is

$$C_{total} = C_T + C_L \tag{4.30}$$

with C_L, C_T are trapped and lattice hydrogen contcentration respectively.

Hydrogen flux $\boldsymbol{j}$ is obey Fick's Law of diffusion

$$\boldsymbol{j} = -m\nabla\mu \tag{4.31}$$

here m is the mobility of the diffusing species and μ is the chemical potential. Assuming the mobility of the trapped hydrogen atoms is zero, inserting equation 4.30 into equtaion 4.29 will give

$$\dot{C_T} + \dot{C_L} = Div(m_L\nabla\mu_L) \tag{4.32}$$

Trapped hydrogen concentration will be discussed in the following sections.

4.2.4 Balance Equations

To develop a thermodynamically consistent framework for coupled deformation–diffusion processes, beginning by stating the first and second laws of thermodynamics for the open system defined over a body $\mathcal{B}$ in the reference configuration.

1. **Balance of Internal Energy** Let e denote the specific internal energy (per unit reference volume), r the external heat supply per unit reference volume, and $\mathbf{q}$ the heat flux vector in the reference configuration. The internal energy balance is

$$\dot{e} = \mathbf{T_R} : \dot{\mathbf{F}} - \mathrm{Div}\,\mathbf{q} + r + \mu_{\mathrm{L}}\dot{C}_{\mathrm{L}} + \mu_{\mathrm{T}}\dot{C}_{\mathrm{T}} \tag{4.33}$$

   Here, μ_{L} and μ_{T} denote the chemical potentials associated with lattice and trapped hydrogen, respectively. The last two terms represent the chemical work done by hydrogen transport and trapping.

2. **Entropy Imbalance** Let η be the specific entropy per unit reference volume. The second law of thermodynamics requires that the rate of entropy production is non-negative:

$$\dot{\eta} \geq -\mathrm{Div}\left(\frac{\mathbf{q}}{\theta}\right) + \frac{r}{\theta} \tag{4.34}$$

   where θ denotes the absolute temperature. This form corresponds to the Clausius–Duhem inequality in its local form.

3. **Free Energy Imbalance** Defining the specific Helmholtz free energy ψ as

$$\psi = e - \theta\eta \tag{4.35}$$

   Combining the energy balance (4.33) with the entropy inequality (4.34) yields the reduced dissipation inequality:

$$\dot{\psi} + \eta\dot{\theta} - \mathbf{T_R} : \dot{\mathbf{F}} + \mu_{\mathrm{L}}\dot{C}_{\mathrm{L}} + \mu_{\mathrm{T}}\dot{C}_{\mathrm{T}} + \frac{1}{\theta}\mathbf{q}\cdot\nabla\theta \leq 0 \tag{4.36}$$

This inequality serves as the basis for formulating constitutive equations in a thermodynamically consistent manner. In particular, it will be ensured that the constitutive forms of ψ, $\mathbf{T_R}$, μ_{L}, and μ_{T} satisfy this inequality under arbitrary admissible processes.

Note that this formulation admits multiple coupled fields (mechanics, species, temperature), but it will be later specialize to isothermal conditions to simplify the analysis of hydrogen diffusion and plastic deformation.

4.2.5 Constitutive Equations

Considering the following dependencies for the free energy, stress, the entropy and the chemical potentials:

$$\psi = \psi(\Phi) \tag{4.37}$$

where Φ is the list of variables $(\mathbf{C}^e, \bar{\dot{\epsilon}}^p, C_{\mathrm{L}}, C_{\mathrm{T}}, \theta)$. Stress power per unit volume is given as

$$\begin{aligned}\mathbf{T}_R : \dot{\mathbf{F}} &= \mathbf{T}_R : \left(\dot{\mathbf{F}}^e\mathbf{F}^p + \mathbf{F}^e\dot{\mathbf{F}}^p\right) \\ &= \left(J\mathbf{F}^{e-1}\mathbf{T}\mathbf{F}^{e-T}\right) : \left(\mathbf{F}^{eT}\dot{\mathbf{F}}^e\right) + \left(\mathbf{C}^e J\mathbf{F}^{e-1}\mathbf{T}\mathbf{F}^{e-T}\right) : \mathbf{L}^p\end{aligned} \tag{4.38}$$

The time derivative of the right Cauchy-Green tensor is

$$\dot{\mathbf{C}}^e = \dot{\mathbf{F}}^{eT}\mathbf{F}^e + \mathbf{F}^{eT}\dot{\mathbf{F}}^e \tag{4.39}$$

Thus using the relation

$$\mathbf{T}^e = \mathbf{F}^{e-1}\mathbf{F}^{e-T}\mathbf{M}^e \tag{4.40}$$

the stress power per unit volume can be written as,

$$\mathbf{T}_R : \dot{\mathbf{F}} = \frac{1}{2}\mathbf{T}^e : \dot{\mathbf{C}}^e + \mathbf{M}^e : \mathbf{L}^p \tag{4.41}$$

Substituting corresponding power terms into the free energy imbalance will give

$$\left(\frac{\partial\psi(\Phi)}{\partial\theta} + \eta\right)\dot{\theta} + \left(\frac{\partial\psi(\Phi)}{\partial\mathbf{C}^e} - \frac{1}{2}\mathbf{T}^e\right) : \dot{\mathbf{C}}^e + \left(\frac{\partial\psi(\Phi)}{\partial C_L} - \mu_L\right)\dot{C}_L + \left(\frac{\partial\psi(\Phi)}{\partial C_T} - \mu_T\right)\dot{C}_T + \left(\frac{\partial\psi(\Phi)}{\partial\overline{\epsilon}^p} - \overline{\sigma}\right)\dot{\overline{\epsilon}}^p + \frac{1}{\theta}\mathbf{q}.\nabla\theta \leq 0 \tag{4.42}$$

To guarantee that the inequality holds for all admissible processes, defining the constitutive relations as:

$$\mathbf{T}^e = 2\frac{\partial\psi}{\partial\mathbf{C}^e} \tag{4.43}$$

$$\mu_{\mathrm{L}} = \frac{\partial\psi}{\partial C_{\mathrm{L}}} \tag{4.44}$$

$$\mu_{\mathrm{T}} = \frac{\partial\psi}{\partial C_{\mathrm{T}}} \tag{4.45}$$

$$\eta = -\frac{\partial\psi}{\partial\theta} \tag{4.46}$$

With these definitions, one of the remaining term is

$$Y = \frac{\partial \psi(\Phi)}{\partial \overline{\epsilon}^p}, \quad (\overline{\sigma} - Y)\dot{\overline{\epsilon}}^p \tag{4.47}$$

defines the plastic flow condition and the latter inequality reduces to the purely dissipative terms:

$$\frac{1}{\theta}\mathbf{q} \cdot \nabla\theta \geq 0 \tag{4.48}$$

which holds for all heat conduction processes consistent with Fourier's law.

4.2.6 Oriani's Local Equilibrium Theory

Hydrogen atoms in metallic solids may reside in two types of sites: interstitial lattice sites and microstructural traps such as dislocations, grain boundaries, and vacancies. Oriani's theory [31] postulates a local equilibrium between these two populations, enabling a thermodynamic relationship between their occupancies and concentrations.

Let θ_{L} and θ_{T} denote the site occupancies of lattice and trap sites, respectively. Under local equilibrium, the ratio of trap to lattice site occupancy satisfies

$$\frac{\theta_{\mathrm{T}}}{1 - \theta_{\mathrm{T}}} = \frac{\theta_{\mathrm{L}}}{1 - \theta_{\mathrm{L}}} K_{\mathrm{T}} \tag{4.49}$$

where K_{T} is the equilibrium constant defined by

$$K_{\mathrm{T}} = \exp\left(\frac{W_{\mathrm{B}}}{R\theta}\right) \tag{4.50}$$

with W_{B} the trap binding energy, R the universal gas constant, and θ the absolute temperature.

The concentrations of hydrogen in each type of site can be expressed in terms of occupancy and density of sites:

$$C_{\mathrm{L}} = \theta_{\mathrm{L}} \beta N_{\mathrm{L}} \tag{4.51}$$

$$C_{\mathrm{T}} = \theta_{\mathrm{T}} \alpha N_{\mathrm{T}} \tag{4.52}$$

Here, N_{L} is the number of solvent atoms per unit volume (e.g., $N_{\mathrm{L}} = N_A / V_{\mathrm{M}}$, with N_A Avogadro's number and V_{M} the molar volume), - β is the number of normal interstitial lattice sites (NILS) per solvent atom, - N_{T} is the number of traps per unit volume, - α is the number of hydrogen sites per trap.

Combining these with (4.49) yields an implicit relation between C_{T} and C_{L}:

$$\frac{C_{\mathrm{T}}}{\alpha N_{\mathrm{T}} - C_{\mathrm{T}}} = \frac{C_{\mathrm{L}}}{\beta N_{\mathrm{L}} - C_{\mathrm{L}}} K_{\mathrm{T}} \tag{4.53}$$

which can be rearranged to solve for C_{T} in terms of C_{L} and trap density N_{T}. This expression is central in defining the total hydrogen concentration:

$$C_{\mathrm{total}} = C_{\mathrm{L}} + C_{\mathrm{T}}(C_{\mathrm{L}}, N_{\mathrm{T}}) \tag{4.54}$$

The trap density N_{T} may evolve with plastic strain or dislocation density and will be modeled in subsequent sections.

Oriani's theory assumes fast kinetics such that equilibrium between sites is instantaneous. This is valid for reversible, mobile traps under moderate strain rates, and it provides a crucial coupling between chemical potential and mechanical deformation through the trap density.

4.2.7 Specialization of the Constitutive Equations

To complete the model, specifying explicit forms of the free energy and derive the associated constitutive relations for stress, chemical potentials, hydrogen flux, and trap–lattice exchange. These forms are chosen to ensure consistency with the dissipation inequality and to incorporate the effects of hydrogen on material behavior.

Note that the isothermal conditions will be used from now on.

4.2.7.1 Free Energy

The Helmholtz free energy per unit reference volume is postulated in additive form:

$$\psi = \psi^e + \psi^{chem} \tag{4.55}$$

The mechanical free energy ψ^e is a function of elastic deformation and may be chosen,

$$\begin{aligned}\psi^e(\mathbf{C}^e, C_L, C_T) = \mathrm{G}|\mathbf{E}^e| + \frac{1}{2}\left(\mathrm{K} - \frac{2}{3}\mathrm{G}\right)(\mathrm{tr}\mathbf{E}^e)^2 \\ - (3\mathrm{K}\beta)(C_L - C_{L0})(\mathrm{tr}\mathbf{E}^e) - (3\mathrm{K}\beta)(C_T - C_{T0})(\mathrm{tr}\mathbf{E}^e)\end{aligned} \tag{4.56}$$

where G and K are shear and bulk modulus respectively, β is coefficient of chemical expansion and C_{L0} and C_{T0} are reference lattice and trapped hydrogen concentrations.

Having the following chemical free energy

$$\psi_L(C_L) = \mu_{L0}C_L + R\nu N_L(\theta_L ln(\theta_L) + (1-\theta_L)ln(1-\theta_L)) \tag{4.57}$$

$$\psi_T(C_T, \overline{\epsilon}^p) = \mu_{T0}C_T + R\nu N_T(\theta_T ln(\theta_T) + (1-\theta_T)ln(1-\theta_T)) \tag{4.58}$$

Combining equations 4.56, 4.57 and 4.58

$$\begin{aligned}\psi = {} & \mathrm{G}|\mathbf{E}^e| + \frac{1}{2}\left(\mathrm{K} - \frac{2}{3}\mathrm{G}\right)(\mathrm{tr}\mathbf{E}^e)^2 \\ & - (3\mathrm{K}\beta)(C_L - C_{L0})(\mathrm{tr}\mathbf{E}^e) - (3\mathrm{K}\beta)(C_T - C_{T0})(\mathrm{tr}\mathbf{E}^e) \\ & + \mu_{L0}C_L + R\nu N_L(\theta_L ln(\theta_L) + (1-\theta_L)ln(1-\theta_L)) \\ & + \mu_{T0}C_T + R\nu N_T(\theta_T ln(\theta_T) + (1-\theta_T)ln(1-\theta_T))\end{aligned} \tag{4.59}$$

and by 4.43, 4.44 and 4.45

$$\begin{aligned}\mathbf{T}^e &= 2\mathrm{G}|\mathbf{E}_0^e| + \mathrm{K}(\mathrm{tr}\mathbf{E}^e)\mathbf{1} - (3\mathrm{K}\beta)(C_L - C_0)\mathbf{1} \\ \mu_L &= \mu_{L0} + R\nu ln\left(\frac{\theta_L}{1-\theta_L}\right) - (3\mathrm{K}\beta)(\mathrm{tr}\mathbf{E}^e) \\ \mu_T &= \mu_{T0} + R\nu ln\left(\frac{\theta_T}{1-\theta_T}\right) - (3\mathrm{K}\beta)(\mathrm{tr}\mathbf{E}^e)\end{aligned} \tag{4.60}$$

4.2.7.2 Hydrogen Trapping

Let us start defining with some useful definitions, number of moles of lattice sites and trap sites per unit reference volume, $\mathbf{N_L}$ and $\mathbf{N_T}$ respectively and given by

$$N_L \overset{\text{def}}{=} \varphi \frac{\rho}{\mathcal{M}} \qquad (mol/m^3) \tag{4.61}$$

where ρ is the mass density of the host metal (kg/m^3) and $\mathcal{M}$ the molar mass of the host metal (kg/mol).

$$N_T = \widetilde{N_T}(\overline{\epsilon}^p) \qquad (mol/m^3) \tag{4.62}$$

Based on experimental observations, number of moles of trap sites is a function of plastic strain.

Defining the **occupancy fraction**, θ_L and θ_T as

$$\theta_L \overset{\text{def}}{=} \frac{C_L}{N_L}, \qquad 0 \leq \theta_L \leq 1 \tag{4.63}$$

denote the occupancy fraction of the lattice sites, and

$$\theta_T \overset{\text{def}}{=} \frac{C_T}{N_T}, \qquad 0 \leq \theta_T \leq 1 \tag{4.64}$$

denote the occupancy fraction of the trap sites.

Assuming the mobility of the trapped hydrogen is zero, the local balance of hydrogen concentrations becomes single equation as

$$\dot{C_L} + \dot{C_T} = div(m_L \nabla \mu_L) \tag{4.65}$$

Oriani's theory states that there exist a local equilibrium between lattice concentration and trapped concentration such that

$$\frac{\theta_T}{1-\theta_T} = \frac{\theta_L}{1-\theta_L} K_T \tag{4.66}$$

where $K_T = exp\left(\frac{W_b}{R\nu}\right)$ is an equilibrium factor and W_b is the trap binding energy.

Using Oriani's theory the trapped concentration and its rate can be calculated as

$$\begin{aligned} C_T &= \frac{N_T}{1 + \frac{N_L}{K_T C_L}} \\ \dot{C_T} &= \frac{C_T(1-\theta_T)}{C_L}\dot{C_L} + \theta_T \frac{dN_T}{d\overline{\epsilon}^p}\dot{\overline{\epsilon}}^p \end{aligned} \tag{4.67}$$

4.2.7.3 Lattice Hydrogen Flux

Having established the constitutive expressions for the chemical potentials, proceeding to define the lattice hydrogen flux. This flux is governed by a stress-assisted Fickian law, where the chemical potential gradient serves as the primary driving force for hydrogen diffusion.

$$\boldsymbol{j_L} = -m_{\mathrm{L}} \nabla \mu_{\mathrm{L}} \tag{4.68}$$

and by 4.60

$$\nabla \mu_L = \frac{R\nu}{C_L}\nabla C_L - (3\mathrm{K}\beta)\nabla(\mathrm{tr}\mathbf{E}^e) \tag{4.69}$$

gives the lattice hydrogen concentration as

$$\mathbf{j_L} = -D_L \nabla C_L + \frac{D_L C_L}{R\nu} 3K\beta \nabla tr(\mathbf{E}^e) \tag{4.70}$$

with

$$D_L = m_L \frac{R\nu}{C_L} \tag{4.71}$$

4.2.7.4 Balance of Lattice Chemical Potential and Concentration

Recall equation 4.65, the change of total concentration is

$$\dot{C}_L + \dot{C}_T = div(m_L \nabla \mu_L) \tag{4.72}$$

and inserting 4.67 and 4.70

$$\frac{C_L + C_T(1-\theta_T)}{C_L}\dot{C}_L = div(D_L \nabla C_L) + div\left(\frac{D_L C_L}{R\nu} 3K\beta \nabla tr(\mathbf{E}^e)\right) - \theta_T \frac{dN_T}{d\overline{\epsilon}^p}\dot{\overline{\epsilon}}^p \tag{4.73}$$

or alternatively one can rewrite the local balance in terms of chemical potential as follows:

$$\frac{C_L + C_T(1-\theta_T)}{R\nu}\dot{\mu} = Div(m_L \nabla \mu_L) - \frac{C_L + C_T(1-\theta_T)}{R\nu}(3\mathrm{K}\beta)\mathrm{tr}\dot{\mathbf{E}}^e - \theta_T \frac{dN_T}{d\overline{\epsilon}^p}\dot{\overline{\epsilon}}^p \tag{4.74}$$

4.2.8 Governing Partial Differential Equations

By combining the previously derived expressions for stress, chemical potential, and lattice hydrogen flux, the governing partial differential equations are obtained. These equations describe the coupled evolution of mechanical equilibrium and hydrogen transport within the deforming solid.

1. Force Balance

$$Div\mathbf{T_R} - \rho\mathbf{b} = 0 \tag{4.75}$$

2. local balance of chemical potential

$$\frac{C_L + C_T(1-\theta_T)}{R\nu}\dot{\mu} = Div(m_L\nabla\mu_L) - \frac{C_L + C_T(1-\theta_T)}{R\nu}(3\mathrm{K}\beta)\mathrm{tr}\dot{\mathbf{E}}^e - \theta_T\frac{dN_T}{d\bar{\epsilon}^p}\dot{\bar{\epsilon}}^p. \tag{4.76}$$

4.3 Numerical Simulations and Discussion

This section presents numerical investigations conducted to analyze the coupling between mechanical deformation and hydrogen diffusion in metallic systems. The analysis begins with simulations based on J2 plasticity to validate the numerical framework and capture general features of hydrogen-assisted behavior, including comparisons with analytical solutions and classic single-edge notch (SEN) problems. The study is then extended using a crystal plasticity-based formulation to resolve crystallographic effects and microstructural influences on hydrogen transport.

4.3.1 J2 Plasticity-Based Modeling and Simulations

To establish a baseline and validate the finite element implementation, a J2 plasticity-based model coupled with hydrogen diffusion is first employed. This approach provides insight into macroscopic deformation-diffusion interactions and serves as a benchmark for subsequent simulations incorporating crystallographic anisotropy. The following subsections include validation against analytical diffusion solutions and simulations of hydrogen accumulation near crack tips.

4.3.1.1 Validation Against Analytical Solution

To verify the accuracy of the numerical implementation of hydrogen diffusion, the classical solution of Fick's second law in an infinite domain with a point-source initial condition is considered. The governing equation is given by:

$$\frac{\partial C(x,t)}{\partial t} = D\frac{\partial^2 C(x,t)}{\partial x^2} \tag{4.77}$$

where $C(x,t)$ is the hydrogen concentration, D is the diffusion coefficient, and x is the spatial coordinate.

The initial condition of a point source centered at the origin is considered as:

$$C(x, 0) = C_0\, \delta(x) \tag{4.78}$$

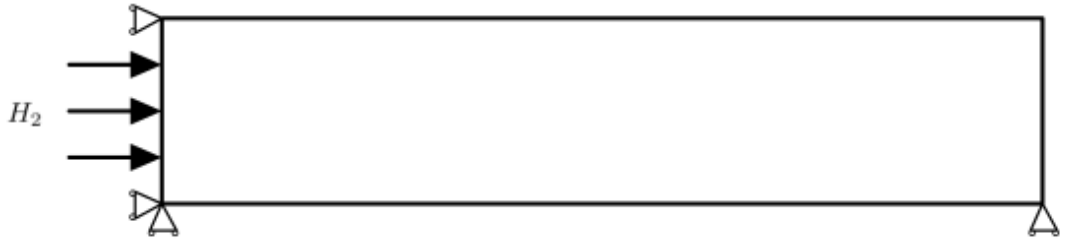
where $\delta(x)$ is the Dirac delta function and C_0 is the total amount of hydrogen introduced at the origin.

The analytical solution to this problem is given by the fundamental solution of the diffusion equation:

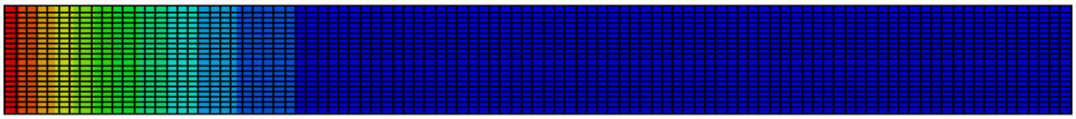
$$C(x, t) = \frac{C_0}{\sqrt{4\pi D}} \exp\left(-\frac{x^2}{4Dt}\right) \tag{4.79}$$

which describes a Gaussian distribution that spreads over time. The peak concentration decreases and the width increases with time, preserving the total amount of hydrogen.

Figure 4.2 illustrates the problem setup and simulation environment. Subfigure 4.2(a) shows the schematic of the bar geometry and boundary conditions, where a constant concentration of hydrogen(in our case constant chemical potential) is applied at the boundary. Subfigure 4.2(b) shows the numerical representation of the diffusion process with visualizing how hydrogen concentration distributes from the boundary into the bar over time.



(a)



(b)

Figure 4.2: (a) Schematic of the bar geometry and boundary conditions, (b) Hydrogen diffusion ahead of the boundary.

Figure 4.3 compares the analytical solution of Fick's law with the results obtained from the UMATHT and UEL subroutines. The graph demonstrates excellent agreement between the numerical and analytical solutions, showcasing the accuracy and reliability of the implemented subroutines. At $t = 10^3$s, the concentration located near the boundary, reflecting the early stages of diffusion. By $t = 10^4$s, the profile flattens as diffusion progresses deeper into the material.

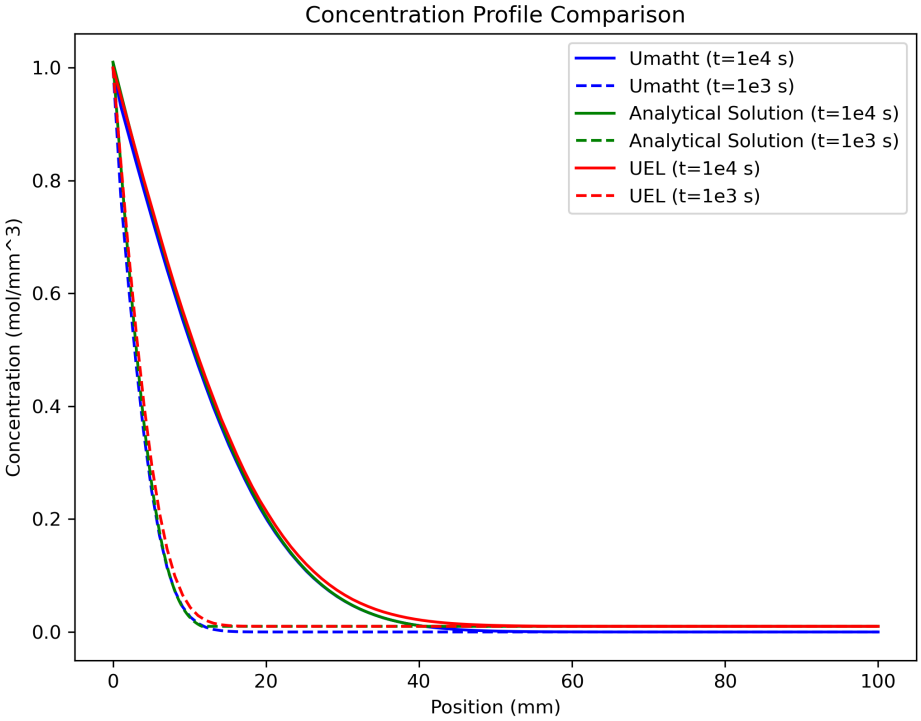


Figure 4.3: Concentration distribution along a bar with different approaches.

The comparison confirms that both subroutines effectively capture the diffusion process and can replicate analytical results with high precision.

4.3.1.2 Single Edge Notch Simulation

As the local balance given in 4.73 and 4.74 dictates, the distribution of hydrogen is driven by volumetric strain. Theoretical models and experimental studies [67, 68, 69] suggest that hydrogen accumulation at the crack tip contributes to the weakening of the material, enhancing crack propagation.

In this study, a blunt crack geometry is utilized to simulate hydrogen transport near a crack tip. The geometry and boundary conditions, shown in Figure 4.4, reflect a symmetrical blunting crack with an applied stress intensity factor (K_I). The equations provided describe the displacement fields(u_x and u_y) in the vicinity of the crack tip based on linear elastic fracture mechanics. This setup effectively captures the coupled mechanical and diffusion behaviors, enabling a detailed examination of hydrogen transport driven by volumetric strain.

$$\begin{cases} u_x(R,\theta) = \dfrac{K_I}{2\mu}\sqrt{\dfrac{R}{2\pi}}\cos\left(\dfrac{\theta}{2}\right)\left[2-4\nu+2\sin^2\left(\dfrac{\theta}{2}\right)\right] \\ u_y(R,\theta) = \dfrac{K_I}{2\mu}\sqrt{\dfrac{R}{2\pi}}\sin\left(\dfrac{\theta}{2}\right)\left[4-4\nu-2\cos^2\left(\dfrac{\theta}{2}\right)\right] \end{cases} \tag{4.80}$$

These displacement fields define the crack-tip asymptotics under mode I loading and are used to prescribe boundary conditions in the simulation. The corresponding material parameters employed in the analysis are listed in the table.

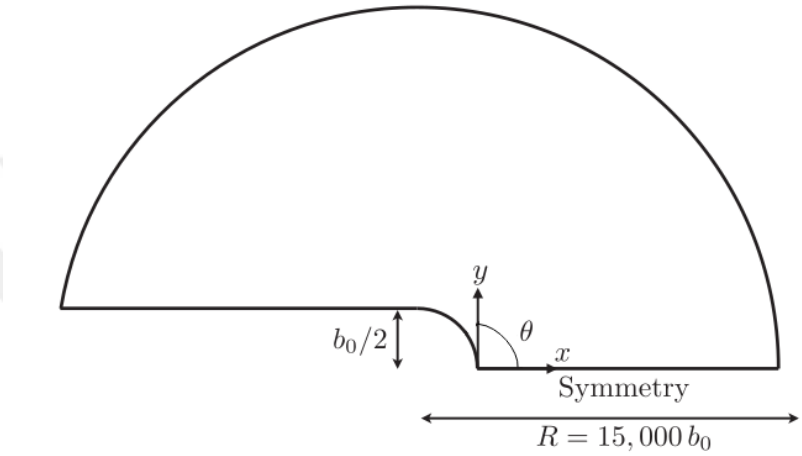
Table 4.1: Material properties for the SEN specimen

E	ν	Y_0	n	D_L	N_L	θ
207 GPa	0.3	250 MPa	0.2	1.27×10^{-8} m^2/s	8.47×10^5 mol/m^2	300K

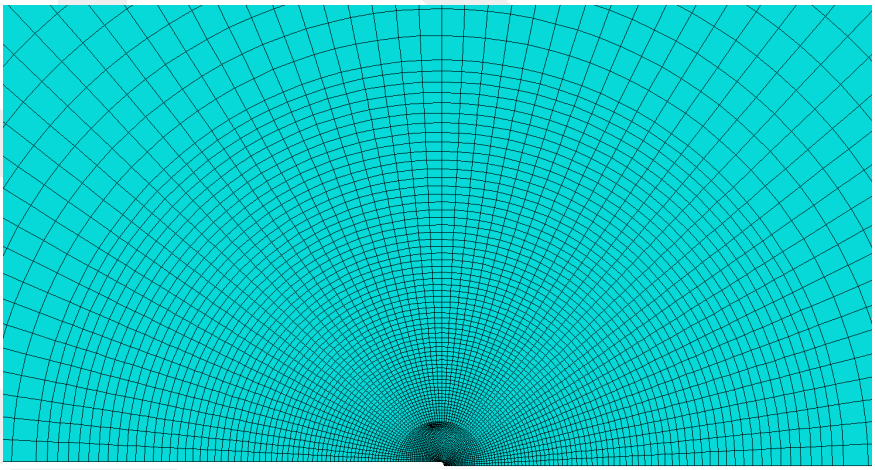
The mechanical response of the material is characterized using a power-law hardening model, which relates the equivalent stress Y to the equivalent plastic strain $\bar{\epsilon}^p$. In this formulation, Y_0 is the initial yield stress, n is the hardening exponent, and $\epsilon_0 = Y_0/E$ is a reference strain based on Young's modulus E. The relation is given as follows:

$$Y = Y_0\left(1+\frac{\overline{\epsilon}^p}{\epsilon_0}\right)^n, \qquad \epsilon_0 = \frac{Y_0}{E} \tag{4.81}$$

Figure 4.4 illustrates the crack geometry and mesh used in the simulation. The domain incorporates a semicircular blunt notch with a characteristic opening displacement b_0, and exploits symmetry to minimize computational cost. A refined mesh is employed around the crack tip to ensure accurate resolution of the stress and hydrogen concentration gradients.



(a)

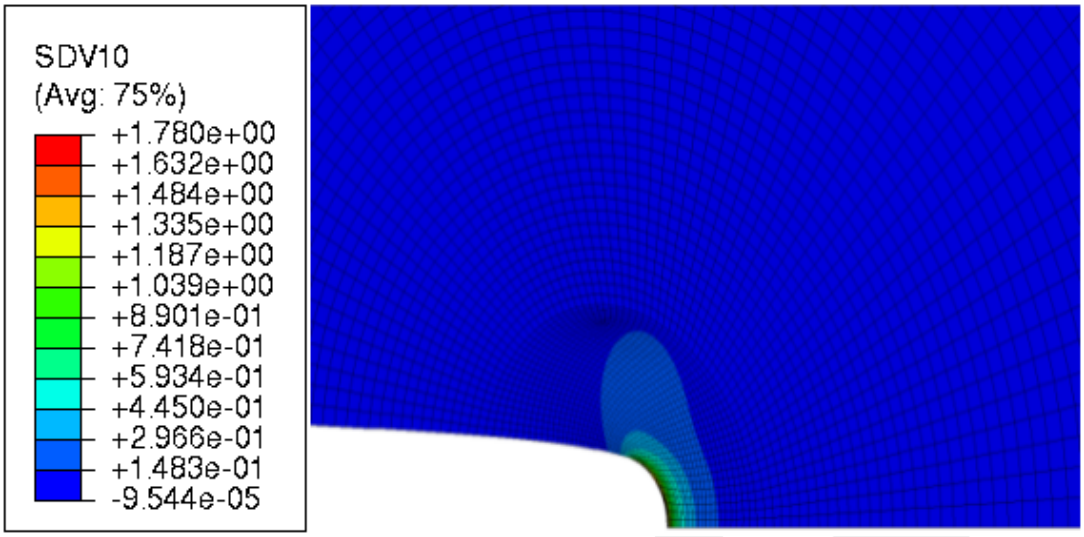


(b)

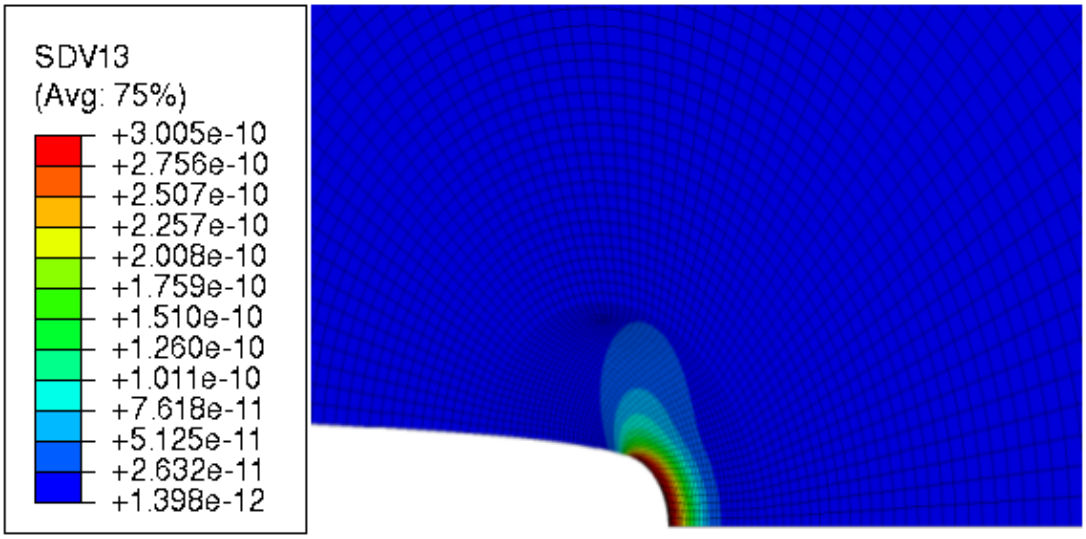
Figure 4.4: (a) Schematic of the blunt-crack geometry and boundary conditions, (b) Mesh around crack tip.

Following the defined boundary conditions and refined mesh near the crack tip, the results of the coupled mechanical-diffusion simulation are presented. Figure 4.5 shows the equivalent plastic strain and the corresponding trapped hydrogen concentration fields. As expected, the plastic deformation localizes around the crack tip, creating favorable trapping sites for hydrogen, which accumulates in regions of high plastic strain.

To further elucidate the driving mechanisms of hydrogen diffusion, Figure 4.6 illustrates the volumetric strain and lattice hydrogen concentration. The volumetric strain field, shown in Figure 4.6(a), peaks near the crack tip and provides a thermodynamic driving force for hydrogen migration. The corresponding lattice hydrogen concentration in Figure 4.6(b) exhibits a distribution pattern that aligns with the strain-induced gradients, confirming the coupling between mechanical fields and hydrogen transport phenomena.

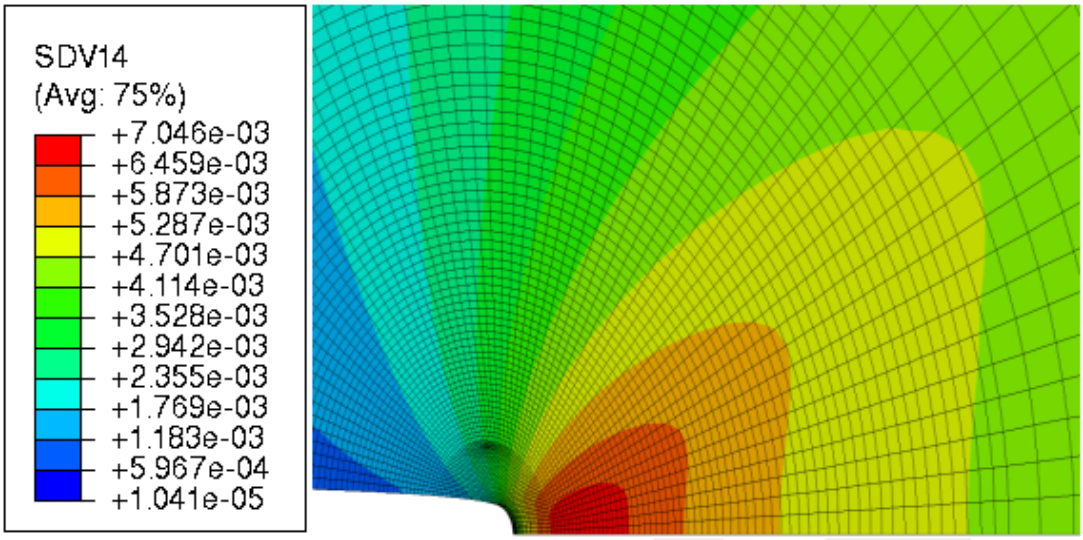


(a)

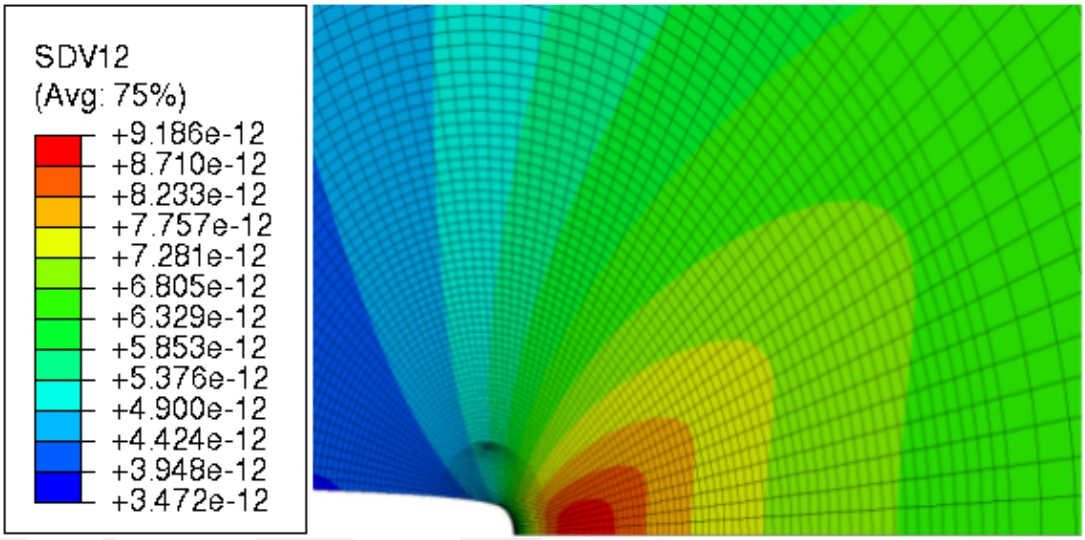


(b)

Figure 4.5: (a) Equivalent plastic strain. (b) Trapped hydrogen concentration.

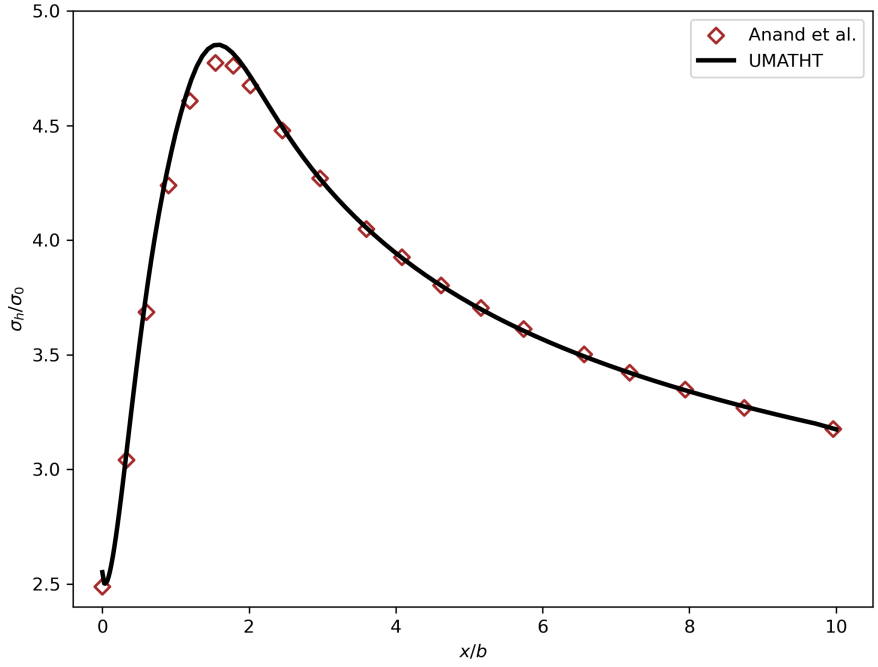


(a)

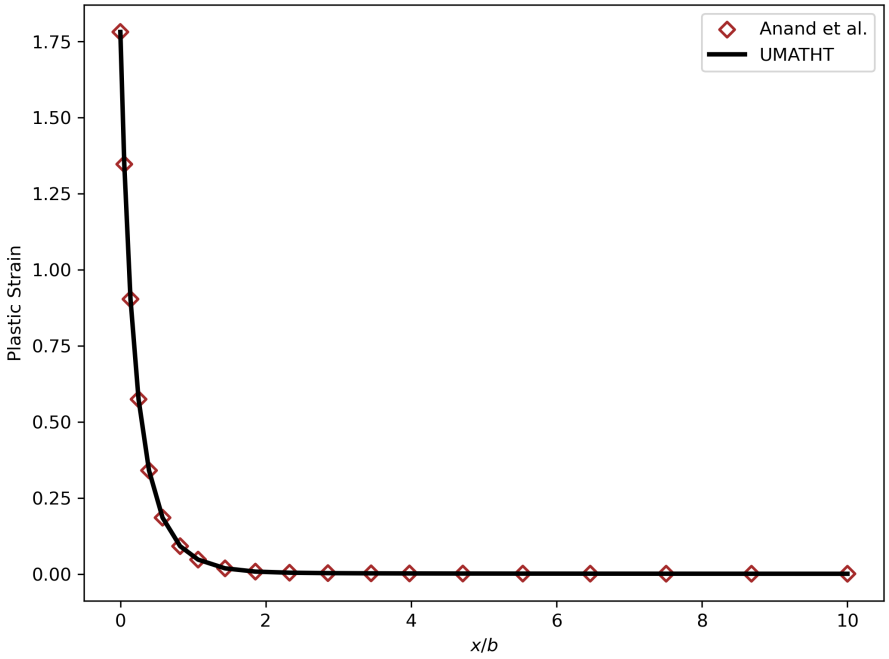


(b)

Figure 4.6: a) Volumetric strain. (b) Lattice hydrogen concentration.

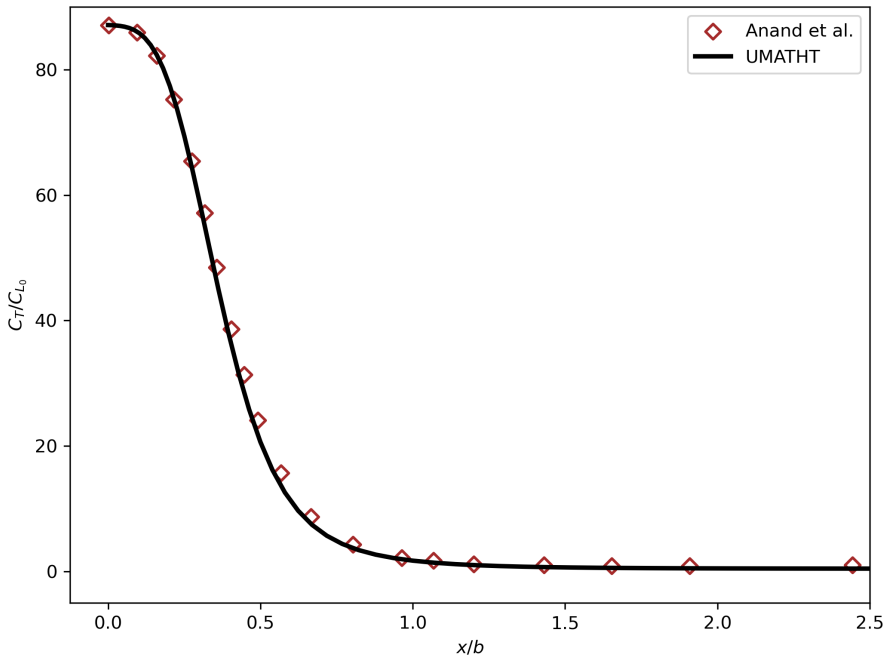


(a)

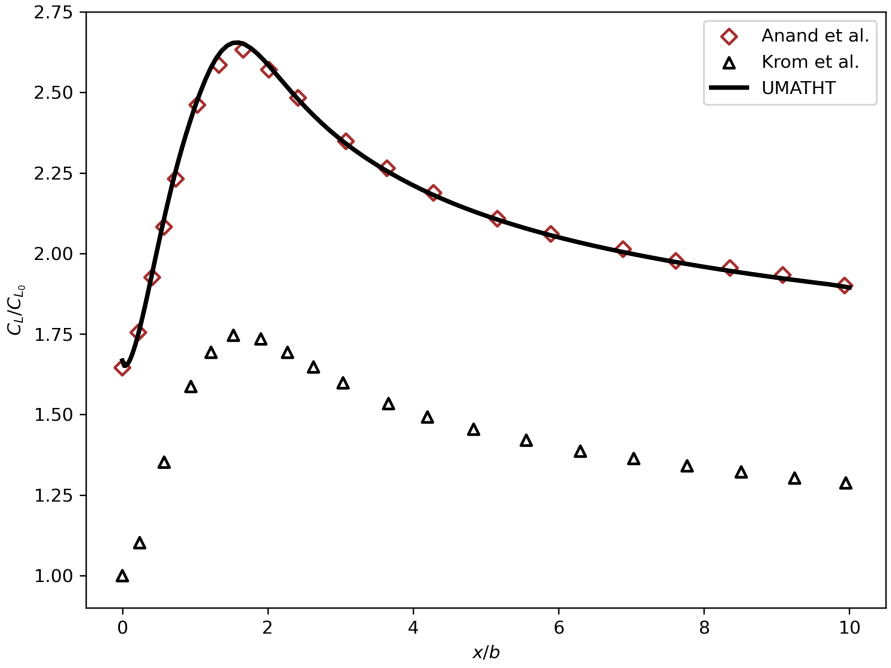


(b)

Figure 4.7: (a) Normalized hydrostatic stress ahead of crack tip, (b) Equivalent tensile plastic strain ahead of crack tip.



(a)



(b)

Figure 4.8: (a) Normalized trapped concentration, (b) Normalized lattice concentration ahead of crack tip.

To validate the mechanical response of the implementation, Figure 4.7 compares the normalized hydrostatic stress and equivalent plastic strain profiles ahead of the crack tip with the reference solution from Anand et al. [61]. The excellent agreement confirms the accuracy of our UMATHT-based model in capturing the stress field under small-scale yielding conditions. Furthermore, Figure 4.8 presents normalized trapped and lattice hydrogen concentrations compared against the results of Anand et al. [61] and Krom et al. [60]. Our simulations accurately reproduce the steep gradients and peak values near the crack tip, confirming both the mechanical-diffusion coupling and the role of hydrostatic stress in enhancing lattice hydrogen content. Notably, differences in boundary conditions explain the shift in lattice concentration profiles, consistent with theoretical expectations derived from the chemical potential formulation in Eq. 4.60.

These results collectively demonstrate that the finite element framework reliably captures the essential features of hydrogen transport under mechanical loading within the context of J2 plasticity. In the following section, the investigation is extended to a more physically detailed representation of deformation behavior using a crystal plasticity-based formulation, enabling the exploration of anisotropic effects and grain-level hydrogen localization.

4.3.2 Crystal Plasticity-Based Modeling and Simulations

4.3.2.1 Single Edge Notch with Crystallographic Anisotropy

To better understand the impact of material anisotropy on hydrogen-assisted deformation, crystal plasticity simulations are utilized and compared with results obtained using isotropic J2 plasticity. While J2 plasticity captures the average yield behavior, it does not account for direction-dependent slip activity and its influence on strain localization and hydrogen accumulation.

Figure 4.9 shows the equivalent plastic strain distribution from the J2 model, which exhibits a symmetric plastic zone typical of isotropic yielding. In contrast, Figures 4.10 through 4.12 illustrate simulations with crystal plasticity under different crystallographic orientations. The case in Figure 4.10 corresponds to a grain with local orientation close to [001]-[010], leading to pronounced directional plastic strain bands and focused hydrogen trapping near the slip-active directions. Figure 4.11 and 4.12 highlight additional cases with orientations [001]-[110] and [100]-[0$\bar{1}$1], respectively, demonstrating how slip system activation leads to distinct plasticity and hydrogen localization patterns.

These results clearly illustrate the role of crystallographic anisotropy in controlling both deformation paths and hydrogen redistribution. Unlike the isotropic response, the CP model captures asymmetric strain fields, localized shear bands, and orientation-specific trapping behavior — phenomena that are critical to understanding intergranular or facet-driven hydrogen embrittlement mechanisms.

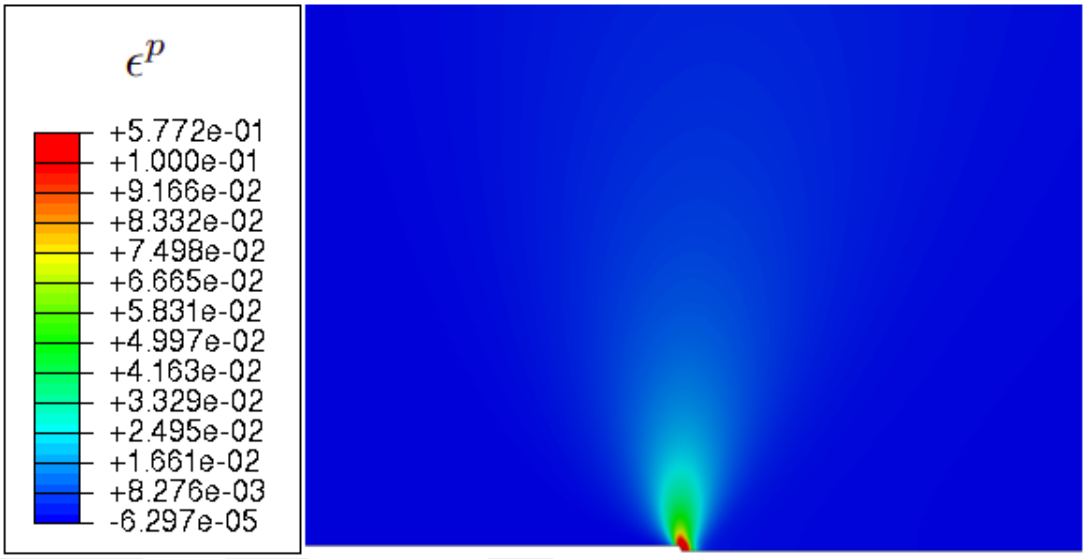
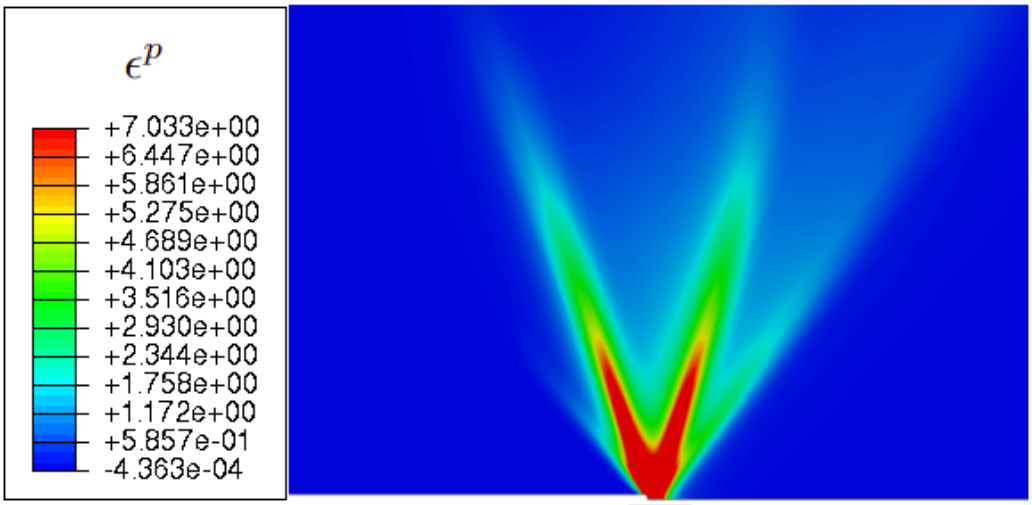
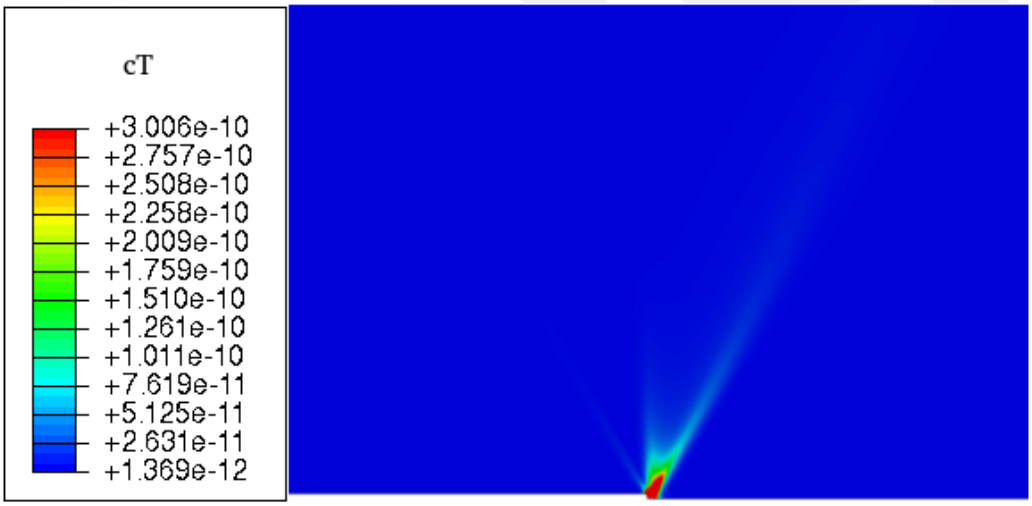


Figure 4.9: Equivalent plastic strain

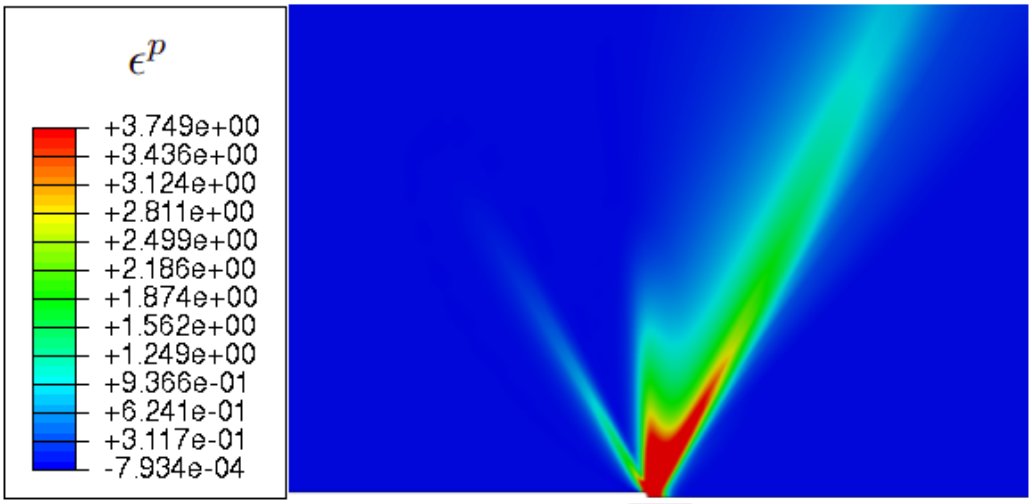


(a)

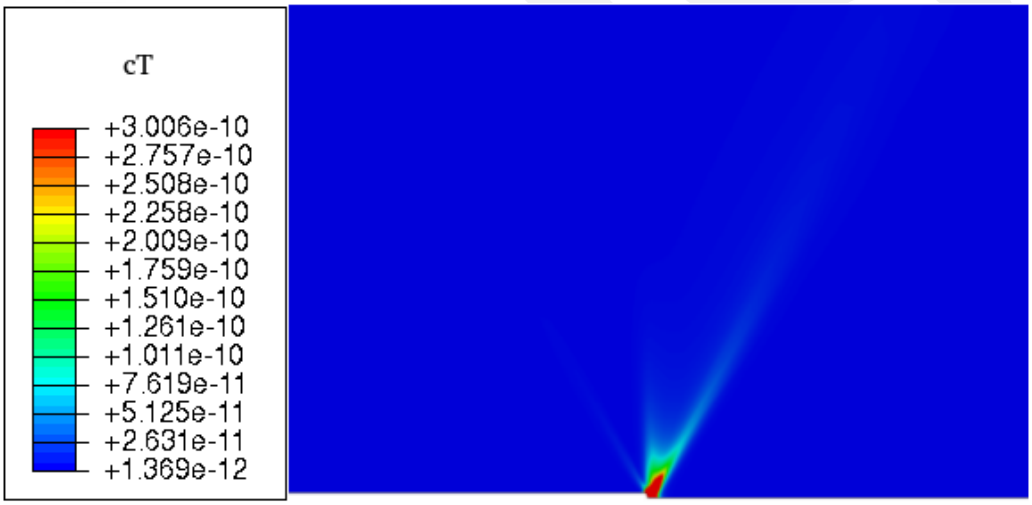


(b)

Figure 4.10: (a) Equivalent plastic strain. (b) Trapped hydrogen concentration.

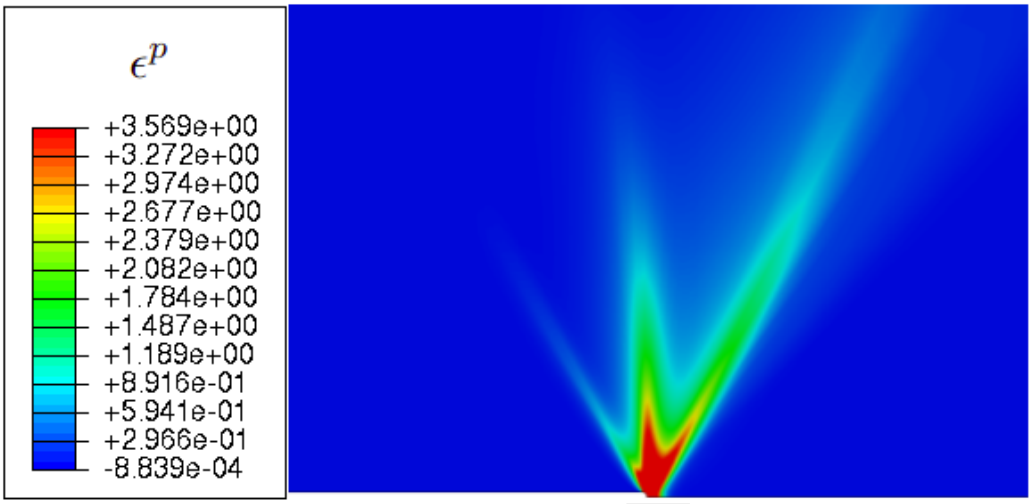


(a)

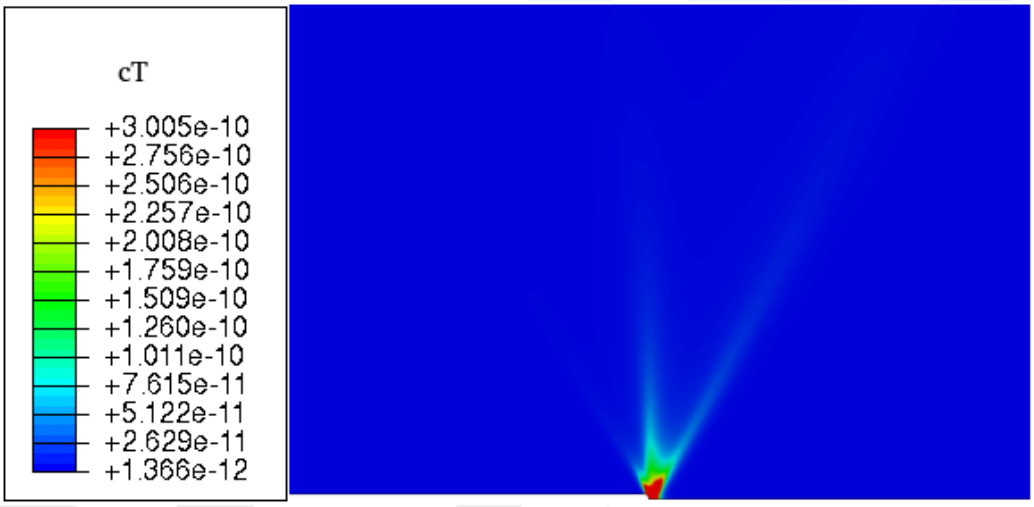


(b)

Figure 4.11: (a) Equivalent plastic strain. (b) Trapped hydrogen concentration.



(a)



(b)

Figure 4.12: (a) Equivalent plastic strain. (b) Trapped hydrogen concentration.

4.3.2.2 Polycrystalline Tensile Test

4.3.3 Polycrystalline Tensile Test

To investigate the grain-level effects of crystallographic orientation on hydrogen accumulation, a virtual polycrystal geometry was constructed with randomly assigned grain orientations centered around the [001] axis, as shown in Figure 4.13. The boundary conditions depicted in Figure 4.14 apply uniaxial tensile loading in the horizontal direction, simulating a mechanically driven hydrogen ingress scenario. This setup allows us to examine how heterogeneous plasticity and stress concentrations at grain boundaries affect hydrogen transport and localization.

Figure 4.15 presents the von Mises stress distribution and the corresponding lattice hydrogen concentration. As expected, the stress field exhibits significant heterogeneity due to anisotropic plastic deformation across grains, which in turn drives non-uniform hydrogen transport. High-stress regions, particularly near triple junctions or sharp orientation mismatches, serve as zones of elevated lattice concentration.

Figure 4.16 shows the equivalent plastic strain and trapped hydrogen concentration. The plastic strain bands are highly localized along grain boundaries and slip paths aligned with the active crystallographic systems. These regions also show enhanced hydrogen trapping, confirming the strong coupling between plastic deformation and hydrogen retention. Notably, the peak trapping zones align with prior high-strain regions, indicating that dislocation-based trap density dominates over hydrostatic stress in determining hydrogen retention in the polycrystalline regime.

These observations underscore the importance of modeling at the microscale using crystal plasticity to capture the synergistic interaction between microstructure, deformation, and hydrogen behavior. The influence of grain orientation, plastic strain heterogeneity, and boundary conditions cannot be neglected in realistic predictions of hydrogen embrittlement susceptibility in engineering alloys.

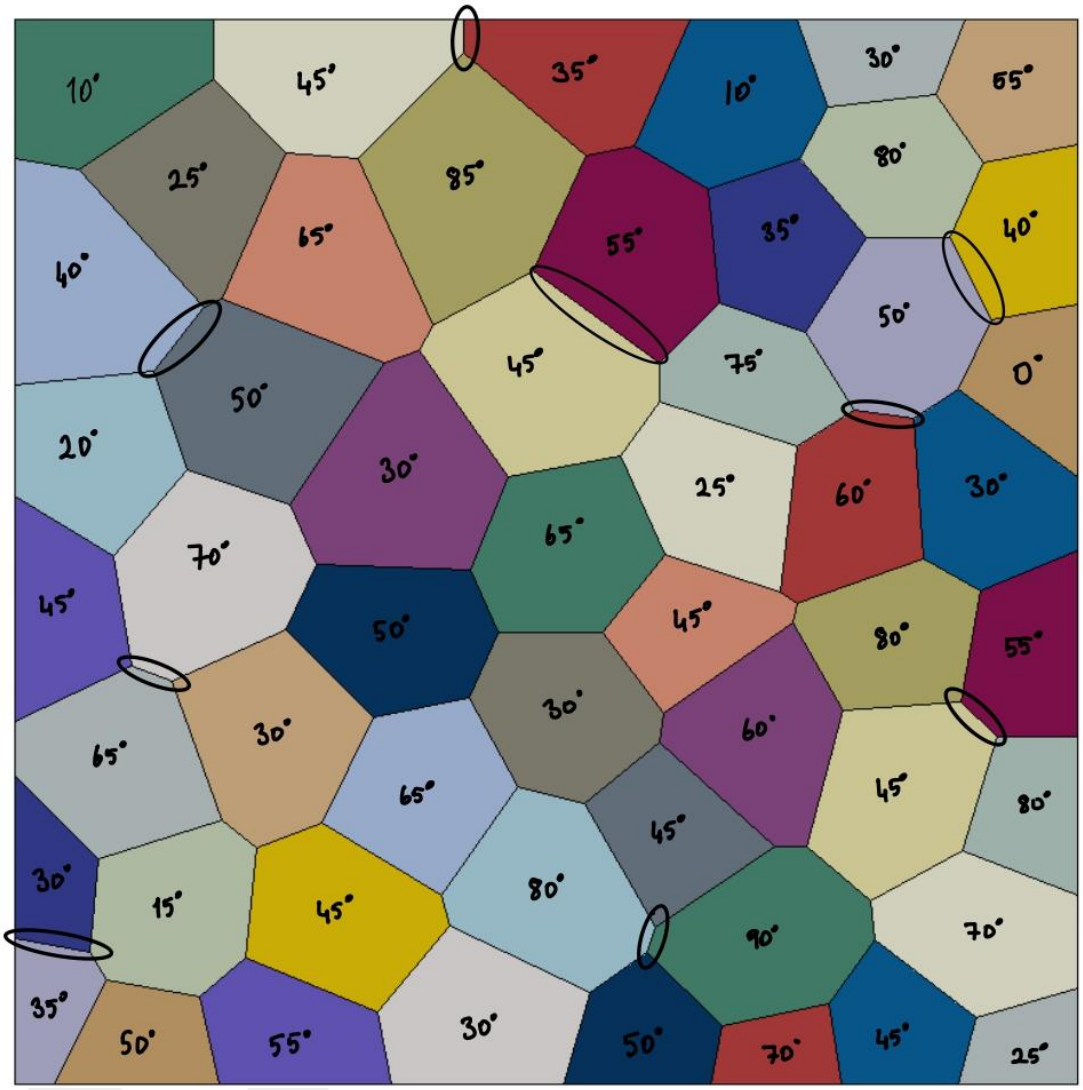


Figure 4.13: Polycrystal contains cells with different orientations.

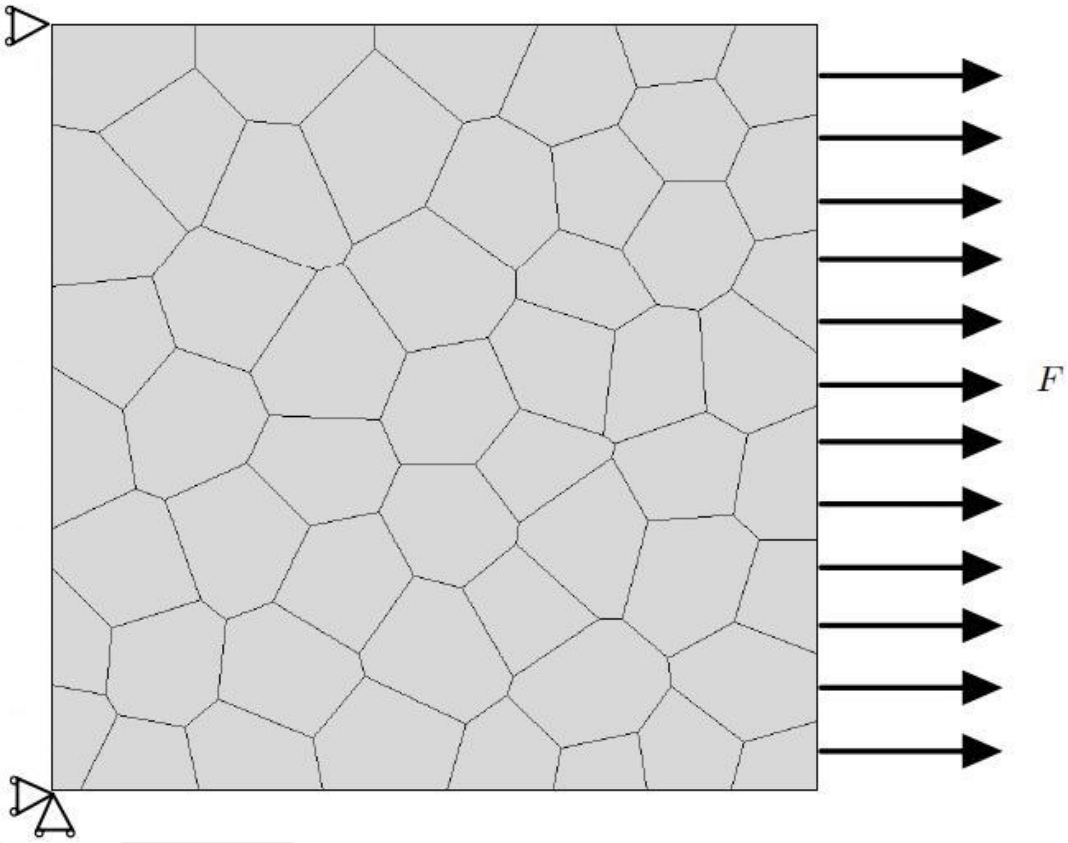
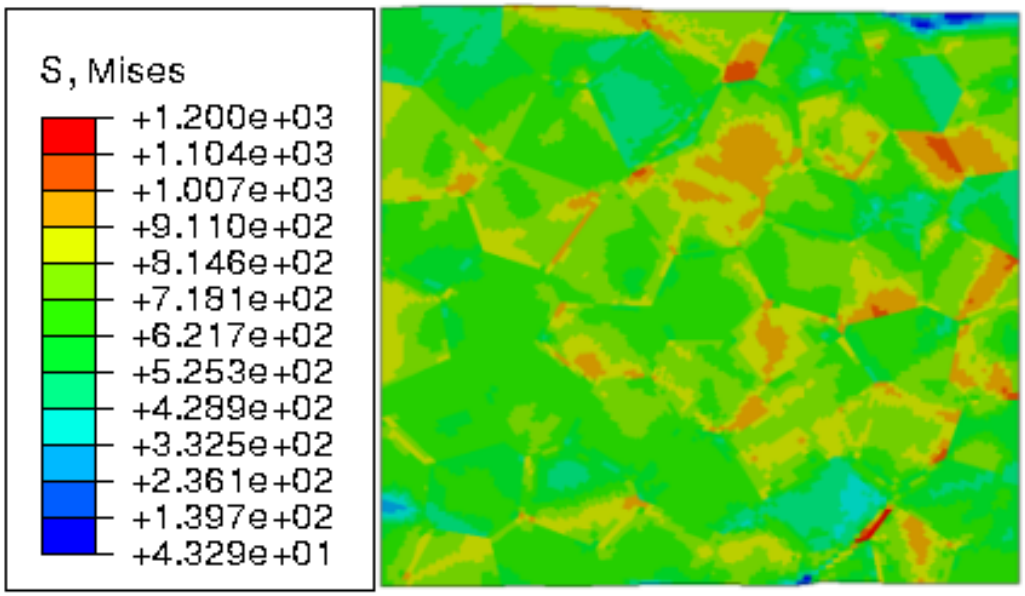
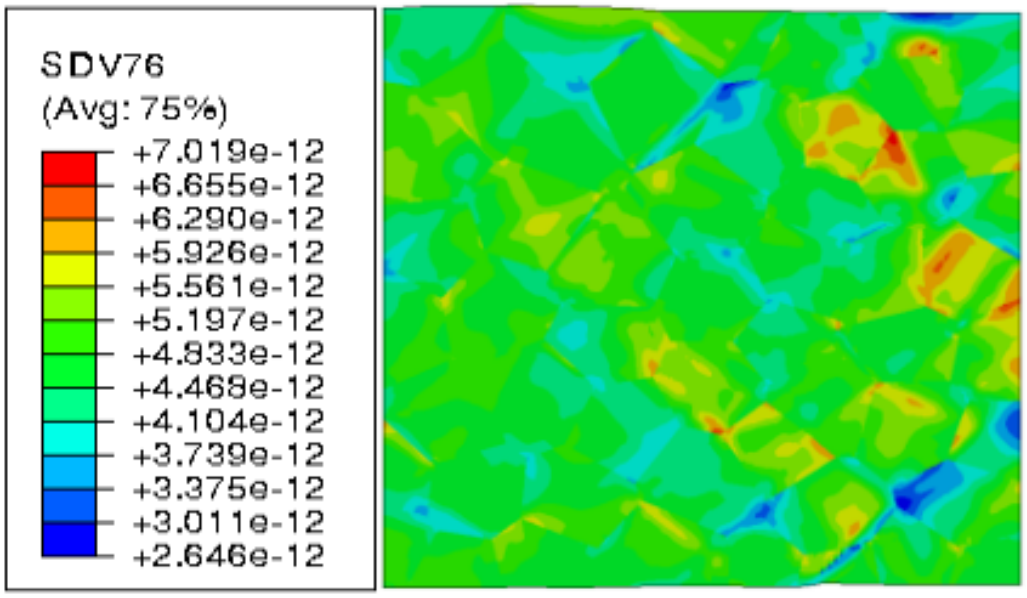


Figure 4.14: Boundary conditions and applied load on the geometry.

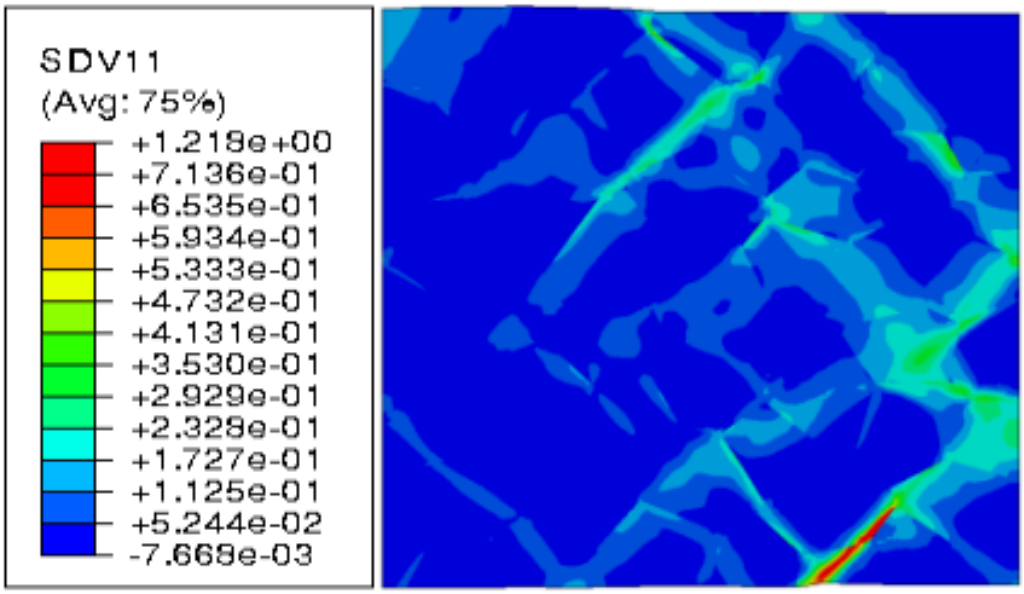


(a)

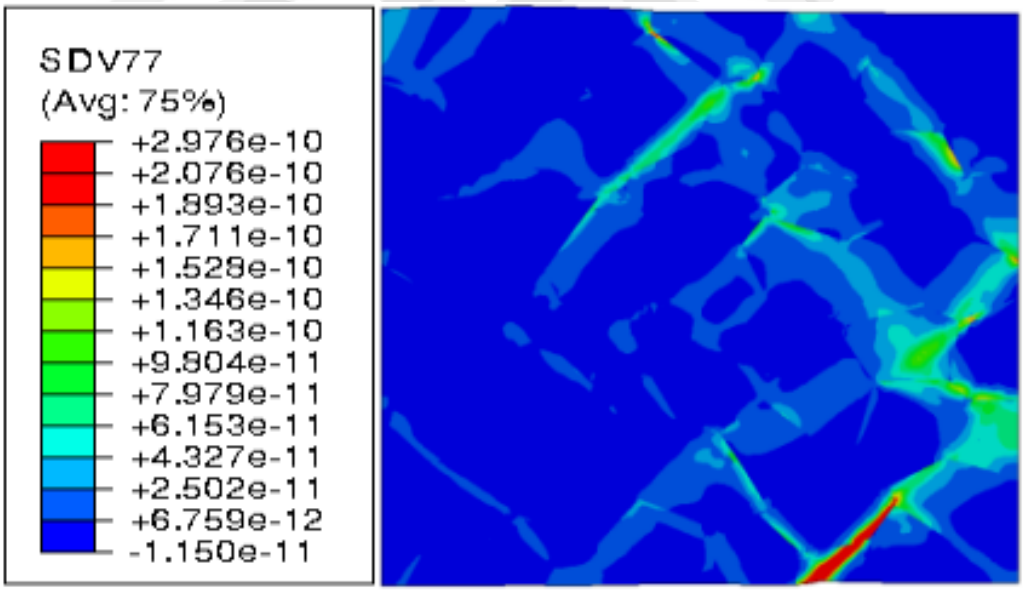


(b)

Figure 4.15: (a) Stress distribution. (b) Lattice hydrogen distribution.



(a)



(b)

Figure 4.16: (a) Equivalent plastic strain. (b) Trapped hydrogen concentration.

4.3.4 Concluding Remarks

The numerical results presented in this chapter systematically demonstrate the critical interplay between mechanical deformation and hydrogen transport in metallic systems. Through a progressive modeling strategy, starting from J2 plasticity and advancing toward full crystal plasticity-based simulations, we have captured the essential mechanisms responsible for hydrogen accumulation, redistribution, and trapping under mechanical loading.

In the initial set of simulations, the use of J2 plasticity enabled a baseline validation of our finite element implementation by reproducing classical crack-tip field behavior and hydrogen transport patterns. These results served not only as verification but also as a conceptual foundation for evaluating hydrogen-enhanced plasticity and the role of hydrostatic stress and volumetric strain in driving lattice diffusion. The comparison with established reference studies, such as those by Anand et al. and Krom et al., confirmed the fidelity of our numerical framework in capturing both mechanical and transport phenomena.

The subsequent incorporation of crystal plasticity introduced a microstructural perspective by accounting for crystallographic anisotropy, slip system activity, and orientation dependent deformation behavior. Through a series of single-crystal and polycrystalline simulations, we demonstrated how grain orientation and boundary architecture significantly influence local stress, strain, and hydrogen concentration fields. These simulations revealed highly localized plastic strain bands and hydrogen trapping paths, often aligned with slip directions and concentrated near grain boundaries. Such heterogeneity, which is inaccessible through isotropic models, is crucial for explaining experimentally observed crack initiation sites and failure modes in hydrogen-embrittled materials.

Overall, the results in this chapter underscore the importance of coupling advanced constitutive modeling with hydrogen transport analysis. Accurate prediction of embrittlement susceptibility requires models that incorporate both the thermodynamic driving forces and the microstructural pathways that govern hydrogen ingress and localization. The methodologies presented here lay the groundwork for future studies involving fatigue, grain boundary character, and three-dimensional microstructures, all of which are essential for developing more resistant material systems.

In the following chapter, we build upon this understanding of hydrogen-assisted degradation by introducing a phase-field fracture modeling framework. This method provides a powerful tool for simulating crack nucleation and propagation in a diffuse, energetically consistent manner. By coupling the phase-field approach with the mechanical and diffusion fields explored thus far, we aim to capture the full evolution of failure, from hydrogen accumulation to final fracture, in a unified computational setting.

CHAPTER 5

PHASE FIELD MODELING OF FRACTURE

Having established the experimental observations and simulation results concerning hydrogen embrittlement in metals, the focus of this thesis now transitions to the computational modeling of fracture phenomena using the phase-field approach. This chapter aims to provide a comprehensive framework for phase-field modeling of fracture, establishing the theoretical background, numerical implementation, and application to relevant material systems.

5.1 Introduction

The modeling of fracture in engineering materials remains a challenging problem due to the inherently multi-scale and nonlocal nature of crack initiation and propagation. Classical approaches, while successful in certain regimes, are often limited when dealing with complex crack topologies or coupling with other physical phenomena. In recent years, phase-field models have emerged as a powerful and versatile tool for simulating brittle and ductile fracture within a unified variational framework.c

Nickel-based single crystal superalloys are widely utilized in high-performance engineering applications due to their superior mechanical properties [70]. However, their anisotropic nature presents unique challenges for modeling fracture, as crack initiation and propagation are highly orientation-dependent [17]. In FCC single crystals, cracks tend to evolve along preferential crystallographic planes—most notably the {111} planes—necessitating advanced models that capture both elastic and plastic anisotropy.

Traditional fracture theories, such as Linear Elastic Fracture Mechanics (LEFM) pioneered by Griffith [71], are limited in their ability to simulate complex crack phenomena such as branching, curving, or spontaneous nucleation. Variational approaches, notably the Francfort–Marigo model and its regularization via phase-field methods, have emerged as powerful alternatives, allowing crack initiation and evolution to be formulated as an energy minimization problem without predefining crack paths [72, 73].

The phase-field method replaces sharp crack discontinuities with a continuous scalar field that smoothly transitions between intact and fully broken states, thus facilitating the simulation of arbitrary crack topologies in complex geometries and in the presence of multiple interacting physical mechanisms [74, 75]. For brittle fracture, the crack surface is regularized by a phase-field functional, and the evolution of the field is governed by energy minimization principles [72, 73, 74].

Recent developments have demonstrated the effectiveness of coupling phase-field fracture with hydrogen diffusion to model hydrogen-assisted cracking. Martínez-Pañeda et al. [59] proposed a thermodynamically consistent framework where the critical energy release rate is degraded based on local hydrogen concentration, using first-principles informed damage coefficients. Their formulation integrates stress-assisted diffusion, a hydrogen-sensitive degradation function, and a staggered finite element solution scheme, offering accurate predictions of environmentally assisted failure in metals.

However, in metals especially in single crystals, fracture is often preceded or accompanied by significant plastic deformation, making it essential to couple the fracture process with plasticity. Early variational models focused on brittle fracture, but recent advances have extended phase-field approaches to ductile fracture by incorporating plastic work and accumulated plastic strain as additional crack-driving forces [75, 76, 77, 78]. Key improvements include:

- Splitting the energy into tensile and compressive parts to avoid crack propagation under compression [74].
- Degrading both the elastic modulus and the yield surface as the phase-field variable evolves, ensuring thermodynamic consistency during elasto-plastic deformation and damage evolution [77].
- Introducing rate effects and fatigue by making fracture toughness or crack-driving energy dependent on plastic strain rate or accumulated fatigue damage, thus enabling the simulation of time-dependent phenomena under cyclic or high-rate loading [70, 79, 80].

In the context of single crystal plasticity, phase-field approaches can be further extended to incorporate crystallographic anisotropy by linking the phase-field evolution to slip system activity and orientation [81, 82]. Traditional discrete approaches, such as the cohesive zone model (CZM) or XFEM, are often limited by the need for predefined crack paths or complex remeshing, and struggle to simulate spontaneous initiation and branching, especially in anisotropic crystals [83, 84].

Various damage models have been developed for crystals. For example, Ekh et al. [85] linked damage to slip systems, Dunne et al. [86] used isotropic damage within a crystal plasticity framework, and Aslan et al. [87] formulated a micromorphic approach with separate damage components for cleavage and shear. However, challenges remain regarding the proper definition of crack-driving forces in the presence of plasticity, the treatment of cyclic loading, and the consistent prediction of crack paths in anisotropic, single-crystal materials.

This work aims to develop and implement a numerical model that couples phase-field fracture with crystal plasticity to simulate fatigue crack growth in FCC single crystals. Martínez-Pañeda et al. [88] demonstrated that incorporating hydrogen diffusion and trap occupancy effects into a fatigue phase-field formulation enables accurate prediction of environmentally assisted crack growth rates, offering strong validation against experimental data in steels. Their work demonstrated that incorporating hydrogen diffusion and trap occupancy effects into a fatigue phase-field formulation enables accurate prediction of environmentally assisted crack growth rates, offering strong validation against experimental data in steels. The model focuses on energy storage and dissipation during crack evolution, as well as the resulting directionality and morphology of cracks, and is implemented in ABAQUS via UMAT and UMATHT subroutines.

5.2 Theoretical Background

In classical fracture mechanics, cracks are represented as sharp discontinuities, making their evolution difficult to track—especially for arbitrary and branching crack paths. The scalar-valued phase field variable

$$d(x) = e^{-\frac{|x|}{l}} \tag{5.1}$$

provides an illustrative profile for the transition between undamaged ($d = 0$) and fully damaged ($d = 1$) states, across a finite width governed by the internal length scale parameter l.

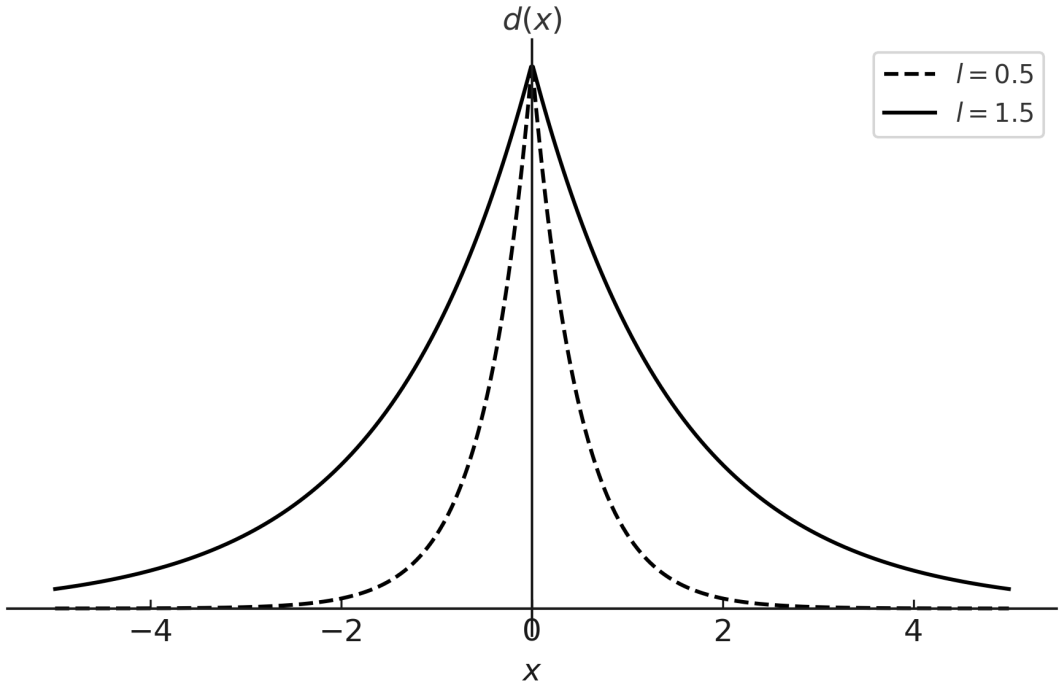


Figure 5.1: Phase field variable with different length parameter.

To incorporate this transition into a variational framework suitable for numerical simulations, the crack is regularized by introducing a smooth functional that approximates the sharp crack topology. This leads to the definition of the regularized crack surface energy:

$$\Gamma_l(d) = \int_{B_0} \gamma_l(d, \nabla d)\, dV, \qquad \gamma_l(d, \nabla d) = \frac{1}{2l}\left[d^2 + l^2 |\nabla d|^2\right] \tag{5.2}$$

where γ_l is the crack surface density function per unit volume. This formulation ensures a smooth transition and enables the modeling of complex crack patterns within a diffuse interface approach [72, 73, 74, 76].

5.2.1 Variational Formulation of Regularized Fracture

The total energy of a cracked elastic body, in the regularized setting, is given by

$$\mathcal{E}(u, d) = \int_{B_0} g(d)\, \psi(\varepsilon(u))\, dV + G_c\, \Gamma_l(d) \tag{5.3}$$

where u is the displacement field, $\psi(\varepsilon(u))$ is the elastic strain energy density, $g(d)$ is the degradation function (e.g., $g(d) = (1 - d)^2$), and G_c is the critical energy release rate.

Remark: The parameter k in the degradation function $g(d) = (1-d)^2 + k$ is usually omitted in theoretical derivations, but is always included in computations (with $k \ll 1$) to prevent numerical ill-conditioning as $d \to 1$.

5.2.1.1 Elastic Energy Contribution at Finite Strain

In the finite-strain setting, the elastic response is formulated in terms of an elastic strain measure $\boldsymbol{\varepsilon}^e$, obtained via the multiplicative decomposition of the deformation gradient:

$$\mathbf{F} = \mathbf{F}^e \mathbf{F}^p \tag{5.4}$$

The elastic strain $\boldsymbol{\varepsilon}^e$ is typically taken as the logarithmic (Hencky) strain:

$$\boldsymbol{\varepsilon}^e = \frac{1}{2} \ln \mathbf{C}^e \tag{5.5}$$

where $\mathbf{C}^e = \mathbf{F}^{eT} \mathbf{F}^e$ is the elastic right Cauchy-Green tensor.

The undamaged stored elastic energy per unit reference volume is:

$$\psi_0(\boldsymbol{\varepsilon}^e) = \frac{1}{2} \boldsymbol{\varepsilon}^e : \mathbb{C} : \boldsymbol{\varepsilon}^e \tag{5.6}$$

where $\mathbb{C}$ is the fourth-order elasticity tensor, which may be isotropic or anisotropic depending on the crystal symmetry.

Damage is incorporated through the degradation function $g(d)$:

$$\psi_e(\boldsymbol{\varepsilon}^e, d) = g(d) \psi_0(\boldsymbol{\varepsilon}^e) \tag{5.7}$$

To avoid non-physical crack growth in compression, the elastic energy is split into tensile and compressive parts using the spectral decomposition of the elastic strain [74, 89]:

$$\psi_e(\boldsymbol{\varepsilon}^e, d) = g(d)\, \psi_e^+(\boldsymbol{\varepsilon}^e) + \psi_e^-(\boldsymbol{\varepsilon}^e) \tag{5.8}$$

where

$$\psi_e^\pm(\boldsymbol{\varepsilon}^e) = \frac{1}{2} (\boldsymbol{\varepsilon}^e)^\pm : \mathbb{C} : (\boldsymbol{\varepsilon}^e)^\pm \tag{5.9}$$

The positive and negative parts of the elastic strain tensor are defined as:

$$(\boldsymbol{\varepsilon}^e)^{\pm} = \sum_{i=1}^{3} \langle \varepsilon_i^e \rangle_{\pm} \, \mathbf{n}_i \otimes \mathbf{n}_i \tag{5.10}$$

where ε_i^e are the principal values (eigenvalues) and $\mathbf{n}_i$ are the corresponding normalized eigenvectors of $\boldsymbol{\varepsilon}^e$. The ramp functions are defined as $\langle x \rangle_+ = \max(x, 0)$ and $\langle x \rangle_- = \min(x, 0)$ (or equivalently, $\langle x \rangle_{\pm} = \frac{1}{2}(x \pm |x|)$).

This spectral split ensures that only the tensile part of the energy is degraded by the phase-field variable, preventing cracks from forming or propagating in regions dominated by compressive loading—a key physical requirement for brittle fracture at large strains [74, 76, 89].

5.2.1.2 Plastic Dissipation at Finite Strain: J2 Plasticity with Linear Isotropic Hardening

For isotropic ductile metals, plastic deformation at finite strain is described by the multiplicative decomposition of the deformation gradient,

$$\mathbf{F} = \mathbf{F}^e \mathbf{F}^p \tag{5.11}$$

where $\mathbf{F}^p$ is the plastic part and $\mathbf{F}^e$ is the elastic part.

The yield condition is formulated in terms of the Kirchhoff stress $\boldsymbol{\tau}$ and its deviatoric part $\boldsymbol{s}$ as

$$f(\boldsymbol{\tau}, \bar{\varepsilon}^p) = \sqrt{\frac{3}{2}\boldsymbol{s} : \boldsymbol{s}} - \left(\sigma_{y,0} + H\bar{\varepsilon}^p\right) \leq 0 \tag{5.12}$$

where $\sigma_{y,0}$ is the initial yield strength, H is the linear isotropic hardening modulus, and $\bar{\varepsilon}^p$ is the accumulated equivalent plastic strain.

Plastic flow is governed by an associative flow rule, which takes the form

$$\dot{\mathbf{F}}^p \mathbf{F}^{p^{-1}} = \dot{\gamma}\, \mathbf{N}, \qquad \mathbf{N} = \frac{\boldsymbol{s}}{\|\boldsymbol{s}\|} \tag{5.13}$$

where $\dot{\gamma}$ is the plastic multiplier determined by the consistency condition. The equivalent plastic strain evolves according to

$$\dot{\bar{\varepsilon}}^p = \sqrt{\frac{2}{3}\dot{\boldsymbol{\varepsilon}}^p : \dot{\boldsymbol{\varepsilon}}^p} = \dot{\gamma}, \tag{5.14}$$

with initial condition $\bar{\varepsilon}^p(0) = 0$.

The instantaneous rate of plastic dissipation per unit reference volume is given by

$$\dot{\psi}_{\mathrm{p}} = \boldsymbol{\tau} : \dot{\boldsymbol{\varepsilon}}^p = \left(\sigma_{y,0} + H\bar{\varepsilon}^p\right)\dot{\bar{\varepsilon}}^p \tag{5.15}$$

so that the total accumulated plastic dissipation up to time t is

$$\psi_{\mathrm{p}} = \int_0^t \left(\sigma_{y,0} + H\bar{\varepsilon}^p\right)\dot{\bar{\varepsilon}}^p \, dt \tag{5.16}$$

To ensure a consistent degradation of the load-carrying capacity as fracture damage evolves, the yield strength and hardening modulus can be degraded by the phase-field variable, so that

$$\sigma_{y,0} \to g(d)\,\sigma_{y,0}, \qquad H \to g(d)\,H \tag{5.17}$$

where $g(d)$ is the degradation function used in the elastic energy.

With these definitions, the total phase-field energy functional including the plastic dissipation becomes

$$\mathcal{E}(u, d, \bar{\varepsilon}^p) = \int_{B_0} \left[g(d)\,\psi_0^+(\boldsymbol{\varepsilon}^e) + \psi_0^-(\boldsymbol{\varepsilon}^e) + g(d)\psi_{\mathrm{p}}(\bar{\varepsilon}^p)\right] dV + G_c\Gamma_l(d) \tag{5.18}$$

where $\psi_0^{\pm}$ are the tensile and compressive parts of the elastic energy from the spectral split, and ψ_{pl} is the cumulative plastic dissipation.

This formulation allows the direct coupling of finite-strain J2 plasticity with linear isotropic hardening into the variational phase-field framework, providing a consistent description of ductile fracture in isotropic metals.

5.2.1.3 Work Density of Fracture and Total Energy Functional

The regularized fracture work density in the phase-field framework is given by

$$\psi_{\text{frac}}(d, \nabla d) = \frac{G_c}{2l} d^2 + \frac{G_c l}{2} |\nabla d|^2 \tag{5.19}$$

where G_c is the critical energy release rate, and l is the phase-field length scale.

To account for hydrogen-assisted fracture, the critical energy release rate G_c can be modeled as a function of the local hydrogen concentration c. Following literature approaches [70, 80], we adopt a linear degradation model of the form

$$\mathcal{G}_c(c) = \mathcal{G}_0 \left(1 - \eta \frac{c}{c_{\text{sat}}}\right) \tag{5.20}$$

where $\mathcal{G}_0$ is the fracture toughness in the absence of hydrogen, c_{sat} is the saturation concentration, and $\eta \in [0, 1]$ controls the strength of hydrogen embrittlement. This formulation reflects the experimentally observed reduction in fracture resistance with increasing hydrogen content.

Accordingly, the fracture work density becomes

$$\psi_{\text{frac}}(d, \nabla d, c) = \frac{\mathcal{G}_c(c)}{2l} d^2 + \frac{\mathcal{G}_c(c)\, l}{2} |\nabla d|^2 \tag{5.21}$$

This coupling introduces hydrogen embrittlement directly into the variational fracture model, allowing for simulation of crack growth under diffusion-deformation interaction.

The total energy per unit reference volume, accounting for the degraded elastic energy, plastic dissipation, and fracture work density, is then

$$\Psi(\boldsymbol{\varepsilon}^e, d, \bar{\varepsilon}^p, \nabla d) = g(d)\, \psi_0^+(\boldsymbol{\varepsilon}^e) + \psi_0^-(\boldsymbol{\varepsilon}^e) + g(d) \psi_{\text{p}}(\bar{\varepsilon}^p) + \psi_{\text{frac}}(d, \nabla d) \tag{5.22}$$

The total potential energy functional over the reference domain B_0 is thus

$$\mathcal{E}[u, d, \bar{\varepsilon}^p] = \int_{B_0} \left[g(d)\, \psi_0^+(\boldsymbol{\varepsilon}^e) + \psi_0^-(\boldsymbol{\varepsilon}^e) + g(d) \psi_{\text{p}}(\bar{\varepsilon}^p) + \frac{G_c}{2l} d^2 + \frac{G_c l}{2} |\nabla d|^2 \right] dV \tag{5.23}$$

5.2.1.4 Variational Derivation of the Phase-Field Evolution Equation

The phase-field evolution equation is obtained by taking the first variation of the total energy functional $\mathcal{E}$ with respect to d and requiring stationarity (i.e., $\delta\mathcal{E}/\delta d = 0$), subject to irreversibility ($\dot{d} \geq 0$).

Focusing on all terms in $\mathcal{E}$ that explicitly depend on d or ∇d, the variational derivative is computed as:

$$\frac{\delta\mathcal{E}}{\delta d} = \int_{B_0} \left[g'(d)\, \psi_0^+(\boldsymbol{\varepsilon}^e)\, \delta d + g'(d)\psi_{\mathrm{p}}(\bar{\varepsilon}^p) + \frac{G_c}{l} d\, \delta d + G_c l\, \nabla d \cdot \nabla(\delta d) \right] dV = 0 \quad (5.24)$$

where $g'(d) = \frac{d}{dd} g(d) = -2(1-d)$ (neglecting k for clarity, or $g'(d) = -2(1-d)$ if $g(d) = (1-d)^2$).

Applying integration by parts to the gradient term and assuming suitable boundary conditions ($\nabla d \cdot \mathbf{n} = 0$ on ∂B_0),

$$g'(d)\, \psi_0^+(\boldsymbol{\varepsilon}^e) + g'(d)\psi_{\mathrm{p}}(\bar{\varepsilon}^p) + \frac{G_c}{l} d - G_c l\, \Delta d = 0 \quad (5.25)$$

where $\Delta d = \nabla \cdot \nabla d$ is the Laplacian of d.

Substituting $g'(d) = -2(1-d)$, the strong form of the phase-field evolution equation becomes

$$-2(1-d)\, (\psi_0^+(\boldsymbol{\varepsilon}^e) + \psi_{\mathrm{p}}(\bar{\varepsilon}^p)) + \frac{G_c}{l} d - G_c l\, \Delta d = 0 \quad (5.26)$$

or, more generally (with $g(d) = (1-d)^2 + k$, $g'(d) = -2(1-d)$), the evolution equation is

$$\boxed{-2(1-d)\, (\psi_0^+(\boldsymbol{\varepsilon}^e) + \psi_{\mathrm{p}}(\bar{\varepsilon}^p)) + \frac{G_c}{l} d - G_c l\, \Delta d = 0} \quad (5.27)$$

This phase-field equation governs the evolution of the crack phase-field variable d in response to the local energy driving force, plasticity, and regularization, and is fully consistent with the variational structure of the model.

Irreversibility Constraint: The evolution of the phase-field variable is subject to the irreversibility condition

$$d(x,t) \geq d(x,t-\Delta t) \tag{5.28}$$

which enforces that damage can only accumulate (i.e., cracks cannot heal).

Remark on Material Anisotropy: If crystal anisotropy is to be included, the elasticity tensor $\mathbb{C}$ and the spectral decomposition for the tension-compression split should be defined in the crystal (material) frame. All expressions above remain valid, with $\mathbb{C}$ specialized for the chosen crystal symmetry.

This formulation, with well-posed boundary conditions and the irreversibility constraint, ensures both the physical consistency and the numerical robustness of the variational phase-field fracture model at finite strains.

The preceding sections have established a variationally consistent phase-field model for fracture. In the following section, the model's capabilities are demonstrated and validated through several numerical examples. Both brittle and ductile fracture scenarios are investigated under tensile and shear loading, with results compared and analyzed to highlight the model's ability to capture crack initiation, propagation, and failure behavior under different loading and material regimes.

5.3 Numerical Results

To evaluate the predictive capability of the proposed phase-field fracture model, a series of numerical simulations are conducted under both tensile and shear loading. The simulations aim to explore the influence of the internal length scale parameter l, the effectiveness of tension-compression energy splitting, and the role of the fracture threshold energy in ductile versus brittle regimes. All simulations are performed in 2D plane strain using finite elements, with the model implemented in `UMAT` and `UMATHT` user subroutines in ABAQUS.

5.3.1 Single Edge Notched Geometry

The test configuration used throughout the simulations is a single edge notched (SEN) rectangular specimen, as shown in Figure 5.2. The bottom edge is fully constrained, and a uniform vertical displacement u is applied on the top edge to induce mode-I tensile fracture. The crack is initialized from the left edge at mid-height. To accurately capture crack evolution, the mesh is refined on the right half of the domain, as illustrated in Figure 5.3.

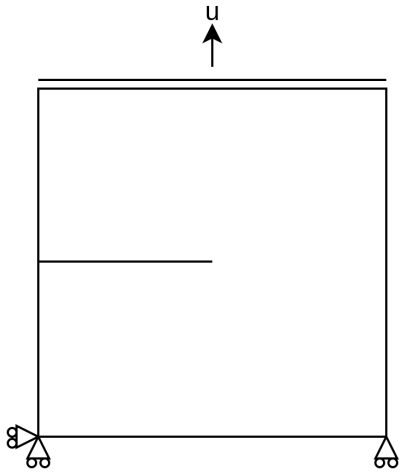


Figure 5.2: Geometry and boundary conditions for the single edge notched specimen under tensile loading.

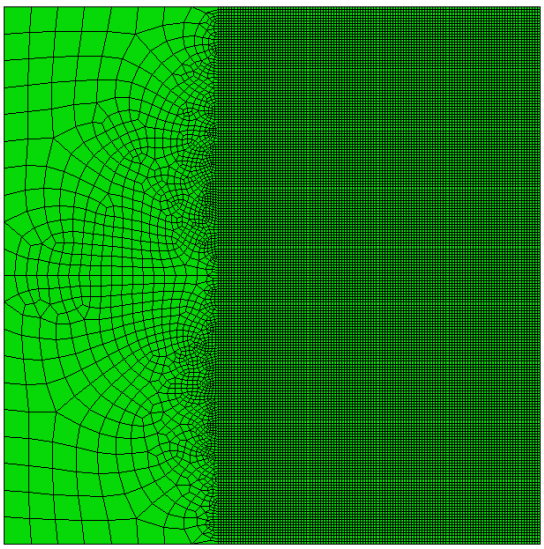


Figure 5.3: Mesh refinement used to enhance resolution of crack propagation zone.

5.3.2 Effect of Length Scale Parameter l in Brittle Fracture

To study the influence of the regularization length l, brittle fracture simulations are performed using $l = 0.01$, 0.02, and 0.03. As shown in Figure 5.4, increasing l leads to a more diffuse crack profile. While all cases produce straight crack propagation under tension, the crack width increases with l, as expected from the regularized phase-field formulation.

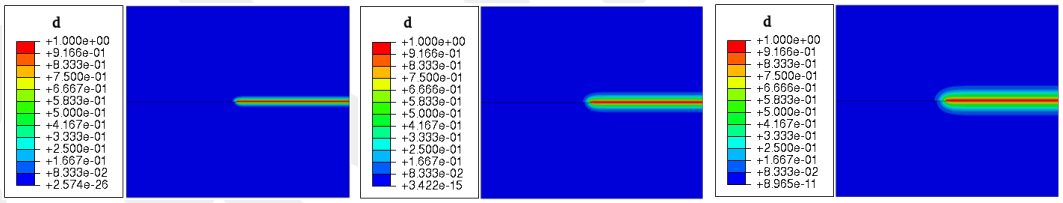


Figure 5.4: Crack profiles in brittle fracture under tension for (left) $l = 0.01$, (middle) $l = 0.02$, and (right) $l = 0.03$.

5.3.3 Tension-Compression Split Validation via Shear Loading

To verify the correct implementation of the spectral decomposition and tension-compression energy split, a shear loading simulation is conducted with $l = 0.02$. Figure 5.5 shows the inclined crack path, consistent with failure under tensile-dominant shear stress components. The result confirms that the phase-field evolution correctly suppresses damage under compression and activates only under tensile energy.

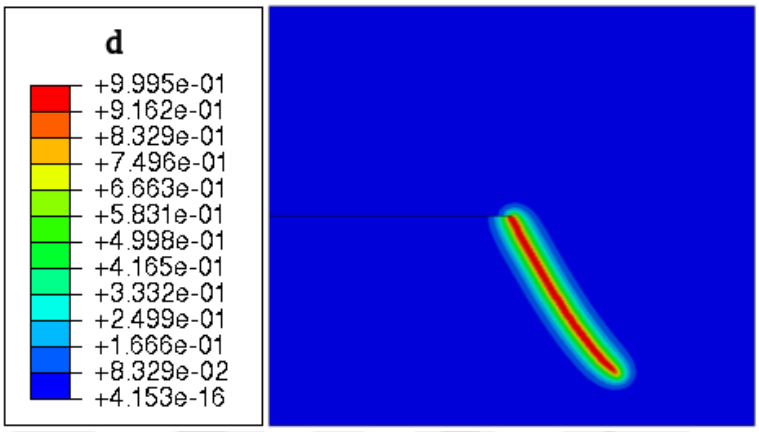


Figure 5.5: Crack propagation under shear loading with $l = 0.02$. Inclined crack confirms that tension-compression split is active.

5.3.4 Stress–Strain Behavior and Fracture Threshold Sensitivity

The critical energy threshold parameter governs the onset of fracture. Two simulations are compared using thresholds of 1 MPa and 30 MPa. Figure 5.6 and Figure 5.7 shows the resulting stress–strain curves. With the lower threshold, brittle fracture initiates immediately after peak stress, leading to sharp stress drop. In contrast, the higher threshold case permits substantial plastic deformation before fracture, resulting in a gradual post-peak softening characteristic of ductile failure.

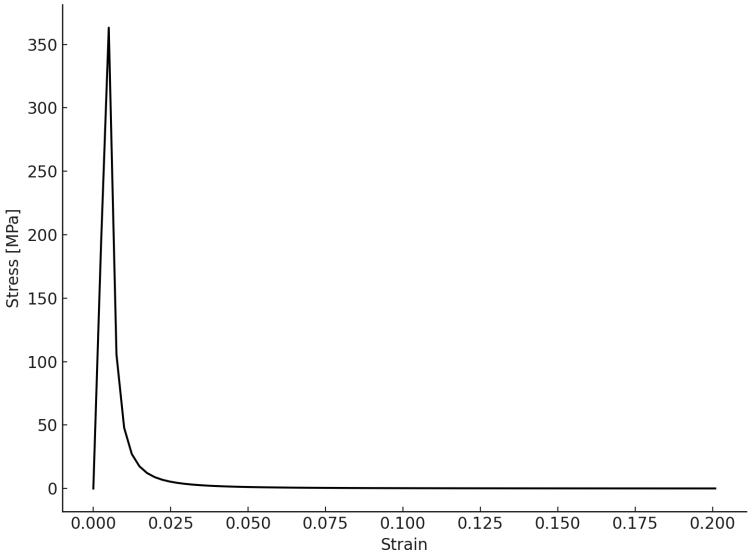


Figure 5.6: Stress–strain response for threshold value 1 MPa. Lower threshold triggers brittle failure.

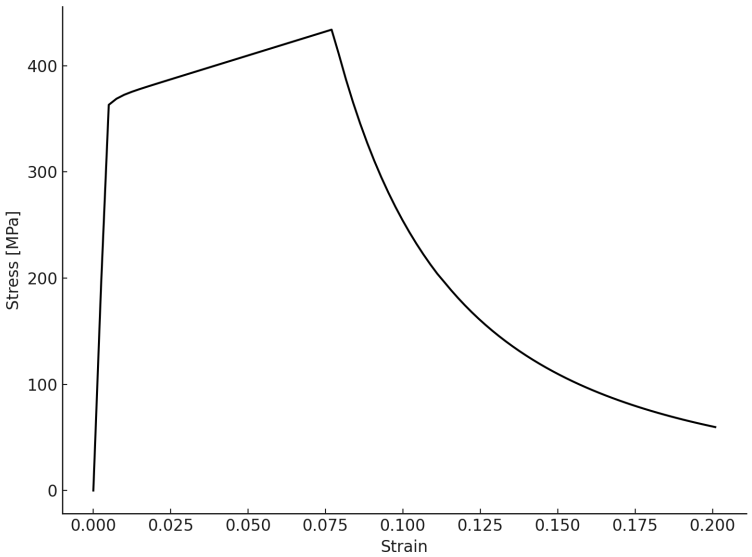


Figure 5.7: Stress–strain response for threshold value 30 MPa. Higher threshold delays damage onset.

5.3.5 Coupled Damage and Plasticity Evolution

The internal variables for damage d and equivalent plastic strain $\bar{\varepsilon}^p$ are tracked over loading. Figures 5.8 and 5.9 show their evolution for 1 MPa and 30 MPa thresholds, respectively. In the brittle case, damage initiates early and dominates the response,

with negligible plastic strain. In contrast, the ductile case exhibits significant plastic accumulation prior to damage onset, indicating the proper interaction between fracture and plasticity mechanisms.

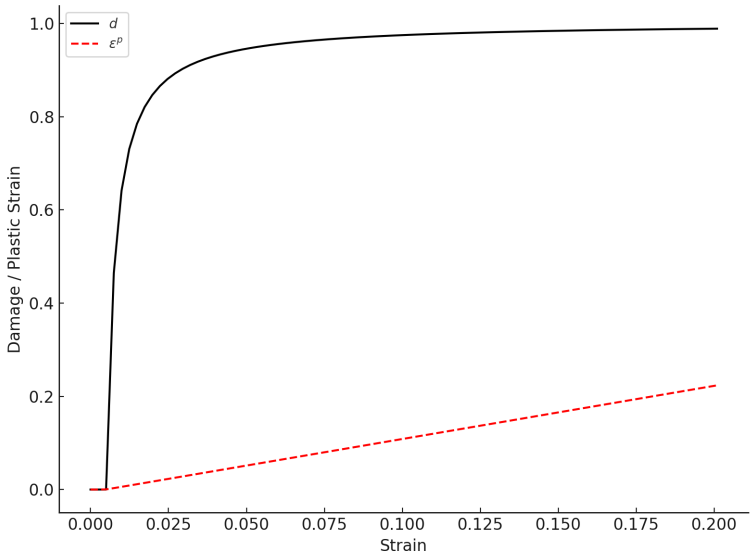


Figure 5.8: Evolution of damage and plastic strain for threshold = 1 MPa. Damage dominates early, consistent with brittle behavior.

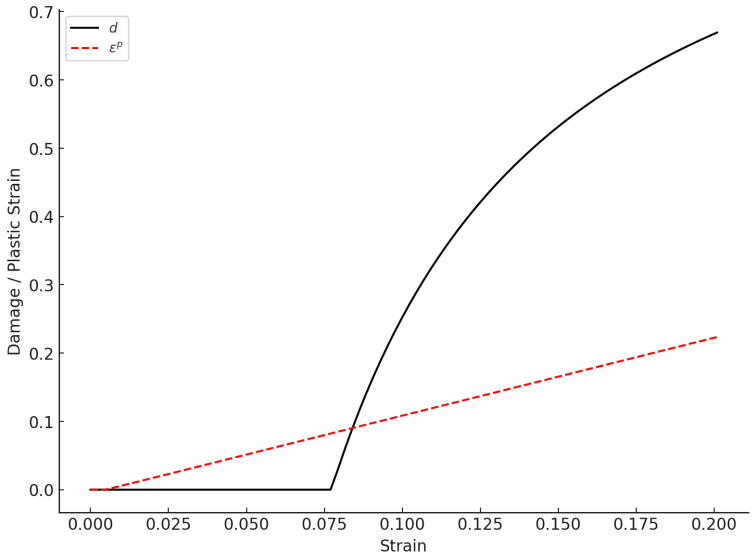


Figure 5.9: Evolution of damage and plastic strain for threshold = 30 MPa. Plastic strain accumulates prior to crack initiation.

5.3.6 Summary

These simulations confirm that the proposed phase-field model:

- Reproduces classical brittle fracture behavior, including straight crack propagation and diffused crack zone scaling with l,
- Correctly implements tension-compression split, suppressing damage under compressive shear,
- Captures the transition from brittle to ductile response via a tunable energy threshold,
- Demonstrates consistent coupling between plastic flow and damage evolution.

The results validate the robustness of the variational formulation and its numerical implementation in ABAQUS for both brittle and ductile fracture scenarios. They also provide a solid foundation for future extensions to include fatigue, crystallographic anisotropy, and hydrogen-assisted fracture. Although not explored numerically in this chapter, the framework is readily extensible to hydrogen-assisted fracture by allowing the fracture toughness to degrade with local hydrogen concentration, and similarly adaptable to fatigue and anisotropic effects through appropriate modifications to the energy functional and constitutive laws.

REFERENCES

[1] Matthew J. Donachie and Stephen J. Donachie, "Superalloys: A Technical Guide," in *Superalloys: A Technical Guide*, 2nd ed., Materials Park, OH: ASM International, 2002.

[2] Tresa M. Pollock and Sammy Tin, "Nickel-Based Superalloys for Advanced Turbine Engines: Chemistry, Microstructure and Properties," *Journal of Propulsion and Power*, vol. 22, pp. 361–374, 2006.

[3] Roger C. Reed, "The Superalloys: Fundamentals and Applications," in *The Superalloys: Fundamentals and Applications*, Cambridge: Cambridge University Press, 2006.

[4] K. Matuszewski and R. Rettig and H. Matysiak and Z. Peng and I. Povstugar and P. Choi and J. Müller and D. Raabe and E. Spiecker and K.J. Kurzydłowski and R.F. Singer, "Effect of ruthenium on the precipitation of topologically close packed phases in Ni-based superalloys of 3rd and 4th generation," *Acta Materialia*, vol. 95, pp. 274-283, 2015.

[5] C M F Rae and Roger C. Reed, "The precipitation of topologically close-packed phases in rhenium-containing superalloys," *Acta Materialia*, vol. 49, pp. 4113-4125, 2001.

[6] David R. Clarke and Michael Oechsner and Nitin P. Padture, "Thermal-barrier coatings for more efficient gas-turbine engines," *MRS Bulletin*, vol. 37, pp. 891–898, 2012.

[7] Dhriti Bhattacharyya and Robert W. Wheeler and Robert P. Harrison and Lyndon Edwards, "The Observation of Slip Phenomena in Single Crystal Fe Samples During In Situ Micro-Mechanical Testing Through Orientation Imaging," *Microscopy and Microanalysis*, vol. 20, pp. 1060–1069, 2014.

[8] F. Hanriot and G. Cailletaud and L. Remy, ”Mechanical behaviour of a nickel-based superalloy single crystal,” in *High Temperature Constitutive Modeling - Theory and Application*, ASME, pp. 139–150, 1991.

[9] G. I. Taylor, ”Plastic Strain in Metals,” *Journal of the Institute of Metals*, vol. 62, pp. 307–324, 1938.

[10] Erik Van der Giessen, ”Crystal Plasticity with Multiple Slip,” in *Encyclopedia of Tribology*, Springer, pp. 647–655, 2013.

[11] Erich Schmid and Walter Boas, ”Kristallplastizität: Mit Besonderer Berücksichtigung der Metalle,” in *Kristallplastizität: Mit Besonderer Berücksichtigung der Metalle*, Berlin: Springer, 1935.

[12] J. W. Christian, ”The Theory of Transformations in Metals and Alloys,” in *The Theory of Transformations in Metals and Alloys*, 2nd ed., Oxford: Pergamon Press, 1983.

[13] M. S. Duesbery and V. Vitek, ”Plastic anisotropy in bcc transition metals,” *Acta Materialia*, vol. 46, pp. 1481–1492, 1998.

[14] R. Gröger and V. Vitek, ”Breakdown of the Schmid law in bcc molybdenum related to the effect of shear stress perpendicular to the slip direction,” *Modelling and Simulation in Materials Science and Engineering*, vol. 16, pp. 035019, 2008.

[15] Marijo Mlikota and Siegfried Schmauder, ”On the Critical Resolved Shear Stress and Its Importance in the Fatigue Performance of Steels and Other Metals with Different Crystallographic Structures,” *Metals*, vol. 8, pp. 883, 2018.

[16] G. I. Taylor and C. F. Elam, ”The distortion of an aluminium crystal during a tensile test,” *Proceedings of the Royal Society of London. Series A, Containing Papers of a Mathematical and Physical Character*, vol. 102, pp. 643–667, 1923.

[17] Franz Roters and Philip Eisenlohr and Thomas R. Bieler and Dierk Raabe, ”Crystal plasticity finite element methods: Theory and application,” *Acta Materialia*, vol. 58, pp. 1152–1211, 2010.

[18] J. Segurado and R. A. Lebensohn and J. Llorca, "Computational homogenization of polycrystals," *Advances in Applied Mechanics*, vol. 51, pp. 1–114, 2018.

[19] Satyapriya Gupta and Curt A. Bronkhorst, "Crystal plasticity model for single crystal Ni-based superalloys: Capturing orientation and temperature dependence of flow stress," *Computational Materials Science*, vol. 174, pp. 109478, 2020.

[20] Ronghai Wu and Michael Zaiser and Stefan Sandfeld, "A continuum approach to combined γ/γ' evolution and dislocation plasticity in Nickel-based superalloys," *Acta Materialia*, vol. 123, pp. 327–340, 2017.

[21] John P. Hirth and Jens Lothe, "Theory of Dislocations," in *Theory of Dislocations*, 2nd ed., New York: John Wiley & Sons, 1982.

[22] Patrick Caron and Thierry Khan, "Evolution of Ni-based superalloys for single crystal gas turbine blade applications," *Aerospace Science and Technology*, vol. 1, pp. 139–151, 1997.

[23] Gregory Martin and R. G. Hoagland and A. Misra, "The influence of stacking fault energy on the deformation behavior of nanoscale metallic multilayers," *Acta Materialia*, vol. 149, pp. 88–99, 2018.

[24] Tresa M. Pollock and Sammy Tin, "Nickel-based superalloys for advanced turbine engines: Chemistry, microstructure, and properties," *Journal of Propulsion and Power*, vol. 22, pp. 361–374, 2006.

[25] Gurtin, Morton E and Fried, Eliot and Anand, Lallit, "The Mechanics and Thermodynamics of Continua," in *The Mechanics and Thermodynamics of Continua*, Cambridge University Press, 2010.

[26] Özgür Aslan, "Simulation numérique de la fissuration par fatigue dans les monocristaux de superalliages à base de nickel," Ph.D. dissertation, École Nationale Supérieure des Mines de Paris, 2010.

[27] Çağatay Kasar and Utku Kaftancıoğlu and Emin Bayraktar and Özgür Aslan, "Lifetime Prediction of Single Crystal Nickel-Based Superalloys," *Applied Sciences*, vol. 15, pp. , 2025.

[28] Johnson, William H., "On Some Remarkable Changes Produced in Iron and Steel by the Action of Hydrogen and Acids," *Nature*, vol. 11, pp. 393, 1875.

[29] Pfeil, L. B., "The Effect of Occluded Hydrogen on the Tensile Strength of Iron," *Proceedings of the Royal Society of London. Series A, Containing Papers of a Mathematical and Physical Character*, vol. 112, pp. 182–195, 1926.

[30] Darken, L. S. and Smith, R. P., "Behavior of Hydrogen in Steel During and After Immersion in Acid," *Corrosion*, vol. 5, pp. 1–16, 1949.

[31] Oriani, R. A., "The diffusion and trapping of hydrogen in steel," *Acta Metallurgica*, vol. 18, pp. 147–157, 1970.

[32] Kumnick, A. J. and Johnson, H. H., "Deep trapping states for hydrogen in deformed iron," *Acta Metallurgica*, vol. 28, pp. 33–39, 1980.

[33] Hirth, J. P., "Effects of hydrogen on the properties of iron and steel," *Metallurgical Transactions A*, vol. 11, pp. 861–890, 1980.

[34] Lynch, S. P., "Hydrogen embrittlement phenomena and mechanisms," *Corrosion Reviews*, vol. 30, pp. 105–123, 2012.

[35] Lynch, S. P., "Hydrogen Embrittlement Phenomena and Mechanisms," in *Hydrogen Embrittlement Phenomena and Mechanisms*, Woodhead Publishing, 2011.

[36] Tunes, M. A. and others, "Limitations of Hydrogen Detection After 150 Years of Research on Hydrogen Embrittlement," *Advanced Engineering Materials*, vol. , pp. , 2024.

[37] Pundt, A. and Kirchheim, R., "Hydrogen in Metals: Microstructural Aspects," *Annual Review of Materials Research*, vol. 36, pp. 555–608, 2006.

[38] Sobotka, J.C. and Dodds, R.H. Jr. and Sofronis, P., "Effects of hydrogen on steady, ductile crack growth: Computational studies," *International Journal of Solids and Structures*, vol. 46, pp. 4095–4106, 2009.

[39] Lyu, Yujie and Wang, Yifeng and Fang, Di and Zhao, Yu and Liu, Jian, "First-principles investigation on hydrogen embrittlement at grain boundaries in bcc iron," *Journal of Materials Science and Technology*, vol. 140, pp. 106–116, 2023.

[40] Gangloff, Richard P., ”Critical issues in hydrogen assisted cracking of structural alloys,” *Metallurgical and Materials Transactions A*, vol. 34, pp. 355–373, 2003.

[41] Ferreira, P. J. and Robertson, I. M. and Birnbaum, H. K., ”Hydrogen effects on the interaction between dislocations,” *Acta Materialia*, vol. 46, pp. 1749–1757, 1998.

[42] Yagodzinskyy, Y. and Saukkonen, T. and Kilpeläinen, S. and Tuomisto, F. and Hänninen, H., ”Effect of hydrogen on plastic strain localization in single crystals of austenitic stainless steel,” *Scripta Materialia*, vol. 62, pp. 155–158, 2010.

[43] Akihide Nagao and Mohsen Dadfarnia and Brian P. Somerday and Petros Sofronis and Robert O. Ritchie, ”Hydrogen-enhanced-plasticity mediated decohesion for hydrogen-induced intergranular and “quasi-cleavage” fracture of lath martensitic steels,” *Journal of the Mechanics and Physics of Solids*, vol. 112, pp. 403-430, 2018.

[44] Birnbaum, Howard K. and Sofronis, Petros, ”Hydrogen-enhanced localized plasticity—a mechanism for hydrogen-related fracture,” *Materials Science and Engineering: A*, vol. 176, pp. 191–202, 1994.

[45] Sofronis, P. and Liang, Y. and Aravas, N., ”Hydrogen induced shear localization of the plastic flow in metals and alloys,” *European Journal of Mechanics - A/Solids*, vol. 20, pp. 8

[46] Song, Jun and Curtin, W. A., ”A nanoscale mechanism of hydrogen embrittlement in metals,” *Acta Materialia*, vol. 61, pp. 682–691, 2013.

[47] Zhang, Wei and Sun, Weiguo and Lu, Yaohua and Pan, Fang and Zhao, Xiujian, ”Hydride-induced embrittlement and fracture of zirconium alloys: A review,” *Journal of Nuclear Materials*, vol. 538, pp. 152180, 2020.

[48] Matsuo, Tomoyuki and Takai, Kenichi, ”Hydrogen-induced delayed fracture of a Ti–6Al–4V alloy and its fracture mechanism,” *Corrosion Science*, vol. 52, pp. 3132–3137, 2010.

[49] A. Díaz and I. I. Cuesta and E. Martínez-Pañeda and J. M. Alegre, ”Analysis of hydrogen permeation tests considering two different modelling approaches for grain boundary trapping in iron,” *International Journal of Fracture*, vol. 223, pp. 17–35, 2020.

[50] McMahon, C. J. and Troiano, A. R., ”The role of hydrogen in the embrittlement of iron and steel,” *Transactions of the Metallurgical Society of AIME*, vol. 239, pp. 524–533, 1973.

[51] Moriconi, C. and Besson, J., ”An energy-based coupled hydrogen diffusion and fracture model for hydrogen embrittlement,” *Engineering Fracture Mechanics*, vol. 178, pp. 605–624, 2017.

[52] Sofronis, P. and McMeeking, R. M., ”Numerical analysis of hydrogen transport near a blunting crack tip,” *Journal of the Mechanics and Physics of Solids*, vol. 37, pp. 317–350, 1989.

[53] Gerberich, W. W. and Olsen, B. and Raman, R. K. S. and Alvarez, C. H., ”Hydrogen embrittlement and decohesion at the atomic scale,” *Journal of the Mechanics and Physics of Solids*, vol. 38, pp. 269–300, 1990.

[54] Martínez-Pañeda, Emilio and del Busto, Susana and Niordson, Christian F. and Betegón, Carlos, ”Strain Gradient Plasticity Modeling of Hydrogen Diffusion to the Crack Tip,” *International Journal of Hydrogen Energy*, vol. 41, pp. 10265–10274, 2016.

[55] Besson, J., ”Continuum models of ductile fracture: a review,” *International Journal of Damage Mechanics*, vol. 19, pp. 3–52, 2010.

[56] Song, J. and Curtin, W. A., ”A nanoscale mechanism of hydrogen embrittlement in metals,” *Acta Materialia*, vol. 61, pp. 682–691, 2013.

[57] Lee, J. and Van der Ven, A., ”Thermodynamics and kinetics of hydrogen in BCC iron from first principles,” *Physical Review Materials*, vol. 5, pp. 033606, 2021.

[58] Barlat, F. and Yoon, J. W., ”Modeling of hydrogen embrittlement in structural metals: A review,” *International Journal of Fracture*, vol. 208, pp. 245–268, 2017.

[59] Martínez-Pañeda, Emilio and Golahmar, Alireza and Niordson, Christian F., "A phase field formulation for hydrogen assisted cracking," *Computer Methods in Applied Mechanics and Engineering*, vol. 342, pp. 742–761, 2018.

[60] Krom, A. H. M. and Bakker, A., "Hydrogen transport near a blunting crack tip," *Journal of the Mechanics and Physics of Solids*, vol. 47, pp. 971–992, 1999.

[61] Anand, L., "A thermo-mechanically-coupled theory accounting for hydrogen diffusion and large elastic–viscoplastic deformations of metals," *International Journal of Solids and Structures*, vol. 48, pp. 962–971, 2011.

[62] Di Leo, Claudio V. and Anand, Lallit, "Hydrogen in metals: A coupled theory for species diffusion and large elastic–plastic deformations," *International Journal of Plasticity*, vol. 43, pp. 42–69, 2013.

[63] Barrera, O. and Tarleton, E. and Tang, H.W. and Cocks, A.C.F., "Modelling the coupling between hydrogen diffusion and the mechanical behaviour of metals," *Computational Materials Science*, vol. 122, pp. 219–228, 2016.

[64] Ozgur Aslan, "Numerical modeling of hydrogen diffusion in metals accounting for large deformations," *International Journal of Hydrogen Energy*, vol. 40, pp. 15227-15235, 2015.

[65] Li, Kaidi and Tang, Bin and Zhang, Mengqi and Zhao, Liguo and Zhang, Jiansheng, "A hydrogen diffusion model considering grain boundary characters based on crystal plasticity framework," *International Journal of Plasticity*, vol. 169, pp. 103740, 2023.

[66] Lu, Guangxian and Zhao, Yunsong and Zhao, Junbo and Chen, Yanhui and Long, Haibo and Gu, Yifan, "Hydrogen embrittlement prompt fracture in Ni-based single crystal superalloy," *Journal of Materials Research and Technology*, vol. 25, pp. 2140–2151, 2023.

[67] Adlakha, I. and Solanki, K. N., "Role of hydrogen on the incipient crack tip deformation behavior in α-Fe: An atomistic perspective," *Journal of Applied Physics*, vol. 123, pp. 014304, 01 2018.

[68] De Assis, Kioshy S and Lage, Marcella Araujo and Guttemberg, Geraldo and dos Santos, Fabrício Pinheiro and Mattos, Oscar R, ”Influence of hydrogen on plasticity around the crack tip in high strength steels,” *Engineering Fracture Mechanics*, vol. 176, pp. 116–125, 2017.

[69] Zhang, Jiding and Sheng, Yue and Yang, Hongda and Wu, Jinbo and Jiang, Xiaoyu, ”Influence of Dislocation Pile-Up on Main Crack Propagation in Nanocrystals in the Hydrogen Environment,” *Acta Mechanica Solida Sinica*, vol. 36, pp. 851–859, 2023.

[70] Shi, Qianyu and Wang, Zhijian and Tang, Hui and Mu, Libo and Zhao, He, ”A Ductile Fracture Phase Field Model Based on Strain Rate-Dependent Fracture Toughness,” *Modelling and Simulation in Engineering*, vol. , pp. , 2024.

[71] Griffith, A. A., ”The phenomena of rupture and flow in solids,” *Philosophical Transactions of the Royal Society A*, vol. 221, pp. 163–198, 1921.

[72] Francfort, G. A. and Marigo, J.-J., ”Revisiting brittle fracture as an energy minimization problem,” *Journal of the Mechanics and Physics of Solids*, vol. 46, pp. 1319–1342, 1998.

[73] Bourdin, B. and Francfort, G. A. and Marigo, J.-J., ”The Variational Approach to Fracture,” *Journal of Elasticity*, vol. 91, pp. 5–148, 2008.

[74] Miehe, C. and Welschinger, F. and Hofacker, M., ”Thermodynamically consistent phase-field models of fracture: Variational principles and multi-field FE implementations,” *International Journal for Numerical Methods in Engineering*, vol. 83, pp. 1273–1311, 2010.

[75] Ambati, M. and Gerasimov, T. and De Lorenzis, L., ”Phase-field modeling of ductile fracture,” *Computational Mechanics*, vol. 55, pp. 1017–1040, 2015.

[76] Miehe, C. and Hofacker, M. and Schänzel, L.-M. and Aldakheel, F., ”Phase field modeling of fracture in multi-physics problems. Part II. Coupled brittle-to-ductile failure criteria and crack propagation in thermo-elastic–plastic solids,” *Computer Methods in Applied Mechanics and Engineering*, vol. 294, pp. 486–522, 2015.

[77] Huang, C. and Gao, X., "Development of a phase field method for modeling brittle and ductile fracture," *Computational Materials Science*, vol. 169, pp. 109089, 2019.

[78] Miehe, C. and Aldakheel, F. and Raina, A., "Phase field modeling of ductile fracture at finite strains: A variational gradient-extended plasticity-damage theory," *International Journal of Plasticity*, vol. 84, pp. 1–32, 2016.

[79] Kalina, M. and Schneider, T. and Waisman, H. and Kästner, M., "Phase-field models for ductile fatigue fracture," *Theoretical and Applied Fracture Mechanics*, vol. 136, pp. 104842, 2025.

[80] Golahmar, A. and Niordson, C. F. and Martínez-Pañeda, E., "A phase field model for high-cycle fatigue: Total-life analysis," *International Journal of Fatigue*, vol. 170, pp. 107558, 2023.

[81] De Lorenzis, L. and McBride, A. and Reddy, B. D., "Phase-field modelling of fracture in single crystal plasticity," *GAMM-Mitteilungen*, vol. 39, pp. 7–34, 2016.

[82] Hernandez Padilla, C. A. and Markert, B., "A coupled ductile fracture phase-field model for crystal plasticity," *Continuum Mechanics and Thermodynamics*, vol. 29, pp. 1017–1026, 2017.

[83] Hutchinson, J. W. and Suo, Z., "Mixed mode cracking in layered materials," *Advances in Applied Mechanics*, vol. 29, pp. 63–191, 1991.

[84] Remmers, J. J. C. and de Borst, R. and Needleman, A. and Sluys, L. J., "A cohesive segments method for the simulation of crack growth," *Computational Methods in Applied Mechanics and Engineering*, vol. 177, pp. 93–116, 2003.

[85] Ekh, M. and Bargmann, S. and Runesson, K., "A finite element framework for microstructure-sensitive damage mechanics with application to dual-phase steel," *International Journal for Numerical Methods in Engineering*, vol. 61, pp. 783–804, 2004.

[86] Dunne, F. P. E. and Man, J. and Pinho, S. T., "Low cycle fatigue crack nucleation and growth in polycrystals," *International Journal of Fatigue*, vol. 29, pp. 2180–2191, 2007.

[87] Aslan, O. and Yalcinkaya, T. and Tekkaya, A. E. and Soyarslan, C., "Micromorphic approach to gradient plasticity and damage in single crystals," *International Journal of Solids and Structures*, vol. 48, pp. 2001–2019, 2011.

[88] Martínez-Pañeda, Emilio and Betegón, Carlos and Niordson, Christian F., "Computational predictions of hydrogen-assisted fatigue crack growth," *International Journal of Fatigue*, vol. 123, pp. 353–362, 2019.

[89] H. Amor and J.-J. Marigo and C. Maurini, "Regularized formulation of the variational brittle fracture with unilateral contact: numerical experiments," *Journal of the Mechanics and Physics of Solids*, vol. 57, pp. 1209–1229, 2009.

APPENDIX A

FINITE ELEMENT IMPLEMENTATION

The numerical implementation of the proposed model is performed via user-defined material subroutines (UMAT and UMATHT) in ABAQUS. The mechanical response is governed through the UMAT, while the hydrogen transport is incorporated via UMATHT. ABAQUS is used both as the solver and the visualization platform. Standard two-dimensional, four-node bilinear plane strain elements (CPE4T) are utilized in the simulations. Each node carries four degrees of freedom: displacement components (u_1, u_2), chemical potential μ_L and the phase-field variable d. These fields are interpolated across the element using standard shape functions, and their spatial gradients are computed via the corresponding derivatives of the shape functions.

Considering a 4-node isoparametric element under plane strain conditions, the interpolation of degrees of freedom and their gradients within the element domain are given by:

$$\mathbf{u} = \sum_{i=1}^{n} N_i \mathbf{u}_i, \quad \nabla\mathbf{u} = \sum_{i=1}^{n} \mathbf{B}_i \mathbf{u}_i \tag{A.1}$$

$$\mu_L = \sum_{i=1}^{n} N_i \mu_{Li}, \quad \nabla\mu_L = \sum_{i=1}^{n} \mathbf{B}_i \mu_{Li} \tag{A.2}$$

$$\mathrm{d} = \sum_{i=1}^{n} N_i \mathrm{d}_i, \quad \nabla\mathrm{d} = \sum_{i=1}^{n} \mathbf{B}_i \mathrm{d}_i \tag{A.3}$$

where N_i are the shape functions. For a bilinear quadrilateral element, the shape functions are defined as:

$$\begin{cases} N_1 = \dfrac{1}{4}(1-\xi)(1-\eta) \\ N_2 = \dfrac{1}{4}(1+\xi)(1-\eta) \\ N_3 = \dfrac{1}{4}(1+\xi)(1+\eta) \\ N_4 = \dfrac{1}{4}(1-\xi)(1+\eta) \end{cases} \tag{A.4}$$

The time rates of the interpolated fields, such as velocity and other rate-type variables, are computed using finite difference approximations between consecutive time steps:

$$\mathbf{V}_{t+1} = \frac{\mathbf{u}_{t+1} - \mathbf{u}_t}{dt} \tag{A.5}$$

$$\dot{\mu}_{L_{t+1}} = \frac{\mu_{L_{t+1}} - \mu_{L_t}}{dt} \tag{A.6}$$

$$\dot{\mathrm{d}}_{t+1} = \frac{\mathrm{d}_{t+1} - \mathrm{d}_t}{dt} \tag{A.7}$$

To compute the physical derivatives of the shape functions, the Jacobian transformation is employed, yielding:

$$\begin{bmatrix} \dfrac{dN}{dx} \\ \dfrac{dN}{dy} \end{bmatrix} = J^{-1} \begin{bmatrix} \dfrac{dN}{d\xi} \\ \dfrac{dN}{d\eta} \end{bmatrix} \tag{A.8}$$

In plane strain formulation, the strain-displacement matrix **B** for the element is constructed as follows:

$$\mathbf{B} = \begin{bmatrix} N_{1,1} & 0 & N_{2,1} & 0 & \cdots & N_{nNode,1} & 0 \\ 0 & N_{1,2} & 0 & N_{2,2} & \cdots & 0 & N_{nNode,2} \\ N_{1,2} & N_{1,1} & N_{2,2} & N_{2,1} & \cdots & N_{nNode,2} & N_{nNode,1} \end{bmatrix} \tag{A.9}$$

Here, $N_{i,1}$ and $N_{i,2}$ denote the partial derivatives of the shape functions with respect to x and y, respectively. Additionally, a matrix **G** is defined to represent the gradient operator acting on scalar fields:

$$\mathbf{G} = \begin{bmatrix} N_{1,1} & 0 & N_{2,1} & 0 & \cdots & N_{nNode,1} & 0 \\ 0 & N_{1,2} & 0 & N_{2,2} & \cdots & 0 & N_{nNode,2} \\ N_{1,2} & 0 & N_{2,2} & 0 & \cdots & N_{nNode,2} & 0 \\ 0 & N_{1,2} & 0 & N_{2,2} & \cdots & 0 & N_{nNode,2} \end{bmatrix} \tag{A.10}$$

Finally, the deformation gradient tensors at the beginning and end of the time step are evaluated using the displacement gradient:

$$\mathbf{F}_t = \mathbf{1} + \nabla \mathbf{u}_t, \quad \mathbf{F}_{t+1} = \mathbf{1} + \nabla \mathbf{u}_{t+1} \tag{A.11}$$

where **1** is the identity tensor, and $\nabla \mathbf{u}$ represents the spatial gradient of displacement.

A.1 Time Integration for Hydrogen Diffusion Model

Time Integration for Rate Dependent Finite Strain Isotropic Hardening

Trial Values

- Step 1: Polar Decomposition of Elastic Distortion and Hencky Strain

$$F_{n+1}^{e\,trial} = F_{n+1}\, F_n^{p-1}$$
$$F_{n+1}^{e\,trial} = R_{n+1}^{e\,trial}\, U_{n+1}^{e\,trial}$$
$$E_{n+1}^{e\,trial} = lnU_{n+1}^{e\,trial}$$

- Step 2: Trial Second Piola and Mandel Stresses

$$T_{n+1}^{e\,trial} = 2\mu E_{0\,n+1}^{e\,trial} + \kappa\, trE_{n+1}^{e\,trial} I$$
$$or$$
$$T_{n+1}^{e\,trial} = 2\mu E_{n+1}^{e\,trial} + \lambda\, trE_{n+1}^{e\,trial} I$$
$$M_{n+1}^{e\,trial} = F_{n+1}^{e\,trial^T}\, F_{n+1}^{e\,trial}\, T_{n+1}^{e\,trial}$$
$$M_{0\,n+1}^{e\,trial} = M_{n+1}^{e\,trial} - \frac{1}{3} trM_{n+1}^{e\,trial} I$$

Note: For coupled; $T_{n+1}^{e\,trial} = 2\mu E_{n+1}^{e\,trial} + \lambda\, trE_{n+1}^{e\,trial}\boldsymbol{I} - 3\kappa\beta(C_{Ln+1} - C_0)\boldsymbol{I}$

- Step 3: Equivalent Tensile Stress and Plastic Flow Direction

$$\overline{\sigma}_{n+1}^{trial} = \sqrt{\frac{3}{2}} |M_{0\,n+1}^{e\,trial}|$$
$$N_{n+1}^{p\,trial} = \sqrt{\frac{3}{2}} \frac{M_{0\,n+1}^{e\,trial}}{\overline{\sigma}_{n+1}^{trial}} = N_{n+1}^{p}$$

- Step 4: Check plasticity criterion

$$if(\overline{\sigma}_{n+1}^{trial} > Y(S))$$
$$Y(S) = yield + \Delta t\, H\, \dot{\epsilon}_n^p + y_\infty \left(\frac{\dot{\epsilon}_n^p}{\dot{\epsilon}_0^p}\right)^m$$
$$f = (\sigma_{n+1}^{trial} - Y(S)) - 3\mu\Delta t \dot{\epsilon}_{n+1}^p - \Delta t\, H\, \dot{\epsilon}_{n+1}^p = 0$$

- Step 5: Updates

$$Y(S) = yield + \Delta t\, H\, \dot{\epsilon}^p_{n+1}$$
$$D^p_{n+1} = \sqrt{\frac{3}{2}} \dot{\epsilon}^p_{n+1} N^p_{n+1}$$
$$\epsilon^p_{n+1} = \epsilon^p_n + \Delta t \dot{\epsilon}^p_{n+1}$$

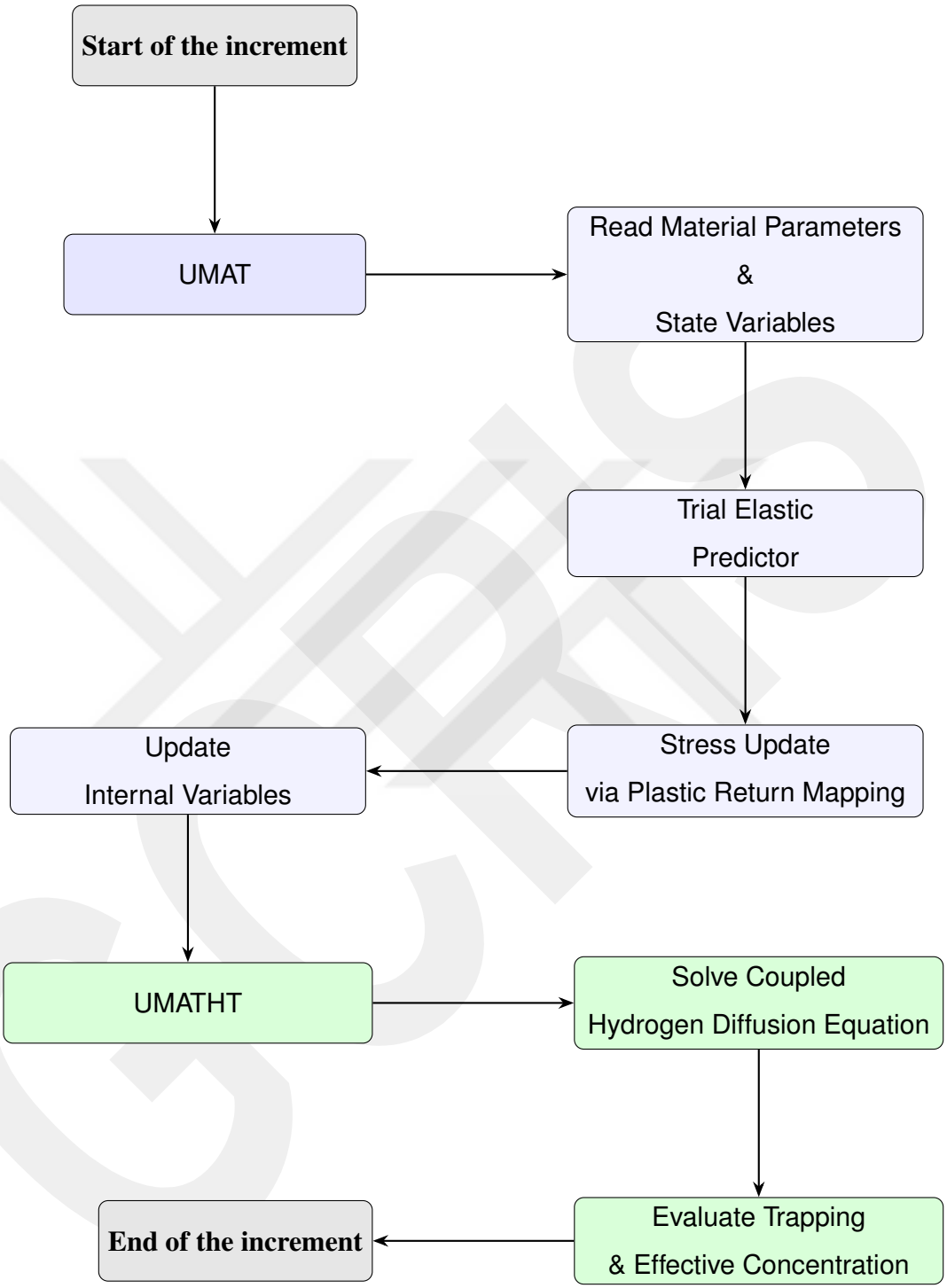
- Step 6: Update Elastic and Plastic Distortion

$$F^p_{n+1} = exp(\Delta t D^p_{n+1}) F^p_n$$
$$F^e_{n+1} = F_{n+1}\, F^{p\,-1}_{n+1}$$

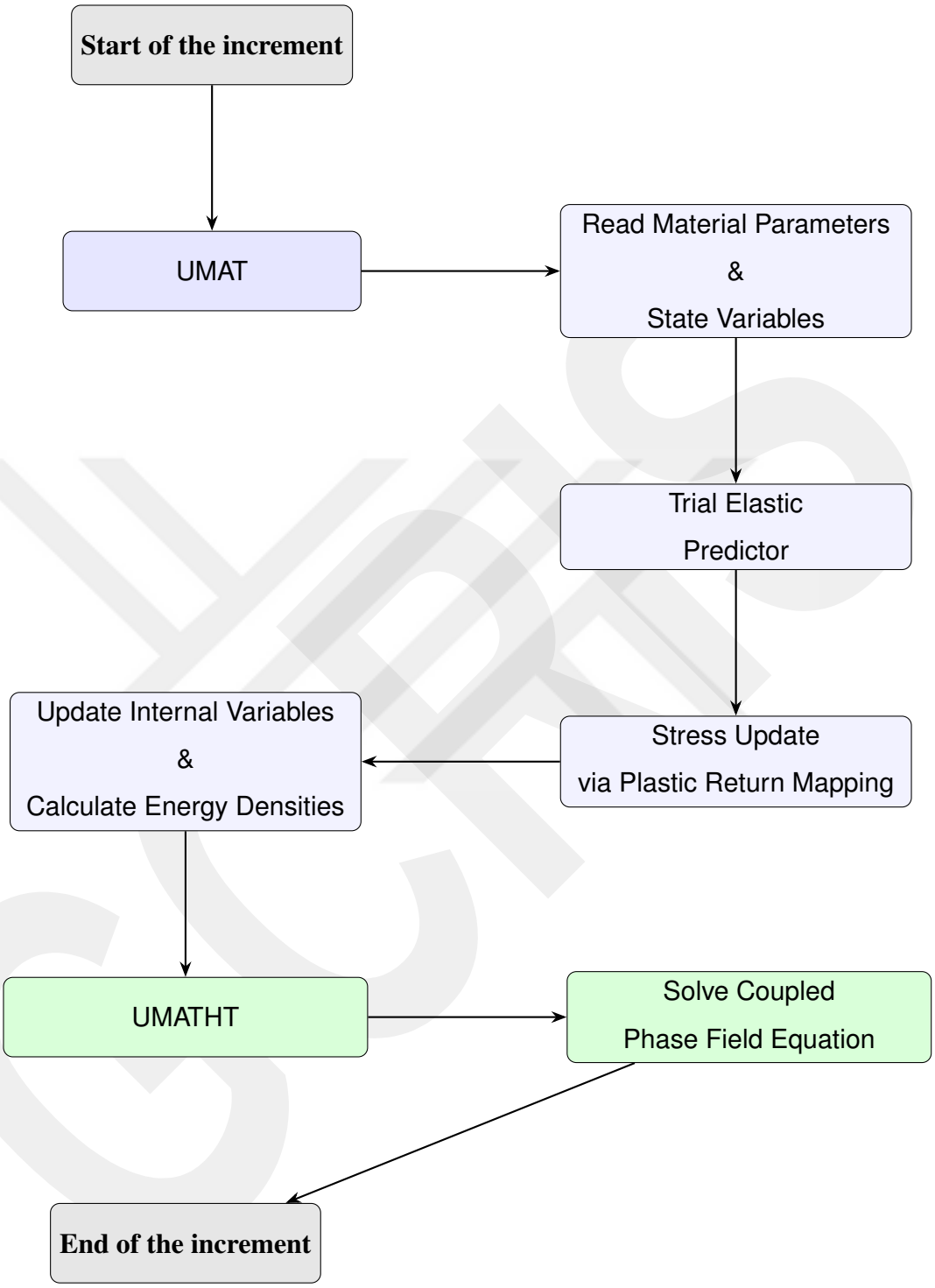
- Step 7: Obtain Cauchy

$$T^e_{n+1} = 2\mu E^e_{n+1} + \lambda\, tr E^e_{n+1} I$$
$$T_{n+1} = J^{-1}\, F^e_{n+1}\, T^e_{n+1}\, F^{e\,T}_{n+1}$$

A.2 Hydrogen Diffusion Flowchart for UMAT & UMATHT Subroutines



A.3 Phase Field Fracture Flowchart for UMAT & UMATHT Subroutines



APPENDIX B

PARTIAL DIFFERENTIAL EQUATIONS

B.1 PDE for Hydrogen

The strong form of the hydrogen mass balance is:

$$\dot{C}_L = -\nabla \cdot \mathbf{j}_L - \sum_k \dot{C}_{T_k}, \qquad \mathbf{j}_L = -\mathbf{m}_L \nabla \mu_L \tag{B.1}$$

The Galerkin weak form is obtained by multiplying with a test function δC_L and integrating over the domain Ω:

$$\int_\Omega \delta C_L \, \dot{C}_L \, \mathrm{d}V - \int_\Omega \nabla \delta C_L \cdot \mathbf{m}_L \nabla \mu_L \, \mathrm{d}V + \int_\Omega \delta C_L \sum_k \dot{C}_{T_k} \, \mathrm{d}V = 0 \tag{B.2}$$

B.1.1 Residual Vector

Let the finite element approximation be:

$$C_L \approx \sum_A N_A \hat{C}_A, \quad \delta C_L \approx N_B \tag{B.3}$$

The residual vector entry for node B is:

$$R_B = \int_\Omega N_B \, \dot{C}_L \, \mathrm{d}V - \int_\Omega \nabla N_B \cdot \mathbf{m}_L \nabla \mu_L \, \mathrm{d}V + \int_\Omega N_B \sum_k \dot{C}_{T_k} \, \mathrm{d}V \tag{B.4}$$

B.1.2 Tangent Matrix

The tangent matrix entry is given by:

$$K_{BA} = \frac{\partial R_B}{\partial \hat{C}_A} \tag{B.5}$$

Using the chain rule:

$$\frac{\partial \mu_L}{\partial \hat{C}_A} = \frac{\partial \mu_L}{\partial C_L} N_A, \quad \frac{\partial \nabla \mu_L}{\partial \hat{C}_A} = \frac{\partial \mu_L}{\partial C_L} \nabla N_A \tag{B.6}$$

Then:

$$K_{BA} = \int_\Omega \nabla N_B \cdot \mathbf{m}_L \left(\frac{\partial \mu_L}{\partial C_L} \nabla N_A \right) \mathrm{d}V + \int_\Omega N_B \left(\frac{\partial}{\partial C_L} \sum_k \dot{C}_{T_k} \right) N_A \, \mathrm{d}V \tag{B.7}$$

B.2 PDE for Phase-Field Fracture

The strong form of the phase-field fracture evolution equation is:

$$\mathcal{G}_c \ell \Delta \phi - \frac{\mathcal{G}_c}{\ell}(1 - \phi) + g'(\phi)\Psi^+ = 0 \tag{B.8}$$

where:

- ϕ is the phase-field variable,
- $\mathcal{G}_c$ is the critical energy release rate,
- ℓ is the length scale parameter,
- Ψ^+ is the tensile part of the elastic energy density,
- $g(\phi)$ is the degradation function (commonly $g(\phi) = (1 - \phi)^2$).

Multiply by a test function $\delta\phi$ and integrate:

$$\int_\Omega \delta\phi \left(-\frac{\mathcal{G}_c}{\ell}(1-\phi) + g'(\phi)\Psi^+ \right) \mathrm{d}V + \int_\Omega \mathcal{G}_c \ell \nabla\delta\phi \cdot \nabla\phi \, \mathrm{d}V = 0 \tag{B.9}$$

B.2.1 Residual Vector

Let:

$$\phi \approx \sum_A N_A \hat{\phi}_A, \quad \delta\phi \approx N_B \tag{B.10}$$

Then the residual vector entry for node B is:

$$R_B = \int_\Omega N_B \left(-\frac{\mathcal{G}_c}{\ell}(1-\phi) + g'(\phi)\Psi^+ \right) \mathrm{d}V + \int_\Omega \mathcal{G}_c \ell \nabla N_B \cdot \nabla\phi \, \mathrm{d}V \tag{B.11}$$

B.2.2 Tangent Matrix

The tangent matrix entry is defined as:

$$K_{BA} = \frac{\partial R_B}{\partial \hat{\phi}_A} \tag{B.12}$$

Using:

$$\frac{\partial \phi}{\partial \hat{\phi}_A} = N_A, \quad \frac{\partial \nabla\phi}{\partial \hat{\phi}_A} = \nabla N_A, \quad \frac{\partial g'(\phi)}{\partial \hat{\phi}_A} = g''(\phi) N_A \tag{B.13}$$

Then:

$$K_{BA} = \int_\Omega N_B \left(\frac{\mathcal{G}_c}{\ell} N_A + g''(\phi)\Psi^+ N_A \right) \mathrm{d}V + \int_\Omega \mathcal{G}_c \ell \nabla N_B \cdot \nabla N_A \, \mathrm{d}V \tag{B.14}$$

Note

If a history field $\mathcal{H}$ is used instead of Ψ^+, then $\Psi^+ \rightarrow \mathcal{H}$, and the expression becomes:

$$R_B = \int_\Omega N_B \left(-\frac{\mathcal{G}_c}{\ell}(1-\phi) + g'(\phi)\mathcal{H} \right) \mathrm{d}V + \int_\Omega \mathcal{G}_c \ell \nabla N_B \cdot \nabla \phi \, \mathrm{d}V \tag{B.15}$$

$$K_{BA} = \int_\Omega N_B \left(\frac{\mathcal{G}_c}{\ell} N_A + g''(\phi)\mathcal{H} N_A \right) \mathrm{d}V + \int_\Omega \mathcal{G}_c \ell \nabla N_B \cdot \nabla N_A \, \mathrm{d}V \tag{B.16}$$

CURRICULUM VITAE

Surname, Name: Çamalan, Caner

EDUCATION

Degree	Institution	Year of Graduation
PhD	Atılım University Mechanical Engineering	2025
BS	Atılım University Mechanical Engineering	2016
High School	Sokullu Mehmet Paşa High School, Ankara	2009

FOREIGN LANGUAGES

Advanced English

PUBLICATION

O. Aslan, G.C. Kabakci, F. Sait, C. Camalan, B. Baranoglu, and E. Bayraktar, "A coupled modeling and simulation approach to electromagnetic sheet metal forming,", Journal AMPT, Manuscript submitted for publication(2025).

RESEARCH INTERESTS

- ➢ Hydrogen Embrittlement
- ➢ Phase Field Modeling of Fracture
- ➢ Numerical Modeling of Coupled Systems
- ➢ Crystal Plasticity